A Non-invasive Central Arterial Pressure Waveform Estimation System using Ultrasonography for Real-time Monitoring

by

Joohyun Seo

B.S., Seoul National University (2012)

S.M., Massachusetts Institute of Technology (2014)

Submitted to the

Department of Electrical Engineering and Computer Science

in partial fulfillment of the requirements for the degree of

Doctor of Philosophy

at the

MASSACHUSETTS INSTITUTE OF TECHNOLOGY

September 2018

Author .....

Department of Electrical Engineering and Computer Science

July 16, 2018

Certified by .....

Hae-Seung Lee

ATSP Professor of Electrical Engineering

Thesis Supervisor

Certified by .....

Charles G. Sodini

Lebel Professor of Electrical Engineering

Thesis Supervisor

Accepted by .....

Leslie A. Kolodziejski

Professor of Electrical Engineering and Computer Science

Chair, Department Committee on Graduate Students

A Non-invasive Central Arterial Pressure Waveform Estimation System using Ultrasonography for Real-time Monitoring

by

Joohyun Seo

Submitted to the Department of Electrical Engineering and Computer Science
on July 16, 2018, in partial fulfillment of the requirements for the degree of
Doctor of Philosophy

Abstract

This thesis details non-invasive evaluation of a central arterial blood pressure (ABP) waveform using a low-cost ultrasound scanning system. ABP bears significant clinical value in cardiovascular pathophysiology. Non-invasive evaluation of the full ABP waveform has been long desired by medical communities due to its anticipated opportunities to greatly enhance cardiovascular patient care. In addition, central ABP has been focused on because of its close association with the adverse outcomes of cardiovascular events.

This work mainly explores monitoring of carotid arterial pulsation and local pulse wave velocity (PWV) by the designed system to estimate the ABP waveform, conducting simultaneous spectral Doppler and M-mode imaging. The system is characterized in electrical and acoustic domains to preserve adequate signal integrity to faithfully extract a spatial mean flow velocity and an arterial distension waveform. The carotid ABP waveform is estimated from the distension waveform and the local PWV with one-time calibration from an arterial-line (A-line) or a volume clamping method.

The proof-of-concept study demonstrated that the carotid ABP waveform estimation is feasible. The pulse pressure estimation compared to a sphygmomanometer and a finger ABP waveform differ by 1.49±11.7 and -4.92±12.9 mmHg, respectively. The designed and characterized motion-tolerant ultrasonography extends tolerable lateral offsets up to ±8 mm while limiting error of the flow and distension waveforms within about 5%. The system is also validated under hemodynamic stress of the Valsalva maneuver and in intensive care settings compared to the A-line. This thesis demonstrates the profound potential for a portable low-cost ultrasound system toward non-invasive evaluation of a central ABP waveform in clinically relevant settings.

Thesis Supervisor: Hae-Seung Lee
Title: ATSP Professor of Electrical Engineering

Thesis Supervisor: Charles G. Sodini
Title: Lebel Professor of Electrical Engineering

Acknowledgments

I have received tremendous helps from so many people. This thesis work cannot be accomplished without these helps. Here, I would like to write a few words to acknowledge them.

My advisors, Prof. Hae-Seung Lee and Prof. Charles Sodini, have been great mentors. When I was struggling, they believed in me. In addition to their insightful guidance on this thesis work, I was always able to get through hardship thanks to their beliefs. I would like to emulate their mentorship in the future. Prof. Aaron Aguirre also greatly devoted his time to maximize my growth and learning opportunities, especially through clinical preceptorship. I would like to express my sincere appreciation to the committee members for their tremendous supports.

I would like to also thank former and current members in Lee and Sodini groups (Sabino, Doyeon, Xi, Taehoon, Maggie, Sidney, Katie, Kailiang, Kyle, and many more). Thanks to their comments and feedbacks, this thesis work could be enriched. I would remember all their helps and casual technical discussion that we had.

I have got many helps from people both inside and outside MIT. Prof. Thomas Heldt was always willing to help and discuss my problems. Kai Thomenius gave me insightful feedbacks especially in ultrasound. I also thank Cathy Ricciardi for the help in MIT Clinical Research Center. Also, industry experts (Tom O'Dwyer, Jeff Ashe, Brian Brandt, Balasundar Raju) greatly increased the depth of this thesis work. I also thank the study team at Boston Medical Center to have gone through all logistics to make the clinical study happen.

I am also grateful to my parents for their unconditional supports on this journey of doctoral study. Even though they were at the other side of the planet, I always felt connected and be supported. Of course, my special thanks go to Chaeyoung who genuinely supported me so that I could summon courage to sprint toward the finish line of this journey. Finally, I would like to thank my friends. I enjoyed working in the Korean Graduate Student Association and playing tennis. Thanks to their friendship, my non-academic life in Cambridge has been full of joy.

This thesis work was supported by Samsung Fellowship, Center for Integrated Circuits and Systems (CICS), and Medical Electronic Device Realization Center (MEDRC) – Philips Healthcare.

Contents

List of Figures

List of Tables

Chapter 1

Introduction

1.1 Background

The cardiovascular system transports oxygen, carbon dioxide, nutrients, and wastes to sustain life. Due to its life-supporting role, cardiovascular diseases (CVDs) are the leading cause of death worldwide according to a World health organization report [1]. Among them, ischemic heart diseases and stroke are ranked first and second, respectively. In addition, they constitute 30% of the causes of death in the United States according to a Centers for Disease Control and Prevention (CDC) report [2].

With various cardiovascular diagnostic tools such as electrocardiogram (ECG) and echocardiogram, arterial blood pressure (ABP) helps determine not only diagnosis but also prognosis of CVDs. Thus, the blood pressure is considered a target to monitor and manage.

While the primary role of ABP is to drive systemic circulation, it also reflects patho-physiological states of the arterial system, such as arterial stiffening. An arterial Windkessel model is often used to interpret the arterial system in the simplest way [3]. This lumped circuit model simulates arterial compliance (i.e., increase of intravascular volume over increase of ABP) and total peripheral resistance. Elastic arteries cushion sudden increase of ABP caused by ventricular contraction of the heart. The arteries also temporarily store blood during systole and gradually release it to peripheries during diastole. In this model, pulse pressure (PP, the difference between systolic

and diastolic blood pressure) is associated with arterial stiffness; The increased PP given the same stroke volume (i.e., ejected blood volume per beat) often implies a stiffened arterial system due to arteriosclerosis.

Although the Windkessel model gives basic insight into the PP increase by the arterial stiffening, the exact shape of an ABP waveform results from complex wave behaviors in the arterial system. In detail, the major artery is modeled as an elastic tube filled with fluid, inertial mass to accelerate with negligible viscous drag. An arterial tree consists of the elastic tubes successively branching out into smaller ones. Distal branches are terminated by resistors mimicking high resistances of the arterioles and capillaries. In this model, the arterial stiffening increases the propagation speed of a pulse wave, thus modifying morphology of the ABP waveform.

Conversely, ABP directly applies mechanical stress on the heart and vasculatures. CVDs are mainly categorized into the heart and vascular diseases, but their disease processes are usually intertwined. Abnormally elevated mean arterial pressure (MAP) or PP exerts stress on the vessel wall. This stress injures endothelium chronically, if repeated. According to the response-to-injury hypothesis, the repeated injury leads to endothelial dysfunction, platelet aggregation, migration of smooth muscle cells into intima of the wall, and synthesis of collagen, thereby modifying viscoelastic property of the vessel wall [4]. This atherosclerotic process forms plaque and narrows the lumen, potentially triggering ischemic events due to blockage caused by the narrowed lumen or blood clots from the ruptured plaque.

Besides vascular diseases, the increased PP due to the systemic arterial stiffening burdens the heart from ejecting blood into the arterial system. The increased PP also contributes to microvascular diseases in the brain and kidney. This is mainly because their vascular resistances are low compared to other vascular beds, such that the micro vessels experience the unattenuated high pulsatile stress generated by the ventricular contraction during systole [5].

Numerous studies have clearly identified that hypertension is a risk factor for CVD events. Initially, systolic (SBP) and diastolic blood pressure (DBP) were correlated to disease severity. A current clinical guideline for hypertension is based on SBP and

DBP, but gradually, PP has been recognized as a more relevant risk factor [6]. In fact, cyclic stretch on endothelial cells was shown to consistently synthesize collagen, one of the components leading to the arterial stiffening with aging, much more rapidly than the static stress [7]. This study implies that the pulsatile stress primarily directs arterial remodeling. Subsequent studies supported that PP is identified as a strong risk factor for coronary heart diseases in the middle-aged and elderly [8] and recurrent myocardial infarction [9].

While the brachial PP has been used for these studies due to measurement convenience, the aortic and carotid PPs have been found more closely associated with adverse cardiovascular outcomes [10], such as coronary artery diseases [11]. These studies implicate that the central ABP more closely reflects the load placed on the left ventricle and the coronary and cerebral vasculatures [10]. Due to its clinical significance, several studies have focused on estimating the central ABP from the peripheral ABP waveform [12–14].

Even though most clinical practices are well-established based on SBP and DBP, further studies are certainly desired to close the gap in our understanding of the interplay between ABP and CVDs. A recent study shows that CVD events, such as heart attacks, heart failures, and stroke, are reduced by one third, and the risk of death are reduced by a quarter through the intensive control of SBP under 120 mmHg instead of the current clinical guideline of 140 mmHg [15]. This study exemplifies both the immense prognostic values that ABP carries and lack of understanding as to how to most effectively use ABP measurements for the patients' benefit.

1.2 Motivation

The clinical information of interest has migrated from static to pulsatile stress and toward specific features in the full ABP waveform calculated from pulse wave analysis. Besides, the arterial site of interest also migrates from peripheries to central sites as the arterial model evolves.

The ABP waveform is believed to offer unparalleled cardiovascular assessments

and useful information in understanding and predicting the course of CVDs. For example, PhysioNet Challenge 2009 asked contestants to predict an acute hypotensive episode–a sudden drop of ABP–at least an hour in advance solely based on the continuously monitored ABP waveform obtained in an intensive care unit for more than ten hours [16]. Many prediction models demonstrated excellent prediction accuracies greater than 93% by utilizing machine-learning techniques. This example clearly suggests rich information contained in the ABP waveform should be discovered.

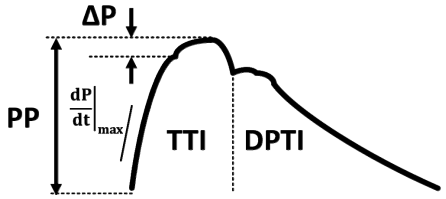

Figure 1-1: Arterial pressure waveform and its studied features.

Several features in the waveform intrigue researchers as compelling candidates for future studies as shown in Figure 1-1. For example, an augmentation index (AIx), defined as the ratio between a fraction of the augmented pressure (ΔP) due to the wave reflection to the measured PP, is associated with the arterial stiffening because of earlier return of the reflected wave caused by increased pulse wave velocity [17]. A subendocardial viability index (SVI), the ratio of the diastolic pressure-time integral (DPTI, area under the ABP waveform during diastole) to systolic tension-time index (TTI), is believed to represent cardiac workload relative to perfusion of myocardium because the heart contracts during systole while it relaxes to be perfused mostly during diastole [18].

Several studies attempted to identify the closer association between these parameters to CVD events. For instance, the AIx is identified as a strong, independent risk factor for premature coronary artery diseases [17] and left ventricular hypertrophy [19]. The SVI is an independent predictor for coronary flow reserve, a parameter to represent coronary microvascular function [20]. In addition to these features, several hemodynamic parameters, such as cardiac output (CO) and total peripheral

resistance (TPR), can be estimated by analyzing the peripheral ABP waveform even in ambulatory settings [21, 22]. Yet, the development of a handy, non-invasive ABP waveform monitoring device has been desired to conduct a series of large population studies. These studies are expected to establish the solid association between the newly identified features and CVD events.

In addition to the detailed morphology of the ABP waveform drawing unprecedented attentions, its variability is also implicated to possible association with the CVDs [23]. Indeed, ABP is the dynamic parameter that reacts to various stimuli both internal and external to the body. It is subject to changing accordingly in order to maintain adequate systemic perfusion under various circumstances, such as varying metabolic needs and the mechanical stress imposed on the circulatory system. A postural change is a great example of such stress.

This variability implies that the ABP obtained at one instance can hardly represent general cardiovascular health without proper contexts. For this reason, a standard blood pressure cuff measurement is usually conducted after a patient is adequately stabilized. In other words, real-time and long duration monitoring of the ABP waveform offers ample opportunities to investigate how the cardiovascular system responds to various stimuli. In fact, blood pressure fluctuations have been observed in a continuous monitoring setting [24, 25]. For example, a 10s Mayer wave is an example of the fluctuations due to baroreflex, which is the body's homeostatic mechanism to control central arterial pressure at a nearly constant level [26]. The body controls the ABP by modulating the heart rate and changing vasomotor tones, both of which are orchestrated by the autonomic nervous system.

Many studies to relate the heart rate or blood pressure variability to cardiovascular health exemplify such efforts. Baroreflex sensitivity, measured as the heart rate change over the pressure change, has been found significantly impaired in bilateral carotid atherosclerosis patients [27]. Considering that baroreceptors are mainly located at the aortic arch and carotid sinus, this study implies the atherosclerosis in these regions can cause dysfunction of a central ABP control loop. In addition, in hypertensive patients, severity of the target-organ damage is highly correlated to the

blood pressure variability as well as the MAP for 24 hours compared to a snapshot of sphygmomanometer readings [28]. To summarize, only continuous or real-time monitoring can allow analyzing the beat-to-beat variation of ABP and greater in-depth understanding about general health of the cardiovascular system.

Unfortunately, the ABP measurements currently practiced in hospitals are unsuitable for real-time monitoring of the ABP waveform in a large population. In clinics, SBP and DBP are measured using a sphygmomanometer. In this measurement, a cuff is wrapped around the upper extremity. Initially, the cuff is inflated to completely occlude the brachial artery. Then, the cuff gradually releases the pressure while SBP and DBP are determined by listening to blood flow using a stethoscope (auscultatory) or an automated algorithm (oscillometric). Although this measurement is handy, it ignores the beat-to-beat variation since it takes multiple cardiac cycles. Additionally, it only measures SBP and DBP, discarding useful information of the dynamic nature of the arterial system.

While a new device gets tested to the cuff measurement, the gold standard method to obtain the complete ABP waveform is an arterial-line (A-line) which requires arterial catheterization and either insertion of a pressure wire into a target arterial site or connection of a pressure tubing to a pressure transducer. Although considered the gold standard, it is highly invasive, and, therefore, seldom practiced in ambulatory settings. Currently, the A-line is only practiced in an intensive care or surgical settings where real-time ABP monitoring is required to trigger a timely alarm for medical emergencies. Consequently, its highly invasive nature not only increases various patients' risks but makes the usage of this waveform very expensive for cardiovascular studies.

Several non-invasive ABP waveform estimation techniques have been introduced, and they mainly fall into two categories: a volume clamping method and arterial tonometry. Penaz introduced the principle that established the volume clamping method [29]. This method requires an inflatable finger cuff exerting pressure on the finger, and the blood volume in the finger is continuously monitored using infrared photoplethysmography. While clamping the blood volume by actively controlling the

cuff pressure, the arterial pressure is calculated [30]. However, in order to achieve high accuracy, it requires careful and repeated calibrations, inevitably interrupting the continuous monitoring. Partly occluding the vessel hinders adequate perfusion of the monitored finger in a longer time scale. Furthermore, its measurement site is restricted to the fingers.

The arterial tonometry is a transcutaneous pulse-sensing technique using a pressure transducer. External pressure to flatten the arterial wall is exerted on the patient's skin using the pressure transducer. While the wall is applanated, normal contact stress, measured by the transducer, becomes equal to the transmural pressure [31]. That is because the hoop tension of the flattened vessel wall cannot balance the transmural pressure at all. Practically, the tonometry requires a specific anatomical condition; a superficial artery should be supported by rigid structures such as a bone in order to properly applanate the target artery. Such arterial sites include the radial and possibly carotid artery. However, the carotid tonometry requires substantial expertise to obtain a reliable waveform [32]. In addition, the reliable measurement greatly depends on accurate alignment of the transducer, thus it is not suitable for real-time monitoring for a long time. Finally, the tonometry was reported unreliable in obese patients [33].

More recently, non-invasive ABP waveform estimation techniques using ultrasound have been introduced. One of the prior art is based on the empirically derived exponential relation between the pressure and the area [34]. This approach calibrates a wall rigidity coefficient to estimate an ABP trace yet lacks continuous calibration capability in case the vessel elasticity changes. Other researchers conducted quantitative tissue elastography based on a hand-held force-controlled ultrasound probe to estimate the ABP [35,36]. Other works utilize a pulse wave velocity (PWV) to quantify the vessel elasticity [37–40]. This approach tracks the vessel elasticity through continuous PWV monitoring using ultrasonography. This approach is more appealing than the volume clamping method and tonometry because it is suitable for the central ABP waveform monitoring at the abdominal aorta [38] or the carotid artery [40] to mitigate the effect of the pulse wave reflection. Besides, an ultrasound scanning device

can potentially be implemented in a portable form factor desirable in long-term and real-time monitoring aspects, which is demonstrated by the introduction of hand-held ultrasound scanners. In addition, ultrasonography allows unimpeded blood flow, desirable for the long-term monitoring. Finally, ultrasonography has been widely used for various cardiovascular diagnostics because of its safe and non-invasive nature.

1.3 Objectives of Thesis

For these reasons, this work aims to explore non-invasive ABP waveform monitoring using ultrasound embodied in a portable, low-cost ultrasound scanner for real-time and long-term monitoring. In order to further develop the potential of PWV-based ABP waveform estimation technique using ultrasound, this thesis investigates several aspects toward real-term and long-time ABP waveform monitoring. Specifically, this work states four objectives in this direction:

- To develop and validate the low-cost portable ultrasound system that can be used to acquire necessary ultrasound images for implementation of the ABP waveform estimation

- To investigate feasibility of the PWV-based ABP waveform estimation using ultrasound on healthy human subjects at the common carotid artery, one of the surrogate central sites

- To conceive and demonstrate hardware improvements of ultrasonography toward sonographer-less operation while maintaining the portable and low-cost characteristics.

- To test the accuracy of the ABP waveform estimation model on humans in comparison to the gold standard arterial-line measurement.

1.4 Thesis Organization

This thesis consists of eight chapters. Chapter 2 establishes basic background. The first section describes an acoustic theory and medical ultrasonography to acquire relevant physiological data needed to estimate the ABP waveform. The second section describes hemodynamics and cardiovascular physiology. The final section discusses specific ultrasound techniques and proposes the ABP waveform estimation method.

Chapter 3 describes the development of the prototype ultrasound scanner to implement the proposed ABP estimation technique. First, probe designs are detailed. Then, the overall architecture of the system is described, followed by implementation details. Finally, electrical and acoustic characterization as well as the operation of the system are presented.

The proof-of-concept human subject study is presented in Chapter 4. First, major considerations in the clinical use of the technique are described. Then, the clinical study results are presented, and their implications are drawn.

Chapter 5 describes the strategy of ultrasonography to achieve motion and misalignment tolerance in physiological waveforms monitoring. Unfocused imaging with wide beam insonation is introduced to achieve such a goal. Several signal and image processing approaches are discussed to mitigate the effect of increased clutter. Finally, the experimental validation with human subject' data is provided.

Chapter 6 discusses the Valsalva maneuver study which supports usefulness of the designed device with the proposed technique for stress test application. While the human subjects performed the maneuver, the hemodynamics changes were continuously monitored and compared to measurements by a volume clamping method device.

Chapter 7 shows results from the Non-invasive Evaluation of an arterial WavEform uSing ulTrasound (NEWEST) study conducted at the Boston Medical Center. This study compares the ABP waveform estimation at the carotid to the gold standard A-line measurement and estimated central ABP waveforms from model-based transfer function techniques.

Chapter 8 summarizes key contributions and suggests potential future work.

Chapter 2

Theory of Operation

This chapter lays the theoretical background for this thesis work. An acoustic wave theory and the cardiovascular system are described. An arterial blood pressure (ABP) waveform estimation technique is proposed based on hemodynamics in the arterial system. Then, ultrasonography is proposed to acquire physiological parameters as well.

2.1 Acoustic Wave Theory

Ultrasonography uses a longitudinal acoustic wave to image biological tissues. The acoustic wave is propagated and scattered, and the scattered echo delivers information about the scattering objects. This section details how the acoustic wave behaves and how to properly extract and interpret physiological information.

2.1.1 Acoustic Wave Propagation in Tissue

The acoustic wave propagates in solids and liquids through various propagation modes. Although the tissues are elastic solids, their contents mostly consist of liquids, more specifically, water. Therefore, the wave behaviors in the liquid establishes a strong basis for medical ultrasonography. For this reason, the acoustic wave is often characterized in water. In addition, in spite of the non-linearity of the tissue, the prin-

ciple of linearity is assumed in this section, which holds true when the perturbation of particles is sufficiently small, to introduce intuition on acoustic wave behaviors. More detailed descriptions of the acoustic wave theory can be found in [41].

The acoustic wave propagated in liquid is a longitudinal wave that generates a cyclic displacement (u) of particles from the equilibrium position. This perturbation produces a local pressure disturbance (p). The cycle of the increased pressure is called compressional, while the decreased pressure is called rarefactional. In an idealized incompressible fluid, the velocity of a particle (v) is defined as:

$$v = \frac{\partial u}{\partial t} \tag{2.1}$$

For the sake of convenience, a velocity potential is defined as:

$$v = \nabla \phi \tag{2.2}$$

Then, pressure (p) is defined as:

$$p = -\rho \frac{\partial \phi}{\partial t} \tag{2.3}$$

where ρ is the density of the fluid with no disturbance. Propagation of the acoustic wave is governed by a wave equation described as:

$$\nabla^2 \phi - \frac{1}{c^2} \frac{\partial^2 \phi}{\partial t^2} = 0 \tag{2.4}$$

Assuming a plane wave is propagated in the z-direction, Equation 2.4 can be rewritten in a Cartesian coordinate as:

$$\frac{\partial^2 \phi}{\partial z^2} - \frac{1}{c^2} \frac{\partial^2 \phi}{\partial t^2} = 0 \tag{2.5}$$

where the speed of sound (c) is expressed in terms of the ratio of specific heats (γ) and the isothermal bulk modulus (B_T) as:

$$c = \sqrt{\frac{\gamma B_T}{\rho}} \tag{2.6}$$

Table 2.1: Acoustic parameters in biological media [42, 43]

Medium	**Density (kg/m^3)**	**Speed of Sound (m/s)**	**Acoustic Impedance (MRayls)**
Air	1.2	333	0.0004
Water	1000	1480	1.48
Blood	1060	1566	1.66
Fat	920	1450	1.38
Muscle	1070	1580	1.70
Soft Tissue (Average)	1058	1540	1.63

The characteristic impedance (Z_C) refers to the ratio of the pressure to the particle velocity. This impedance can be expressed from Equations (2.2), (2.3), and (2.5) as:

$$Z_C = \frac{p}{v} = \rho c \tag{2.7}$$

Table 2.1 summarizes the acoustic parameters in various biological tissues. The solution of the wave equation consists of forward and backward traveling waves, and the characteristic impedance is negative for the backward wave.

An instantaneous intensity (I_{inst}) of the acoustic wave is expressed in terms of the characteristic impedance as:

$$I_{inst} = pp^*/Z_C = vv^*Z_C \tag{2.8}$$

Since the instantaneous intensity is a function of time and space, the average and maximum intensities in a temporal or a spatial domain are typically utilized to better describe the transmission of acoustic energy. In the time domain, a temporal average, a pulse average, and a temporal peak value are used [44]. In the spatial domain, a spatial peak and a spatial average value are used. The U.S. Food and Drug Administration (FDA) guides ultrasound scanner manufacturers for the safe usage of ultrasound. A spatial peak temporal average intensity (I_{SPTA}) dictates the thermal effect of medical ultrasound in tissues. On the other hand, a spatial peak

pulse average intensity (I_{SPPA}) is used to evaluate the non-thermal effect [45].

2.1.2 Acoustic Wave Scattering in Tissue

The acoustic wave gradually loses energy in real media through absorption and scattering. Absorption, similar to friction, results in local heating in media. Therefore, absorption is important for ultrasound safety because excessive heating may damage the tissues. The scattering results in changing the original trajectory of the acoustic waves. Attenuation by these processes is described by an exponential law as:

$$u(z,t) = u_0 e^{-\alpha z} e^{(kz-\omega t)} \tag{2.9}$$

where α is an attenuation factor, k is the wave number, and ω is the angular frequency. The attenuation experienced in the tissues increases as frequency increases. A typical value for the attenuation factor is reported as 0.5 dB/cm/MHz for soft tissues [44].

Scattering occurs when the acoustic wave faces inhomogeneous boundaries, more specifically, boundaries with different characteristic impedances. The echoes generated from the scattering excite an ultrasound probe to produce medical ultrasound images of anatomical structures. Mechanisms of the scattering depend on the wavelength relative to the roughness of the boundary [41]. Depending on this relation, the mechanisms are categorized as: specular, diffusive, or diffractive scattering. Specular scattering occurs when the wavelength is much smaller than the roughness. Diffusive scattering occurs when the roughness is much smaller than the wavelength. Diffractive scattering occurs between these two regimes. For example, the echoes from a vessel wall or the boundary between large organs are based on specular scattering, while the echoes from individual cells in these organs or erythrocytes (i.e., red blood cells) are described based on diffusive scattering [41].

Specular Scattering

Specular scattering, also called reflection, is understood according to a ray theory [41]. Consider a single-frequency plane wave propagating in the positive z-direction through medium 1 with the wave number and characteristic impedance of k_1 and Z_1,

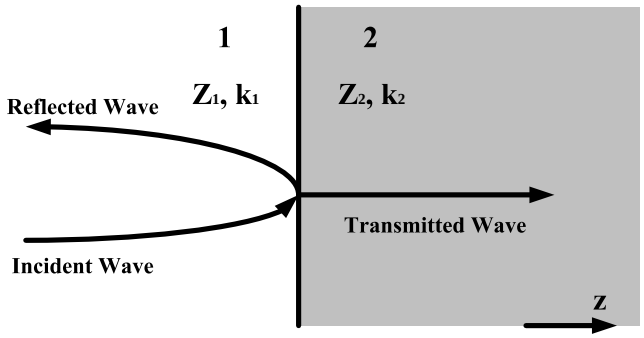

Figure 2-1: Illustration of an acoustic wave perpendicularly reflected at the boundary between media with different characteristic impedances.

respectively, It is perpendicularly reflected at a flat boundary to medium 2 with k_2 and Z_2. Due to the different acoustic properties, the reflection occurs with a reflection coefficient (Γ_a). The continuity of the pressure and velocity at the boundary dictates:

$$p_2 = p_1(1 + \Gamma_a) \tag{2.10a}$$

$$v_2 = v_1(1 - \Gamma_a) = \frac{p_1}{Z_1}(1 - \Gamma_a) \tag{2.10b}$$

where p_1 and v_1 are the pressure and particle velocity of the incident wave, respectively. Then, the characteristic impedance of medium 2 is written in terms of Γ_a and Z_1:

$$Z_2 = \frac{p_2}{v_2} = \frac{(1 + \Gamma_a)Z_1}{1 - \Gamma_a} \tag{2.11}$$

In terms of the characteristic impedances, the reflection coefficient is written as:

$$\Gamma_a = \frac{Z_2 - Z_1}{Z_2 + Z_1} \tag{2.12}$$

Finally, a transmission coefficient (τ) can be determined as:

$$\tau = 1 + \Gamma_a = \frac{2Z_2}{Z_1 + Z_2} \tag{2.13}$$

To apply the above analysis to the wave incident at an angle, let's define θ_I, θ_R,

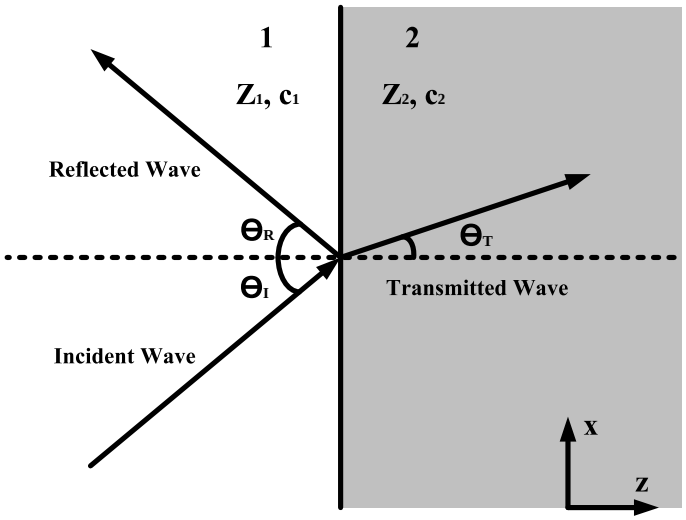

Figure 2-2: Illustration of an acoustic wave reflected obliquely at the boundary between media with different characteristic impedances [46].

and θ_T as the angles of incidence, reflection, and transmission, respectively, in Figure 2-2. Snell's law gives:

$$\frac{\sin\theta_I}{\sin\theta_T} = \frac{c_1}{c_2} \tag{2.14}$$

where c_1, c_2 are the speeds of sound in media 1 and 2, respectively. At the boundary, the tangential components of the wave numbers must be equal to the following:

$$k_x = k_1 \sin\theta_I = k_1 \sin\theta_R = k_2 \sin\theta_T \tag{2.15}$$

Due to the oblique incidence, the wave number components in the z-direction have cosine dependencies to the angles as:

$$k_{Iz} = k_1 \cos\theta_I \tag{2.16a}$$

$$k_{Rz} = k_1 \cos\theta_R \tag{2.16b}$$

$$k_{Tz} = k_2 \cos\theta_T \tag{2.16c}$$

The effective characteristic impedances are calculated as:

$$Z_{1,effective} = \frac{Z_1}{\cos\theta_I} \tag{2.17a}$$

$$Z_{2,effective} = \frac{Z_2}{\cos\theta_T} \tag{2.17b}$$

Then, the reflection and transmission coefficients are calculated from Equations 2.12 and 2.13, respectively:

$$\Gamma_a = \frac{Z_{2\theta_T} - Z_{1\theta_I}}{Z_{2\theta_T} + Z_{1\theta_I}} = \frac{Z_2\cos\theta_I - Z_1\cos\theta_T}{Z_2\cos\theta_I + Z_1\cos\theta_T} \tag{2.18a}$$

$$\tau = \frac{2Z_{2\theta_T}}{Z_{2\theta_T} + Z_{1\theta_I}} = \frac{2Z_2\cos\theta_I}{Z_2\cos\theta_I + Z_1\cos\theta_T} \tag{2.18b}$$

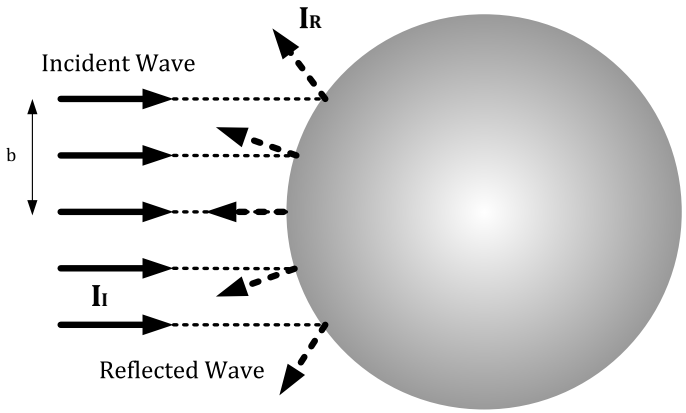

Figure 2-3: Specular scattering of a planar incident wave on a spherical object [46].

Assuming the wavefront of the reflected wave is approximately the same as the shape of the object, an intensity of the reflected wave can be calculated [41]. Consider that the plane wave of a radius b insonates a spherical object with a radius of a, which is much larger than the wavelength of the incident wave. Then, the intensity is roughly calculated as [41]:

$$\frac{I_R(r)}{I_I} \sim \frac{\pi b^2}{r^2}|\Gamma_a|^2 \tag{2.19}$$

where r is the distance from the object, and I_I is the incident intensity. The reflected

intensity is directly proportional to the square of the reflection coefficient. It is noteworthy that most of the reflected waves do not follow the same trajectory as the incident wave.

Diffusive Scattering

Diffusive scattering, also called Rayleigh scattering, occurs when individual scatterings from the boundary fail to produce a distinct interference pattern [41]. In medical ultrasound, echoes backscattered from numerous scatterers that are spaced sub-wavelength contribute to the production of a random pattern called a speckle. An intensity of the diffusively scattered wave is formulated as:

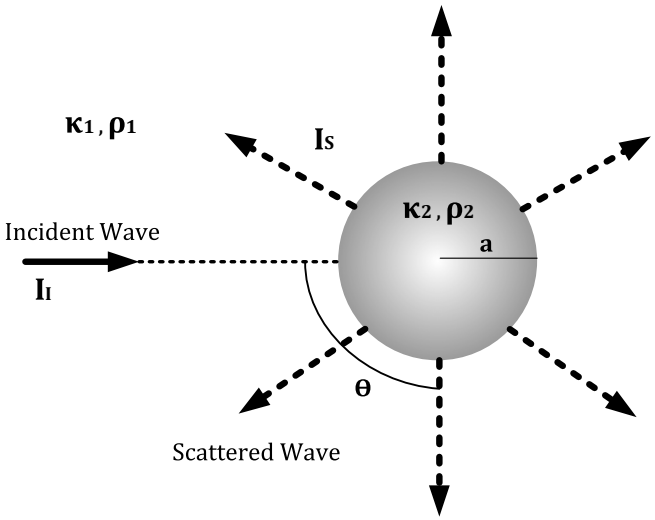

Figure 2-4: Diffusive scattering of a planar incident wave on a spherical object [46].

$$\frac{I_S(r)}{I_I} = \frac{16\pi^4 a^6}{9\lambda^4 r^2}[\frac{3(1-\rho_2/\rho_1)\cos\theta}{1+2\rho_2/\rho_1} + (1-\frac{\kappa_1}{\kappa_2})]^2 \tag{2.20}$$

where a is a radius of the spherical scatterer, θ is the angle measured from the line of incidence, ρ_1, ρ_2 are the densities of the medium and scatterer, respectively, and κ_1, κ_2 are the compressibility of the medium and scatterer, respectively, in Figure 2-4.

For the rigid scatterer, $\frac{\rho_2}{\rho_1}$ and $\frac{\kappa_1}{\kappa_2}$ goes to infinity to simplify Equation 2.20 [41]:

$$\frac{I_S(r)}{I_I} = \frac{k^4 a^6}{9r^2}[1 - \frac{3\cos\theta}{2}]^2 \tag{2.21}$$

The intensity distribution reaches its maximum at $\theta = 0$ and π, presenting a dipole-like shape. In addition, The intensity is dependent on the fourth power of the wavelength and the sixth power of the size of the scatterer. Provided a red blood cell is a bi-concave disk with a diameter of 7 μm and a thickness of 2 μm [41], the echoes from the erythrocytes are much weaker than those from the vessel wall.

2.1.3 Ultrasound Transducer

Transducer Structure

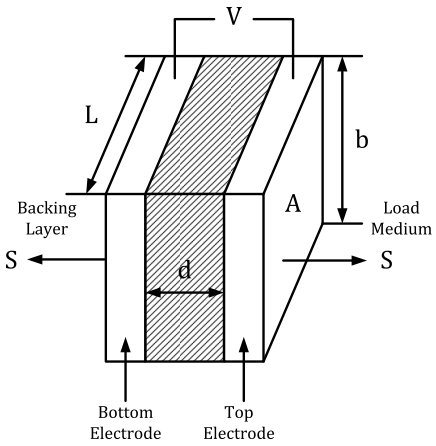

Figure 2-5: Piezoelectric element consisting of top and bottom electrodes [46].

Most commercial ultrasound probes are made of piezoelectric materials. The piezoelectric effect refers to the ability to generate electric charges in response to mechanical stress and vice versa. The simplest transducer consists of piezoelectric material with top and bottom electrodes. By applying a voltage across the electrode, an acoustic wave is generated due to the mechanical stress of the material, and the wave propagates to a load medium. Figure 2-5 depicts the physical structure of the piezoelectric element.

Electrical Impedance

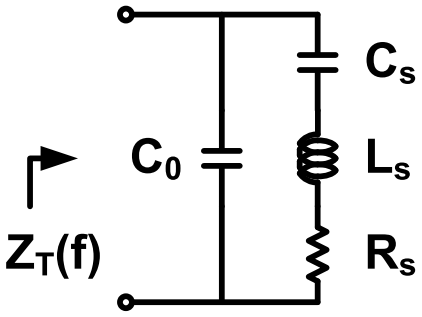

Figure 2-6: Lumped electric circuit element model for a loaded piezoelectric ultrasound transducer.

Since the piezoelectric element is dielectric, an electrical impedance seen at the voltage terminal consists of capacitance in addition to a radiation impedance. In addition, due to the stress generated in the material, the impedance changes as a function of frequency [41]. The electrical impedance is expressed in terms of the radiation impedance Z_A and a clamped capacitance C_0 as:

$$Z_T = Z_A + \frac{1}{j\omega C_0} = R_A(f) + X_A(f) + \frac{1}{j\omega C_0} \tag{2.22}$$

where R_A and X_A are the real and imaginary part of the radiation impedance, respectively. R_A represents the real power that is transmitted to the load medium, and it is maximized at a fundamental resonant frequency of the piezoelectric element (f_0), determined by its geometry where X_A becomes zero. Since the radiation impedance is a complicated function of frequency, a purely lumped model is used for the simplest transducer's electric model, which is shown in Figure 2-6. This model, often called the Butterworth-van Dyke model, presents a series resonance at $f_r = \frac{1}{2\pi\sqrt{L_s C_s}}$ and a parallel antiresonance $f_{ar} = \frac{1}{2\pi\sqrt{L_s(C_s//C_0)}}$.

2.1.4 Acoustic Pressure Field

The acoustic wave generated in the ultrasound transducer propagates to the load medium from the aperture. According to Huygen's principle, a plane wave can be

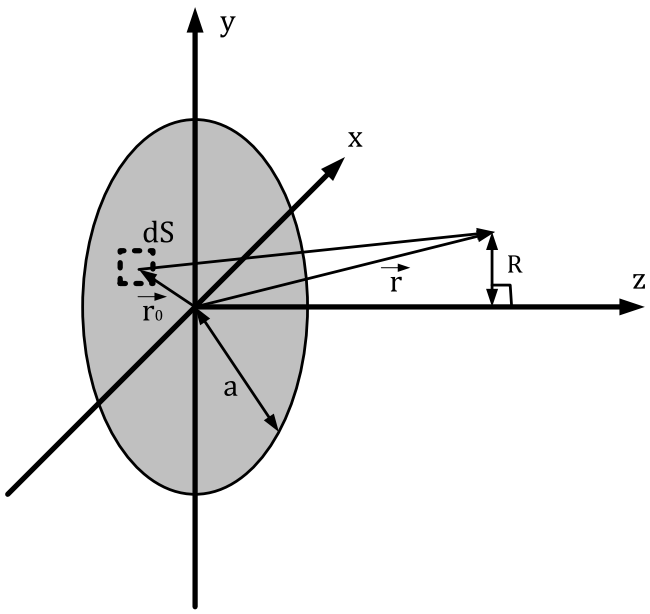

Figure 2-7: Geometric representation of a transducer aperture and its coordinates [46].

viewed as numerous spherical waves departing from point sources on the wavefront. Based on this description, individual spherical waves interfere with each other to create a distinct pattern of a field, called a diffraction pattern. Given that the wavelength of medical ultrasound ranges from 154 to 770 μm within a frequency range of 2–10 MHz, and the aperture size ranges from milimeters to a few centimeters, the pressure field insonating the tissue displays the diffraction pattern governed by the wavelength and the size of the aperture. In order to fully describe the field pattern, first, a continuous wave case is introduced, followed by modification for a pulsed wave.

Continuous Wave Pressure Field

Based on Huygen's principle, a pressure field generated by an aperture S can be described by a Rayleigh-Sommerfeld integral as [41]:

$$p(\vec{r},t) = \frac{j\rho_0 ckv_0}{2\pi}\int_S \frac{e^{i[\omega t - k(\vec{r}-\vec{r_0})]}}{|\vec{r}-\vec{r_0}|}A(\vec{r_0})dS \tag{2.23}$$

where r_0 is a position vector on the aperture, r is a position vector in space, ρ_0 is the density of the medium, $v_0 A(\vec{r_0})$ is the velocity normal to the surface, c is the speed of

sound, and k is the wave number. The parabolic approximation, also known as the Fresnel approximation, is applied as:

$$|\vec{r} - \vec{r_0}| = \sqrt{z^2 + (x - x_0)^2 + (y - y_0)^2} \simeq z[1 + \frac{1}{2}(\frac{x - x_0}{z})^2 + \frac{1}{2}(\frac{y - y_0}{z})^2] \quad (2.24)$$

Then, combining Equations 2.23 and 2.24 results in:

$$p(\vec{r}, t) = \frac{j\rho_0 ckv_0}{2\pi z} e^{i(\omega t - kz)} e^{-ik(x^2+y^2)/2z} \iint_S [e^{-ik(x_0^2+y_0^2)/2z} A(x_0, y_0)] e^{ik(xx_0+yy_0)/z} dx_0 dy_0 \quad (2.25)$$

Equation 2.25 implies that the pressure field pattern at the depth of z is the two-dimensional spatial Fourier transform of $e^{-ik(x_0^2+y_0^2)/2z} A(x_0, y_0)$, also called a near-field pattern. Furthermore, at greater depths, the Fraunhofer approximation is applied as:

$$e^{-ik(x_0^2+y_0^2)/2z} \simeq 1 \quad (2.26)$$

such that the pressure field pattern becomes the two-dimensional spatial Fourier transform of the aperture itself:

$$p(\vec{r}, t) = \frac{j\rho_0 ckv_0}{2\pi z} e^{i(\omega t - kz)} e^{-ik(x^2+y^2)/2z} \iint_S [A(x_0, y_0)] e^{ik(xx_0+yy_0)/z} dx_0 dy_0 \quad (2.27)$$

For an example of a rectangular aperture with a size of $L_x \times L_y$, Equation 2.27 is expressed as:

$$p(\vec{r}, t) = \frac{jp_0}{\lambda z} L_x L_y \frac{\sin \pi(L_x x/\lambda z)}{\pi(L_x x/\lambda z)} \frac{\sin \pi(L_y y/\lambda z)}{\pi(L_y y/\lambda z)} e^{i(\omega t - kz)} e^{-ik(x^2+y^2)/2z} \quad (2.28)$$

where p_0 is the pressure at the surface of the aperture. Then, beam width is described in a full width half maximum (FWHM) sense, and it is calculated as:

$$FWHM_{rect,x,y} = 1.206 \frac{\lambda z}{L_{x,y}} \quad (2.29)$$

Along the beam axis, the pressure amplitude is expressed as:

$$|p(0,0,z)| = 2p_0[\int_0^{\frac{L_x/2}{\sqrt{\lambda z/2}}} e^{-j\pi t^2} dt][\int_0^{\frac{L_y/2}{\sqrt{\lambda z/2}}} e^{-j\pi t^2} dt] \tag{2.30}$$

A natural focus, also known as the near-to-far field transition point, occurs at:

$$z_{max} = 0.339\frac{L^2}{\lambda} \tag{2.31}$$

if the aperture is square ($L = L_x = L_y$). Before the natural focus, the field is often called a near-field while the field beyond is called a far-field.

For an example of a circular aperture with a radius of a, Equation 2.27 is approximately expressed as:

$$p(R,z) = \frac{jp_0\pi a^2}{\lambda z}\frac{2J_1(2\pi Ra/\lambda z)}{2\pi Ra/\lambda z} \tag{2.32}$$

where R is the distance from the z-axis, and J_1 is the first order Bessel function [41]. A full width half maximum beam width is also calculated as:

$$FWHM_{circular} = 0.7047\frac{\lambda z}{a} \tag{2.33}$$

Along the beam axis, the pressure amplitude is expressed with the Fresnel approximation:

$$|p(0,z,\lambda)| = 2p_0 \sin[\frac{kz}{2}(\sqrt{1+(a/z)^2} - 1)] \tag{2.34}$$

The natural focus for the circular aperture occurs at the depth of

$$z_{max} = \frac{a^2}{\lambda} \tag{2.35}$$

Equations 2.31 and 2.35 show that the natural focus for the flat aperture only depends on the aperture size and the wavelength.

Figure 2-8 presents pressure field patterns of the circular aperture in a lateral and an axial dimension. The axial pattern shows many peaks and valleys as expected in a near-field pattern. After the natural focus, the pressure amplitude monotonically

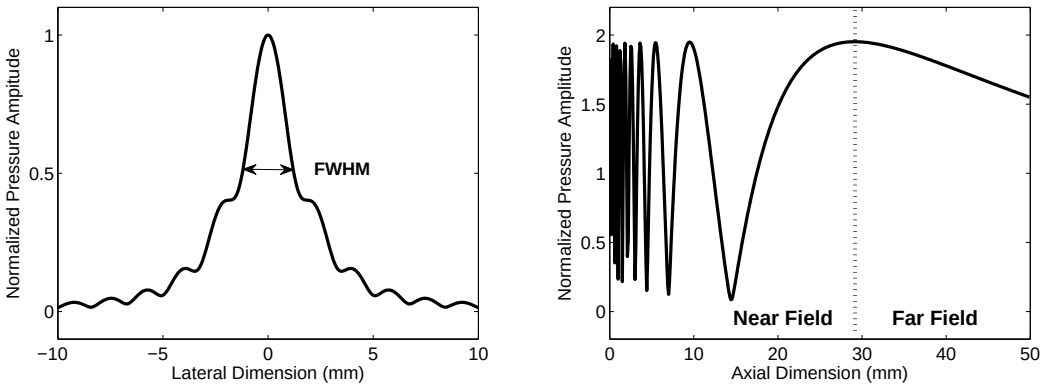

(a) Radial dimension pattern at z_r (b) Axial dimension pattern

Figure 2-8: Simulated pressure field patterns in a radial and an axial dimension for a circular aperture of 3 mm radius at a continuous 5 MHz ultrasound.

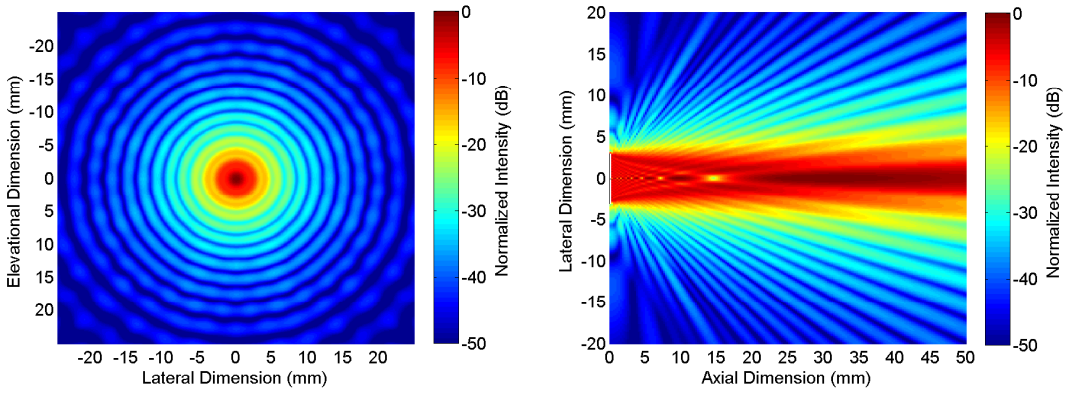

(a) $x-y$ plane (b) $x-z$ plane

Figure 2-9: Simulated temporal-averaged intensity fields in a lateral-elevational dimension and a lateral-axial dimension for a circular aperture of 3 mm radius at a continuous 5 MHz ultrasound.

decreases. This is because the natural focus is the point where significant constructive interference occurs for the last time. The simulated pattern generally agree with Equation 2.34, although a slight discrepancy is observed.

The radial pattern presents acoustic energy that is focused compared to the size of the aperture. It generally agrees with Equation 2.32. In general, the beam width determines the lateral resolution of ultrasound images. For a single element transducer, the beam width is minimum at the natural focus, and it is fixed by the wavelength

and the aperture size. Therefore, given the fixed aperture, the natural focus depth can only be controlled by the wavelength. For a transducer array, which commercial ultrasound scanners use, the focus can be defined through beamformation in the near-field. Figure 2-9 shows two-dimensional maps of the pressure fields produced by a circular aperture of 3 mm radius radiating a 5 MHz acoustic wave.

Pulsed Wave Pressure Field

Although the pressure field pattern in the continuous wave provides insights about how the diffraction pattern looks, most medical ultrasound is practiced using a pulsed wave to preserve depth-specific information. Similar to the continuous wave, the Rayleigh integral, based on Huygen's principle, is used to express the pressure field as [42]:

$$\begin{aligned} p(\vec{r},t) &= \frac{\rho_0}{2\pi}\int_S \frac{\partial v_n(\vec{r_0}, t-\frac{|\vec{r}-\vec{r_0}|}{c})/\partial t}{|\vec{r}-\vec{r_0}|}dS \\ &= \rho_0 v_n(t) * \frac{\partial}{\partial t}\int_S \frac{\delta(t-\frac{|\vec{r}-\vec{r_0}|}{c})}{2\pi|\vec{r}-\vec{r_0}|}dS \\ &= \rho_0 v_n(t) * \frac{\partial h(\vec{r},t)}{\partial t} \end{aligned} \tag{2.36}$$

where h is a spatial impulse response. The spatial impulse response is expressed as:

$$h(\vec{r},t) = \int_S \frac{\delta(t-\frac{|\vec{r}-\vec{r_0}|}{c})}{2\pi|\vec{r}-\vec{r_0}|}dS \tag{2.37}$$

It characterizes the pressure field pattern determined by specific transducer geometry assuming that the surface velocities are uniform across the aperture. It is also interpreted as a response at the aperture produced by an impulse point source in space using the acoustic reciprocity theorem [42]. The reciprocity theorem states that a transmitter and a receiver are interchangeable. This theorem can also be generalized for multiple transmitters and receivers. Using this theorem, Equation 2.37 can be viewed as a summation of the numerous point receivers on the aperture from the impulse radiated by a point source in space. Once the spatial impulse response is calculated, the pulsed field pattern ($p(\vec{r},t)$) can be easily calculated for various pulse

excitation conditions ($v_n(t)$), as implied in Equation 2.36.

So far, the pressure fields generated by acoustic sources have been discussed, but medical ultrasound images are constructed not only through pulse transmission but also echo reception. Most echoes in the images originate from diffusive scattering from mild tissue inhomogeneity. In this case, the backscattered echoes are considered spherical waves from individual point scatterers in the tissue. Then, the same spatial impulse response can be used to characterize reception [42]. Accounting for the tissue inhomogeneity $f_m(\vec{r})$, such intuition can be formulated as:

$$p_r(\vec{r}, t) = v_{pe}(t) *_t f_m(\vec{r}) *_r h_{pe}(\vec{r}, t) \tag{2.38}$$

where $*_t$ is a temporal convolution, $*_r$ is a spatial convolution, and $h_{pe}(\vec{r}, t)$ is a pulse-echo impulse response [42]. The FIELD II simulator, the ultrasound simulator used in this work, is based on this principle [47, 48].

2.1.5 Medical Ultrasonography

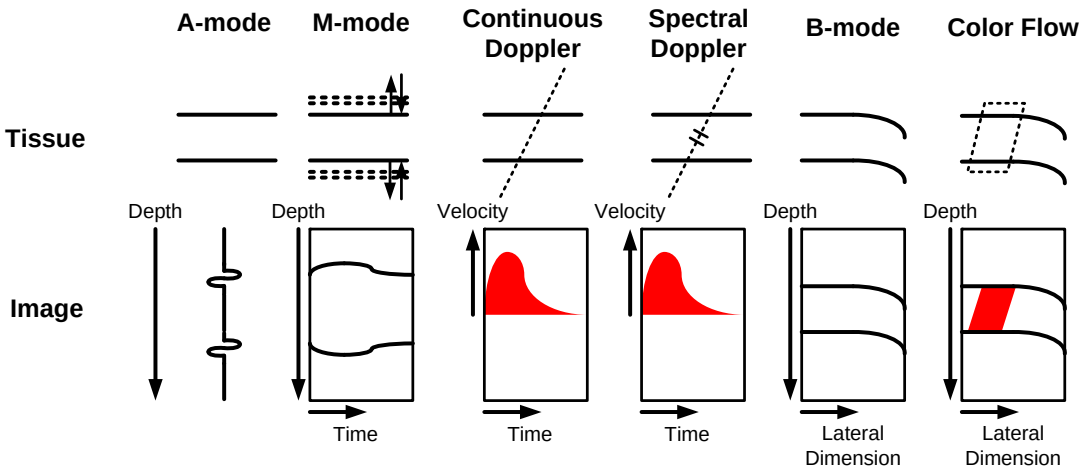

Figure 2-10: Illustration of different ultrasound imaging modes for arterial vessel imaging.

Medical ultrasound employs pulse-echo operation to scan biological tissues to extract clinically relevant information. Figure 2-10 illustrates various imaging modes.

A-mode, currently obsolete, is the most basic imaging mode merely based on the pulse-echo operation. M-mode comprises continuous A-mode operations over time with multiple pulse transmissions while the image is displayed in grayscale, based on the strength of the received echo. M-mode achieves a fine temporal resolution, as the beam is transmitted to and received from a fixed direction. Due to its superior temporal resolution, it is used to visualize fast-moving structures such as arterial vessel walls or heart valves.

Continuous and spectral Doppler measure blood flow based on the Doppler effect of the received wave. The continuous Doppler is useful to acquire an extremely high velocity jet from a stenotic valve because it is free of aliasing. However, it loses depth-specific information when the transmitted and received beam directions are the same. On the contrary, the spectral Doppler measures blood flow at a specific depth. However, the spectral Doppler is unsuitable for measuring high-flow velocities.

B-mode offers a two-dimensional image by scanning the transmitted and received beams in the field of view. The image is updated at a certain frame rate, yet its temporal resolution is generally limited compared to the M-mode. Finally, a color flow mode visualizes a flow velocity map overlaid on a simultaneously acquired B-mode image. Between the B-mode image acquisition, separate beams are transmitted at an angle multiple times and swept through a region of interest to acquire Doppler signals. Dissimilar to the continuous or spectral Doppler, the color flow quickly calculates the mean Doppler shifts in the elemental sample volumes (i.e., volume where the acoustic signal is acquired) and produces the two-dimensional flow map. This mode is particularly useful to grasp overall flow patterns in conjunction with anatomical structures imaged by B-mode.

In this work, mainly the M-mode and spectral Doppler are utilized to monitor arterial pulsation and blood flow velocities at a target artery, respectively. How the flow velocity and diameter are continuously monitored is detailed in Section 2.3.

2.2 Cardiovascular System

This section describes the hemodynamics of the arterial system and cardiovascular physiology, which are crucial to understanding acquired physiological information using ultrasound.

2.2.1 Hemodynamics

This subsection describes the hemodynamics of the arterial system. First, the mechanics of blood flow is described. Then, an analogy of the arterial system to an electric circuit is introduced. Then, pulse wave behaviors in the arterial system are visited.

Static Blood Flow Physics

Fluid is first assumed incompressible on a macroscopic scale. In this case, a volumetric flow rate (Q) at any point along a rigid cylindrical tube must be constant, expressed as the continuity equation:

$$\frac{\partial Q}{\partial x} = 0 \tag{2.39}$$

where the x-axis is parallel to the axis of the cylinder.

The fluid has viscosity or internal friction between the layers moving at different velocities. Because of the viscosity, a pressure gradient needs to push the fluid inside the tube. In Figure 2-11, the fluid fills the space between the top and bottom plate

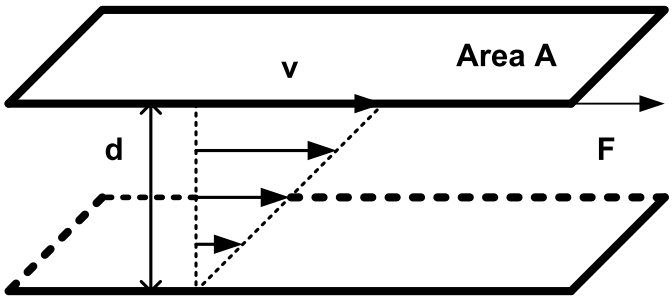

Figure 2-11: Schematic of viscous drag of the fluid at constant flow when the top wall slides to the right with a fixed velocity [42].

where the top plate is moving at a constant velocity of v to the right. To drag the top plate, a constant force (F) is applied. A shear stress is defined as a ratio of the force to area (A), and it is directly proportional to a velocity gradient across the plates, expressed as:

$$\frac{F}{A} = \mu \frac{dv(y)}{dy} = \mu \frac{v}{d} \tag{2.40}$$

where d is the distance between the plates and μ is a coefficient, called viscosity. The viscosity of water at 20.2 °C is 0.001 kg/[m·s] or 1.0 cP. Blood, which behaves as a non-Newtonian fluid, shows variations of the viscosity depending on hematocrits and the size of the conduit [49]. Although the reported viscosity of blood varies among literature, the typical value at 37 °C with a hematocrit of 45% is 4.0 cP.

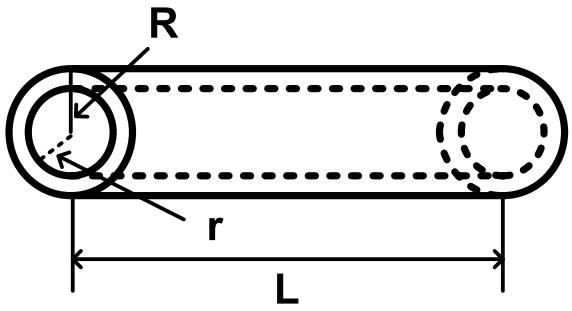

Figure 2-12: Schematic of a cylindrical tube.

In the cylindrical rigid tube with a radius R and a length L, as shown in Figure 2-12, the pressure gradient (ΔP) is applied between the inlet and outlet. Due to the symmetry, the velocity profile (v) is the function of the distance (r) from the tube's center. The shear stress on the side wall of a cylindrical fluid column with a radius r is expressed as:

$$\frac{F_{shear}}{2\pi r L} = \mu \frac{dv(r)}{dr} \tag{2.41}$$

This shear force (F_{shear}) on the fluid column balances against the force that originated from the pressure gradient as:

$$F_{shear} = 2\pi r L \mu \frac{dv}{dr} = \pi r^2 \Delta P \tag{2.42}$$

Solving Equation 2.42 with a boundary fluid velocity of zero, the velocity profile is calculated as:

$$v(r) = \frac{\Delta P R^2}{4L\mu}(1 - \frac{r^2}{R^2}) = v_0(1 - (\frac{r}{R})^2) \tag{2.43}$$

where v_0 is the maximum flow velocity at the center. Equation 2.43 implies that the parabolic profile with constant flow is developed in a steady state. The volumetric flow rate is calculated by integrating the velocity over the cross-section as:

$$Q = \int_0^R 2\pi r v dr = \frac{\Delta P \pi R^4}{8L\mu} \tag{2.44}$$

This equation, also known as the Poiseuille's law, implies that the flow rate in the fully developed laminar flow is directly proportional to the pressure gradient, which resembles Ohm's law in electric circuits. A flow resistance (R_f) is defined as a ratio of the pressure gradient to flow rate, and it is expressed in the fully developed parabolic flow:

$$R_f = \frac{8\mu L}{\pi R^4} \tag{2.45}$$

Equation 2.45 indicates that the flow resistance is inversely proportional to the fourth power of the radius of the tube. In the arterial system, the flow resistances of major arteries are negligible because their diameters are large. Hence, negligible pressure drop occurs through the large arteries. On the other hand, the resistances at the arterioles and capillaries are significantly higher due to their small sizes. Consequently, a large pressure drop occurs through arterioles and capillary beds.

In fact, when the fluid flows from a large reservoir to the tube, the velocity profile is a plug profile at the inlet (i.e., a flat profile) and then gradually transforms to a parabolic profile as the viscous effect happens. In the middle, an intermediate profile is described approximately in terms of the Poiseuille's coefficient (p_0) as:

$$v(r) = v_0(1 - (\frac{r}{R})^{p_0}) \tag{2.46}$$

With this Poiseuille profile, a spatial mean flow velocity (i.e., average flow velocity

across the cross-section) is expressed as:

$$\bar{v} = \frac{1}{\pi R^2} \int_0^R v_0 \Big(1 - (\frac{r}{R})^{p_0}\Big) \times 2\pi r dr = v_0 \frac{p_0}{p_0 + 2} \tag{2.47}$$

Pulsatile Blood Flow Physics

The blood flow in the arterial system is pulsatile because of the heart's pumping and arterial compliance. The pressure gradient that drives the flow not only counteracts the viscous drag but the inertia of the fluid to accelerate. Such intuition is implied in two Navier-Stokes equations, assuming there is no circumferential motion [50]:

$$-\frac{dP}{dx} = \rho(\frac{dv}{dt} + u\frac{dv}{dr} + v\frac{dv}{dx}) - \mu(\frac{d^2v}{dr^2} + \frac{1}{r}\frac{dv}{dr} + \frac{d^2v}{dx^2}) \tag{2.48a}$$

$$-\frac{dP}{dr} = \rho(\frac{du}{dt} + u\frac{du}{dr} + v\frac{du}{dx}) - \mu(\frac{d^2u}{dr^2} + \frac{1}{r}\frac{du}{dr} + \frac{d^2u}{dx^2} - \frac{u}{r^2}) \tag{2.48b}$$

where v is a longitudinal flow velocity and u is a radial flow velocity. The first three terms of both equations represent the acceleration, while the latter terms represent the internal friction. Although a complete solution of the Navier-Stokes equations is not always available, a useful analytical model can be derived by analyzing the laminar flow in a rigid tube, also called Womersley's model [50]. Then, Equation 2.48b is ignored. Furthermore, Equation 2.48a is reduced to result in:

$$-\frac{dP}{dx} = \rho(\frac{dv}{dt}) - \mu(\frac{d^2v}{dr^2} + \frac{1}{r}\frac{dv}{dr}) \tag{2.49}$$

Womersley's model assumes a sinusoidal pressure gradient with an amplitude of B. Then, the longitudinal velocity and volumetric flow rate are calculated as:

$$v(r,t) = Real[\frac{|B|e^{j\omega t}R^2}{j\alpha^2\mu}(1 - \frac{J_0(j^{3/2}\alpha\frac{r}{R})}{J_0(j^{3/2}\alpha)})] \tag{2.50}$$

$$\begin{aligned} Q(t) = \frac{|B|\pi R^4}{\mu} \cdot \frac{M'_{10}}{\alpha^2} \cos(\omega t - \phi - [90^\circ - \epsilon'_{10}]) \\ (M'_{10}e^{j\epsilon'_{10}} = 1 - \frac{2J_1(j^{3/2}\alpha)}{j^{3/2}\alpha J_0(j^{3/2}\alpha)}) \end{aligned} \tag{2.51}$$

where α is defined as the Womersley number ($\alpha = R\sqrt{\frac{\rho}{\mu}\omega}$) [50,51]. Figure 2-13 shows a time-varying velocity profile predicted by Womersley's model during a single cardiac cycle. The model allows a bi-directional velocity profile at a certain time, which is dissimilar to the Poiseuille profile. In fact, at the aortic valve closure, slight backflow can be observed at the carotid artery, while most of flow velocities point downstream, resulting from a complicated interplay of the acceleration and viscous drag. The appearance of this interplay varies with the phase in the cardiac cycle and the types of arteries. At the major arteries, due to the insignificant flow resistance, the inertial behavior of the fluid dominates, especially during the systole (i.e., contracting phase of the left ventricle). As a result, a plug profile is formed at the ascending aorta. During the diastole (i.e., relaxing phase of the left ventricle), the profile is more developed toward a parabola. On the other hand, at the smaller arteries, the viscous drag becomes comparable to the inertia such that the profile reaches a parabolic profile, especially during the diastole. Overall, Womersley's model better reflects reality than Poiseuille's profile.

Womersley's model for an elastic tube better mimics the fluid behaviors [52], and the resulting solution is similar to Equations 2.50 and 2.51. A detailed description can be found in [50, 52].

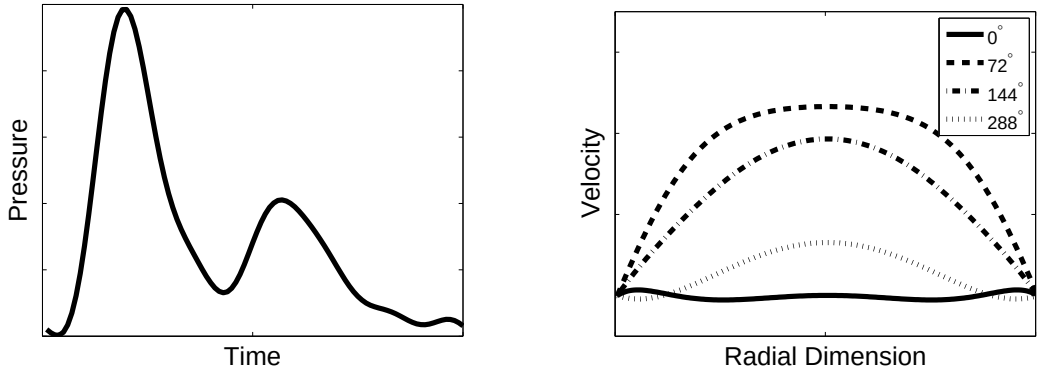

(a) ABP waveform in a cardiac cycle

(b) Velocity profile variation over a cardiac cycle

Figure 2-13: Simulation of the Womersley's pulsatile velocity profile in different cardiac phases [46].

Pulse Wave Propagation

Poiseuille's law resembles Ohm's law in electric circuits as seen in Equation 2.44. Womersley's model, as expressed in Equation 2.51, also suggests that the impedance can be defined as a ratio of the pressure to the volumetric flow rate analogous to an impedance in the electric circuits. In this analogy, the pressure and flow correspond to voltage and current, respectively.

In fact, Equation 2.48a is reduced by neglecting convective acceleration terms; that is, the longitudinal velocity is unaffected by radial oscillations, and the viscous terms can be expressed as a lumped flow resistance times the volumetric flow rate (Q):

$$-\frac{dP}{dx} = RQ + L\frac{dQ}{dt} \simeq L\frac{dQ}{dt} \tag{2.52}$$

where R is the flow resistance per length and L is the inertance of blood per length, also expressed as $\frac{\rho}{A}$. In large arteries, the flow resistance can be ignored. In addition, the continuity equation in the elastic vessel suggests:

$$-\frac{dQ}{dx} = \frac{dA}{dt} = \frac{dA}{dP}\frac{dP}{dt} = C\frac{dP}{dt} \tag{2.53}$$

where A is a cross-sectional area and C is the volume compliance per length, also called the arterial compliance. By combining Equations 2.52 and 2.53, it can be shown that both P and Q meet the wave equation, suggesting propagation of the pressure and flow wave along the elastic vessel. This is called pulse wave propagation. The propagation speed, also called a pulse wave velocity (PWV), is expressed by the Bramwell-Hill equation [53]:

$$PWV = \sqrt{\frac{1}{LC}} = \sqrt{\frac{A}{\rho}\frac{dP}{dA}} \tag{2.54}$$

The pulse consists of pressure and flow components. Analogous to the transmission line, a characteristic impedance is defined as the ratio of the pressure to the flow in the propagating wave. The characteristic impedance is expressed as:

$$Z_C = \sqrt{\frac{L}{C}} = \sqrt{\frac{\rho}{A}\frac{dP}{dA}} \tag{2.55}$$

Table 2.2: Analogy of pulse wave propagation in an elastic tube to an electric transmission line [46, 50]

Elastic Tube	**Transmission Line**
Pressure (P)	Voltage (V)
Flow (Q)	Current (I)
Inertia ($\frac{\rho}{A}$)	Unit length inductance (L)
Compliance ($\frac{dA}{dP}$)	Unit length capacitance (C)

Table 2.2 summarizes the analogy between the conduit arterial vessel to the electric transmission line. Since the characteristic impedance is dependent on the cross-sectional area and arterial compliance, the pulse wave is reflected where impedance mismatch occurs. Minor wave reflections may occur as the arterial tree successively branches out. Typically, the arterial branching is well matched for the forward-traveling wave [54]. However, due to the sudden decrease of the area at the arterioles, major reflections occur. Since the arterioles have high resistances, the reflection coefficient is positive, causing pressure augmentation.

Human Arterial System Model

The arterial system is often modeled by using lumped electric circuit elements. A resistor represents the flow resistance, and a capacitor models the compliance of the system, meaning that the system reserves blood as the transmural pressure increases. The heart is modeled by a current or a voltage source.

From this representation, the two-element Windkessel model consists of a capacitor, mimicking total arterial compliance in parallel with a resistor, representing systemic vascular resistance [3]. It assumes the arterial pressure is the same throughout the entire system. Given that the heart is modeled by a current source enabled only during the systole, the pressure ramps up during the systole, followed by an exponential decay during the diastole, dictated by a time constant. In addition to this model, a diode, for an aortic valve, may be added if the heart is modeled by a voltage source.

Instead, the arterial system can also be modeled by a tree of transmission lines

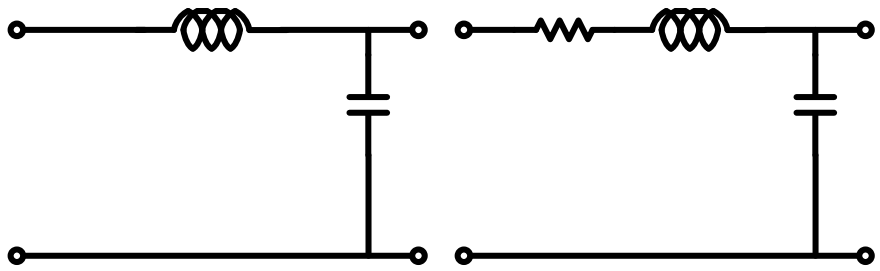

(a) Lossless (b) Flow resistance

Figure 2-14: Schematics of various electric circuit models for an elemental arterial vessel segment [50].

rooted from the heart. The most distal branches are usually terminated with load impedances. Figure 2-14 shows various electric circuit models for an elemental arterial vessel segment [50]. A lossless model only includes inertance and compliance without energy loss elements. This model is adequate for major arteries as the flow resistance is negligible. At the smaller arteries, the flow resistance becomes comparable to the behavior of inertia such that the model with a resistor in series to the inductor fits.

The terminal load impedance is described again by the two-element Windkessel model, where the capacitor represents the downstream arterial compliance while the resistor represents the downstream flow resistance.

This tree model, due to pulse wave propagation, suggests the arterial pressure may not necessarily be the same at different arterial sites. An ABP waveform shape is determined by adding the forward and backward traveling reflected pulse wave. At the distal sites, these two waves are augmented in a time-aligned manner. On the other hand, at the proximal sites, these waves are superposed with a round-trip delay of the pulse wave to create a less augmented shape. In addition, this delay is determined by the distances to major reflection sites as well as the pulse wave velocity. Due to this phenomenon, it has been reported that the pulse pressure at the distal sites is higher than at the central sites [50], called pulse pressure amplification. Figure 2-15 shows the change of the arterial blood pressure and flow waveform as the measurement site progressively moves downstream. The distal site shows a sharper systolic peak of the ABP waveform, while the proximal site shows a sharper systolic

peak of the flow waveform.

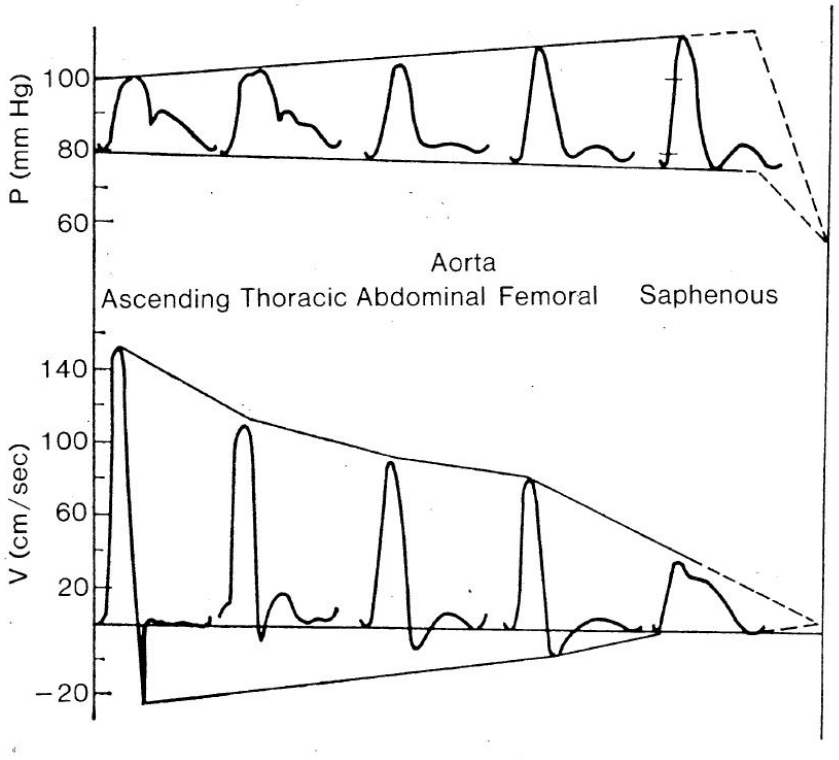

Figure 2-15: Pressure (above) and blood flow velocity (below) of arteries in a dog [50].

2.2.2 Cardiovascular Physiology

Arterial System Anatomy

The circulatory system consists of arteries, capillaries, and veins. The systemic circulation is driven by the pressure gradient between the arterial and venous sides. This gradient is maintained through the endless pumping of the heart.

The primary role of the arterial system is to store and deliver oxygenated blood and nutrients to various parts of the body as needed without stressing the organs. During systole, the blood ejected from the heart enters the arterial system and flows downstream, and intravascular volume and transmural arterial pressure increase as a result. During diastole, the stored blood continues to flow downstream as the intravascular volume and pressure gradually decrease. In this way, the system continuously

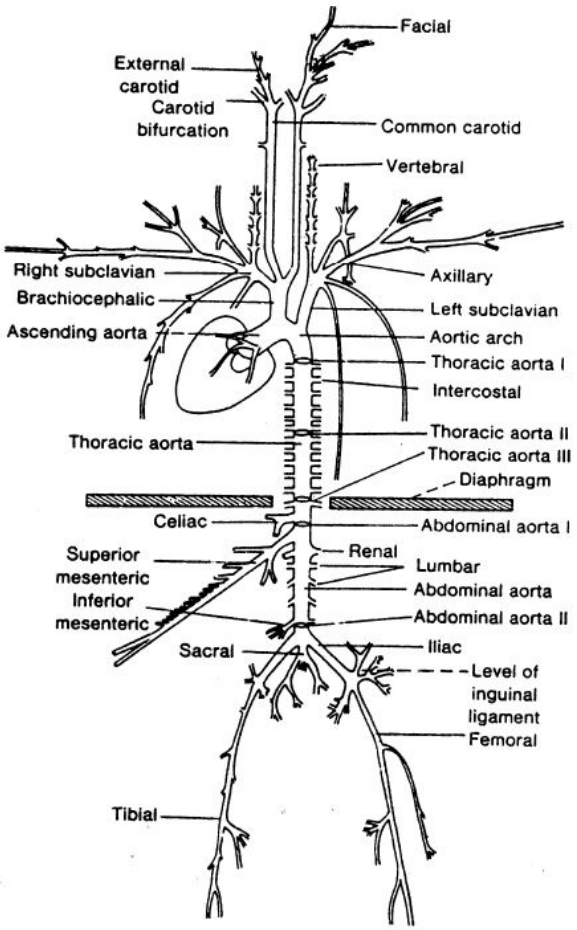

Figure 2-16: Illustration of the structure of the human arterial tree [54].

delivers the blood for an entire cardiac cycle. It also cushions the high pulsatile stress generated by the ventricular contraction. Otherwise, the capillaries and the organs would be damaged unless the stress is smoothed by the arterial system. The arterial tree provides pathways for this delivery as shown in Figure 2-16.

About a sixth of cardiac output (CO; average blood volume ejected from the heart per minute) goes to cerebral vasculatures from the ascending aorta, aortic arch, and to common carotid arteries (CCA) or vertebral arteries [26]. The left CCA directly branches out from the aortic arch, while the right CCA branches out from the brachiocephalic trunk. The CCAs further branch out to the internal (ICA) and external (ECA) carotid arteries. The ICA mainly carries blood to the brain, while

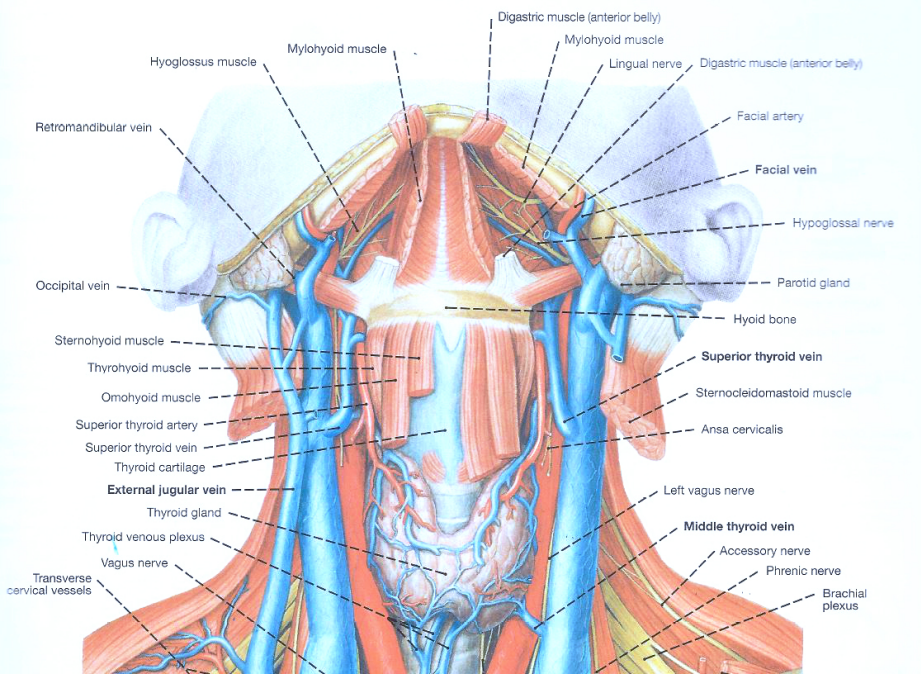

Figure 2-17: Illustration of the vascular structure in the neck [55].

the ECA supplies a blood to facial tissues. Adjacent to the carotid arteries, jugular veins are located, as shown in Figure 2-17.

A quarter of the cardiac output goes to skeletal muscles, and 5% goes to the skin. The rest goes to other organs, such as the intestines or the kidney. The skeletal muscle in the arm is perfused by the artery from the aortic arch, the brachiocephalic trunk, subclavian arteries, brachial arteries, and radial or ulnar arteries. The blood travels to lower extremities through the aortic arch, descending aorta, thoracic aorta, and abdominal aorta to iliac, tibial, and femoral arteries. Reported physical properties of the various arterial vessels are summarized in Table 2.3.

Among the aforementioned arteries, the potential target vessel in this work includes the common carotid artery, brachial artery, and radial artery. They are relatively superficial and convenient for ultrasound scanning. The common carotid artery is attractive due to its size, anatomy, and proximity to the aorta. Prior art demonstrated that the pulse wave contour at the carotid artery is very similar to that at the aorta [57]. The other sites can also be compelling because the sphygmomanometer

Table 2.3: Reported arterial vessel radius and compliance of the major arteries [56].

Name	**Distal Radius (cm)**	**Arterial Compliance (10^{-1}cm^4/N)**
Ascending Aorta	1.440	26,100
Subclavian Artery	0.423	1,647
Common Carotid Artery	0.370	1,207
Brachial Artery	0.236	803
Femoral Artery	0.190	308
Radial Artery	0.142	80

targets the brachial artery, and the arterial line is performed at either the radial or femoral sites.

Arterial Vessel Anatomy

Unlike the veins and capillaries, the arterial wall is thick in order to endure high mechanical stress. The artery is often modeled as an elastic tube, but the elastic property of the arterial wall is more complicated than a pure elastic tube.

The arterial vessel wall mainly consists of endothelium, elastin, collagen, and smooth muscles [54]. A cross-section of the wall presents three distinct layers: the innermost tunica intima, tunica media, and adventitia. The tunica intima is mainly composed of a thin layer of endothelial cells. The endothelium provides a smooth surface for blood flow, and its sensory function also serves for smooth muscle control [58]. However, its contribution to the elastic property is negligible.

The thick tunica media contains all major components except the endothelium. Elastin is an extensible material whose elastic modulus is reported 1–6 N/cm^2 [54]. Collagen is much stiffer than elastin, as its Young's modulus is 400–1000 times higher [54, 58]. In fact, collagen has little effect on the elasticity until the vessel is sufficiently dilated. In other words, collagen is crucial to understanding the pressure-dependent elasticity. Finally, the smooth muscle produces tensions when it is excited by physiological or pharmacological stimuli.

The variation in the composition of these elements differentiates an elastic and a muscular artery. The central artery contains elastin abundantly with a limited amount of smooth muscle. Most arterial compliance is provided by the central artery

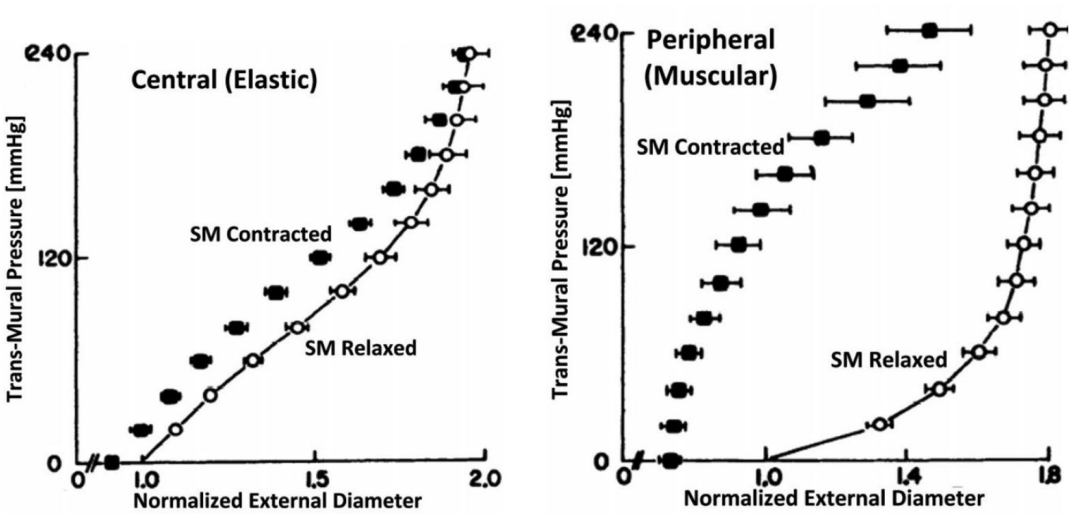

(a) Central Elastic Artery (b) Peripheral Muscular Artery

Figure 2-18: Relationships between transmural pressure and a vessel diameter in the central elastic artery and peripheral muscular artery [58].

while their elasticity is much less regulated by an autonomic nervous control, as seen in Figure 2-18. The central artery is suited for storing the ejected blood by increasing intravascular volume. On the other hand, smooth muscle is the most prevalent in the peripheral artery, and its collagen content is higher than in the central artery. Consequently, its size and elasticity are strongly controlled by the nervous system, and its compliance shows higher pressure dependence, as shown in Figure 2-18. The peripheral artery is suited to control the blood flow downstream.

While arterial compliance depends on composition, the arterial wall presents time-dependent elasticity due to viscoelasticity. This originates from the stress-relaxation of viscoelastic materials [54]. The viscoelastic behavior produces a hysteresis in the pressure-diameter relation as shown in Figure 2-19, which leads to phase shifts between them. This hysteresis implies viscous loss during the repeated pulsation of the vessel.

Regulation of Arterial Pressure

In order to maintain proper blood supply to individual organs with ever-changing metabolic needs, the arterial system strategizes to control blood flow through the arterioles' local vasomotor tones, while the arterial pressure is regulated at a constant

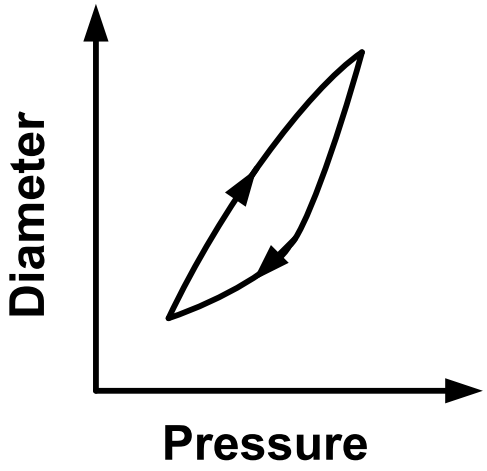

Figure 2-19: Qualitative illustration of a hysteresis loop between an arterial diameter and pressure due to viscoelasticity of the vessel wall [54].

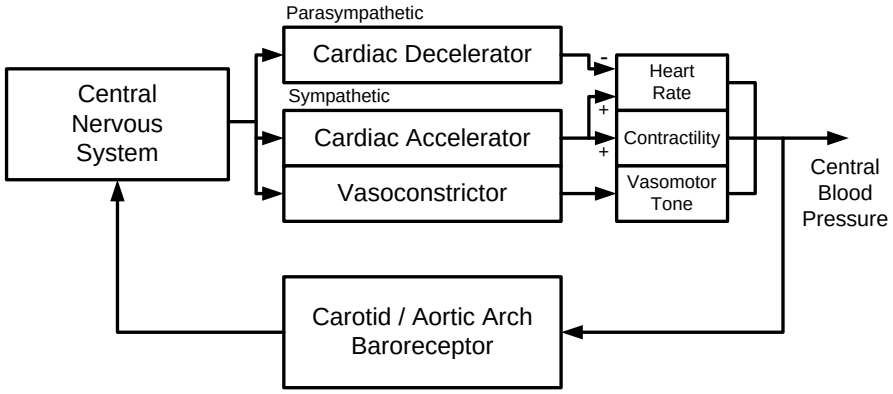

Figure 2-20: Block diagram of cardiovascular control mechanisms to maintain central blood pressure at a constant level [26].

level. Since the peripheral vessels leading to the organs are connected in parallel, the central arterial pressure becomes the primary target for regulation [26].

Arterial pressure is regulated by two mechanisms: the baroreflex and a renin-angiotensin-aldosterone system. The latter mechanism, orchestrated by the hormones, acts across a longer time scale by modulating total intravascular volume. On the contrary, the former mechanism works much quicker to react to various stimuli, such as sudden postural changes.

Figure 2-20 illustrates a feedback loop that regulates the central blood pressure through baroreflex. Baroreceptors, cells that sense blood pressure, are mainly located at the aortic arch and the carotid sinus. The baroreceptors send signals to the central nervous system, which determines which effector mechanisms to stimulate. The effectors modulating heart rate, contractility or the vasomotor tone are stimulated by either sympathetic or parasympathetic nerves. For instance, the decreased pressure leads to the increase of sympathetic activities, resulting in an elevated heart rate, increased stroke volume (i.e., the amount of blood volume ejected per beat) through an increased contractility, and the increase of a systemic vascular resistance through vasoconstriction. These effects lead to the increase of cardiac output and vascular resistance to bring the decreased pressure to the normal. Since the feedback loop presents a delay, the central pressure often presents a distinctively periodic variation, called a Mayer wave, with a period of about 10 seconds [25].

2.3 Arterial Pressure Waveform Estimation

This section details the arterial pressure waveform estimation technique based on the pulse wave velocity. Measurements of relevant physiological parameters using ultrasound to make the estimation are also described.

2.3.1 Arterial Pressure Waveform Estimation using Pulse Wave Velocity

The vessel cross-sectional area changes in response to transmural pressure changes. Arterial compliance ($\frac{dA}{dP}$) sets the incremental relationship between the pressure and area. In principle, the ABP waveform is estimated by continuous monitoring of arterial pulsation and vessel elasticity, represented by the pulse wave velocity (PWV). Equation 2.54 implies that the PWV is determined by the arterial compliance ($\frac{dA}{dP}$)

and area (A). Assuming the PWV is constant, Equation 2.54 can be solved as:

$$P(t) - P_{dia} = \rho PWV^2 \ln(\frac{A(t)}{A_{dia}}) \tag{2.56}$$

where P_{dia} is the diastolic pressure and A_{dia} is the diastolic area. In order to establish an accurate relation between the pressure and area, the local PWV should be measured since the PWV varies along different arterial sites.

More accurately, the PWV also varies within a cardiac cycle, since the transmural pressure changes induce change of compliance due to the collagen [59], as discussed in Section 2.2. If the incremental PWVs at different areas were measured, the estimation model could be modified as:

$$\begin{aligned} PWV(A) &= \sqrt{\frac{A}{\rho}\frac{dP}{dA}} \\ dP &= \rho PWV(A)^2 \frac{1}{A} dA \\ P(t) - P_{dia} &= \rho \int_{A_{dia}}^{A(t)} \frac{PWV(A)^2}{A} dA \end{aligned} \tag{2.57}$$

while still neglecting the viscoelasticity. In this work, an estimation model with a constant PWV, expressed in Equation 2.56, is used. The average PWV represents the average arterial compliance is to be measured. To implement the proposed ABP waveform estimation, continuous monitoring of the local PWV and arterial pulsation is needed.

Several local PWV estimation techniques have been introduced. First, a pulse transit time method calculates the local PWV by measuring a transit time of the pulse between two locations with a known distance during a reflection-free period [60]. However, to faithfully capture the fast-traveling pulse wave within a localized region of interest and to monitor the arterial cross-sectional area, a high frame rate ultrasound system is required.

Another method utilizes the temporal and spatial gradient of the pulse wave during the reflection-free period [61]. Since the pulse wave satisfies the wave equation, a

distension waveform can be written as a form of $f(kx - \omega t)$. The local PWV is evaluated from the ratio between the angular frequency (ω) and the wave number (k). This method also requires a high temporal and spatial resolution to calculate these gradients accurately.

The other method, called a flow-area method, measures the local PWV from the slope during the reflection-free period in a flow-area loop [62]. This method measures the local PWV at a single arterial site. To detail this method, the characteristic impedance during the reflection-free period is also expressed as the incremental ratio of the pressure to the flow ($\frac{dP}{dQ}$) such that the local PWV can be expressed using Equations 2.54 and 2.55:

$$PWV = \sqrt{\frac{A}{\rho}\frac{dP}{dA}} = \sqrt{\frac{A}{\rho}\frac{dA}{dP}\frac{dP}{dA}} = \frac{1}{Z_C}\frac{dP}{dA} = \frac{dQ}{dP}\frac{dP}{dA} = \left.\frac{dQ}{dA}\right|_{\text{reflection-free}} \tag{2.58}$$

To implement the flow-area method, the flow-area loop is drawn through simultaneous measurements of the flow and area. The measurements require a sufficiently fine temporal resolution below 4 ms to produce multiple data points during the reflection-free period. Typically, this period lasts 50 ms at the common carotid artery [40, 62].

In this work, the flow-area method is used to determine the local PWV for several reasons. First, this method is expressly designed to measure the local PWV. Second, the flow waveform along with the resulting ABP waveform, can provide a complete view of the dynamic nature of the arterial system. In the following subsections, ultrasound imaging techniques to obtain the volumetric flow rate and cross-sectional area are discussed.

2.3.2 Blood Flow Measurement

If a complete velocity profile inside the lumen were available with a sufficient temporal resolution, the flow rate can be calculated by integrating the velocities over the cross-section. However, this approach requires a complex system to control beam directions with intensive computation power. Instead, the flow rate can also be calculated if a spatial mean flow velocity, an average flow velocity over the vessel cross-

section, is measured directly. This approach potentially aides the goal of designing a portable and low-cost system.

As discussed in Subsection 2.1.5, the Doppler ultrasound is utilized to measure flow velocity. Specifically, the spectral Doppler is used in this work to acquire the depth-specific Doppler signals. The Doppler effect originally refers to the frequency shift of the reflected wave from a moving object, where the frequency shift is a function of the velocity of the object. This principle is not directly applicable to the pulsed Doppler because of the difficulty of detecting the shift. The frequency-dependent attenuation affects the wide band of the echo spectrum, obscuring the underlying Doppler shift [41]. Instead, a short acoustic pulse is transmitted multiple times to gauge the change of the round-trip time to an object, which is represented as the frequency of the down-sampled Doppler signal.

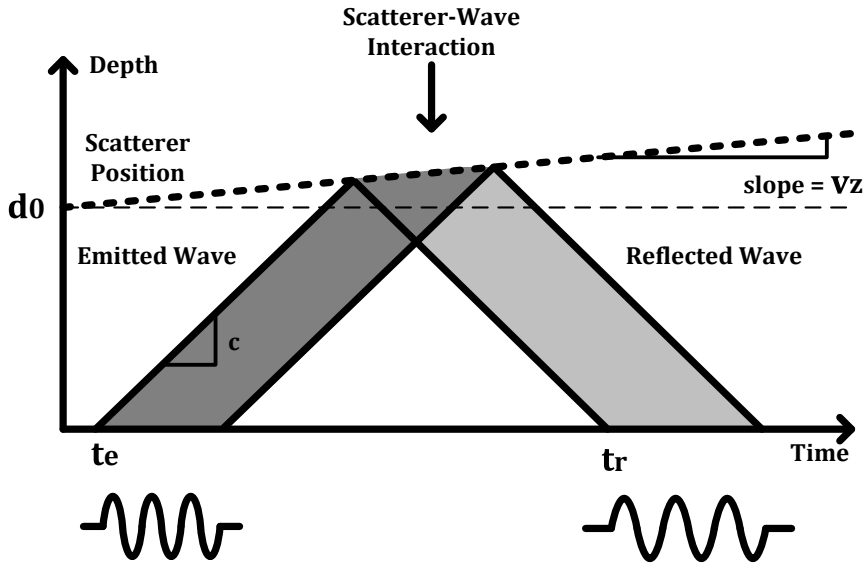

Figure 2-21: Diagram of pulsed Doppler time compression [42, 46].

To further detail the theory of operation, let's assume that the object moves relative to the transducer with an axial velocity of v_z, illustrated in Figure 2-21. A pulse received time (t_r) experiences either expansion or compression from a pulse

emitted time (t_e) as [42]:

$$t_e = (\frac{c - v_z}{c + v_z} t_r - \frac{2d_0}{c + v_z}) \approx (1 - \frac{2v_z}{c})(t_r - \frac{2d_0}{c}(1 + \frac{v_z}{c})) \quad (\because \frac{v_z}{c} \ll 1) \tag{2.59}$$

where c is the speed of sound and d_0 is the distance at $t = 0$. The emitted pulse ($e(t)$) is described by a rectangular windowed sinusoid as:

$$e_{mult}(t) = \sum_{n=-\infty}^{\infty} \prod ((t - nT_{PRF}) \frac{f_0}{M}) \sin(2\pi f_0 (t - nT_{PRF})) \tag{2.60}$$

where M is the number of pulse cycles, PRF is a pulse repetition frequency, T_{PRF} a pulse repetition period, and f_0 is a center frequency of the transmitted acoustic wave. Then, the received echo is expressed as:

$$r_{mult}(t) = \sum_{n=-\infty}^{\infty} \prod (((1 - \frac{2v_z}{c})(t - \frac{2d_0}{c}(1 + \frac{v_z}{c})) - nT_{PRF}) \frac{f_0}{M}) \sin(2\pi f_0 ((1 - \frac{2v_z}{c})(t - \frac{2d_0}{c}(1 + \frac{v_z}{c}) - nT_{PRF})) \tag{2.61}$$

By taking an initial sample at $t = \frac{2(d_0 + \Delta d)}{c}$ and re-sampling at the rate of PRF, the downsampled sequence ($x[n]$) has a form of:

$$x[n] = \prod ((\frac{2\Delta d}{c} - \frac{2v_z}{c} n T_{PRF}) \frac{f_0}{M}) \sin(2\pi f_0 (\frac{2\Delta d}{c} - \frac{2v_z T_{PRF}}{c} n)) \tag{2.62}$$

Equation 2.62 suggests the center frequency of the sampled signal is a linear function of the axial velocity. In addition, as the object passes through the sample volume, the amplitude of the downsampled signal is modulated, which is a source of inherent spectral broadening [63]. From Equation 2.62, the Doppler frequency (f_D) is measured as [42]:

$$f_D = \frac{2 f_0 v_z}{c} \tag{2.63}$$

Since the Doppler ultrasound measures the axial velocity, the angle of insonation or

the Doppler angle (θ) should be considered to calculate the true velocity as:

$$v_{scat} = \frac{cf_D}{2f_0 \cos(\theta)} \tag{2.64}$$

Due to its sampling nature, the pulsed spectral Doppler can suffer from aliasing if the speed of the object exceeds

$$v_{scat,max} = \frac{cPRF}{4f_0 \cos(\theta)} \tag{2.65}$$

While the aforementioned pulsed Doppler is discussed from a single moving object, the Doppler signal obtained from blood flow is backscattered from numerous erythrocytes moving at a variety of velocities. In this case, the Doppler signal contains multiple frequency contents. Moreover, the Doppler spectral density is determined by the number of scatterers and the amount of acoustic energy insonating the scatterers moving at their respective velocities. In other words, the Doppler spectrum is determined by the velocity profile and acoustic beam patterns. For example, if the sample volume is preferentially defined at high flow lines, the Doppler signal has a stronger high-frequency content.

In order to easily calculate the spatial mean velocity, a uniform insonation technique is used in this work [64]. The uniform insonation means that the pressure field intensity is uniform across the sample volume, which is defined as completely covering the vessel cross-section. In this condition, the Doppler signal is equally weighted over the cross-section such that the spatial mean velocity is calculated by taking a mean frequency shift of the Doppler signal, assuming the cell density inside the vessel is uniform.

The uniform insonation can be achieved by using two different beam patterns. It can be achieved in the deep far-field as the beam width linearly increases with the depth. The other strategy uses a near-field pattern generated by a high aspect ratio rectangular aperture, and it is discussed more in depth in Chapter 5.

Compared to scanning a focused beam to measure and integrate the velocity profile over the cross-section, the uniform insonation approach does not necessarily

need an array system due to lack of beam scanning. However, the Doppler signal presents a stochastic nature due to the interference between individual acoustic waves backscattered from the numerous scatterers. Depending on the relative positions of these scatterers and the aperture, the interferences occur either constructively or destructively, creating variations in the acquired Doppler intensity at each frequency around the underlying true spectral density, representing a real velocity profile. As a result, the estimated spatial mean velocity is accurate on average, but it shows the variations of individual velocity measurements.

2.3.3 Cross-Sectional Area Measurement

The B-mode ultrasound image visualizes the cross-section of the target vessel. For this approach, a high frame rate is usually required with the system having an array as well as using high computation power, However, this system is unsuitable for low-cost and portability.

In fact, the cross-section is almost a perfect circle due to the high transmural pressure, unlike that of the vein. Given the axi-symmetric geometry, the cross-sectional area can be calculated from the inner diameter. The M-mode ultrasound is suited to image the pulsating arterial walls because it can easily achieve a fine temporal resolution when measuring the diameter.

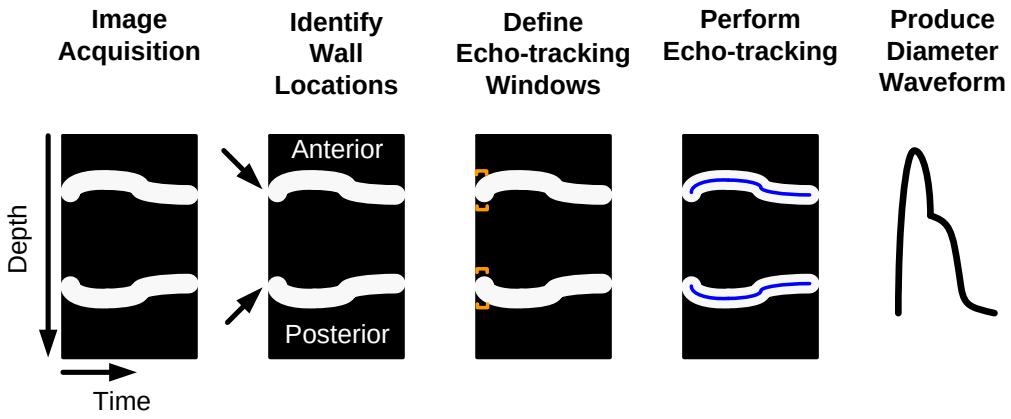

Figure 2-22: Illustration of a signal processing sequence for a distension waveform measurement.

The diameter waveform is measured in two steps: identifying of the anterior and posterior walls and tracking the echoes from the walls. Figure 2-22 shows the sequence of the diameter waveform measurement steps. Because specular scattering occurs, these echoes are strong in the acquired M-mode images. The absolute inner diameter is calculated from the distance between the two echoes.

While this measurement is typically done by sonographers on a frozen image, automated algorithms may be used, including a sustain attack filter approach [65]. The sustain attack filter utilizes dynamic thresholding to determine the inner boundary of the lumen and eventually the diameter. The dynamic thresholds are dependent on the strength of the prominent echoes. In addition to this approach, the peaks of each echo from the walls may be identified to calculate the inner diameter.

However, these methods are limited to achieve a fine spatial resolution to produce a full distension waveform as they solely rely on amplitude information, which is easily corrupted. A prior work showed that distension waveform estimation using M-mode showed poor performance [66]. Instead, echo-tracking techniques exploit both the phase and magnitude information to estimate the displacement of the echo of interest. After the vessel walls are located, the echo-tracking windows are applied to continuously track the movement of the echoes. This method demonstrated superior performance in estimation of the distension waveform, achieving a fine spatial resolution [66]. Then, change of diameter waveform is added to the initial inner diameter to produce a full diameter waveform.

To produce a diameter change waveform, cross-correlation based echo-trackers were introduced such as the cross-correlation model (CCM) estimator [67] and the complex cross-correlation model (C3M) estimator [68], assuming specific spectral characteristics of the received echo. These estimators evaluate and identify the peak in the cross-correlation function between the segments in the two RF data from consecutive pulses. The sampling frequency of the RF signal determines the resolution of the lags in the cross-correlation function. In fact, the cross-correlation function can be interpolated around the possible peak position to achieve a finer spatial resolution below the distance between adjacent samples. Given that the echo of interest resem-

bles the windowed sinusoid, parabolic interpolation may be considered [42] since the first-order Taylor series expansion of the cosine function is a parabola. In addition, an assumption on spectral characteristics allows better interpolation to locate the peak in the cross-correlation function. Such an assumption includes the bandwidth [69] and shape of power spectral density [67, 68]. Among these, the C3M estimator uses the complex RF signal that is acquired through the Hilbert transform or quadrature sampling. It is shown that the C3M estimator produces unbiased and low standard deviation estimates, thereby outperforming the CCM and other cross-correlation based estimators [68].

The C3M estimator evaluates two complex cross-correlation values to estimate the displacement of the echo. The velocity estimate of the target reflector in the C3M estimator can be expressed as [68]:

$$v = \frac{c}{2}\frac{PRF}{f_s}\frac{\angle(R[0,1])}{\angle(R[1,0])} \tag{2.66}$$

where c is the speed of sound, f_s is the sampling frequency of the RF signal, and R is the cross-correlation function. $R[i,j]$ represents the cross-correlation between the i-th lag in the depth and the j-th lag in the time domain. By dividing both the numerator and denominator with 2π, $f_s\frac{\angle(R[1,0])}{2\pi}$ can be seen as an estimate of the center frequency of the received echo. Then, $\frac{c}{2}\frac{\angle(R[0,1])}{2\pi}/f_s\frac{\angle(R[1,0])}{2\pi}$ is the estimate of displacement of the echo of interest. The velocity is then calculated by multiplying by the PRF, as shown in Equation 2.66.

The C3M estimator needs two complex cross-correlation values to calculate the velocity of the vessel wall. While the evaluation of the complete cross-correlation function requires intensive computation, a model-based estimator such as CCM or C3M is computationally efficient, suitable for real-time monitoring of the distension waveform from the raw ultrasound images.

Chapter 3

Prototype System Design

This chapter describes the design of a prototype ultrasound scanner system. First, the physical design of an ultrasound probe is addressed. Then, the overall architecture of the system is described, followed by the implementation details using off-the-shelf components. The following sections present electrical and acoustic characterizations of the system and operation for real-time ultrasound scanning.

3.1 Probe Design

In this work, the system operates to conduct M-mode imaging and spectral Doppler ultrasound simultaneously to measure a diameter and a spatial mean flow velocity waveform, respectively. To clearly visualize a cross section of a target vessel, the M-mode should be performed while an acoustic beam perpendicularly insonates vessel walls to maximize reflected echo strengths. For the Doppler ultrasound, however, an acoustic beam should ideally be in parallel to flow or at least at an angle because the Doppler ultrasound detects an apparent flow velocity along the beam axis. A commercial scanner uses an array in a single aperture when both imaging tissues and measuring blood flow simultaneously in a color flow mode thanks to beam steering capability. Instead, this work aims to design a low-cost device, thus proposing two separate apertures primarily assigned to each imaging mode to negate the need of beam steering capability.

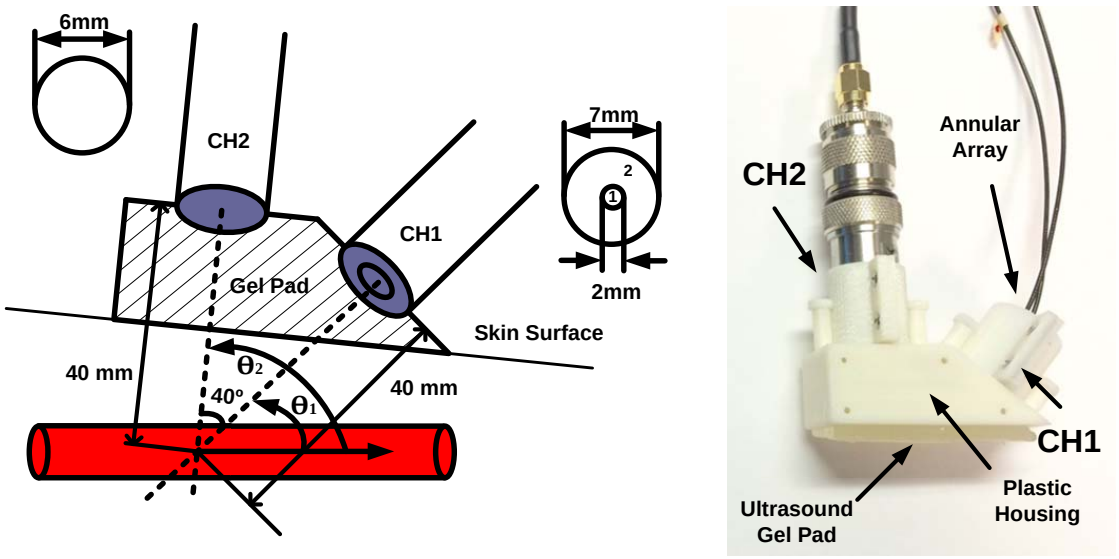

Figure 3-1: First probe design with circular apertures for the proof-of-concept human subject study [40].

Figure 3-1 shows the first design of the probe which was used for the proof-of-concept study described in Chapter 4. The circular aperture for channel 1 (CH1) emits ultrasound nominally at 50° for the Doppler ultrasound, while the beam from channel 2 (CH2) perpendicularly insonates the vessel for the M-mode.

In this design, a high-contrast M-mode image showing clear pulsation of the arterial vessel walls is obtained by scanning with a focused beam. On the other hand, a wide beam with a sufficient beam width is required to achieve the uniform insonation for the Doppler ultrasound. The 3 dB full beam width of 10 mm is preferred to limit the velocity overestimation under 5% if the carotid artery is imaged [46]. For the vector Doppler technique to estimate the angle of insonation, as detailed in Section 4.2, the focused beams are preferred to obtain the Doppler signals preferentially from the high-flow line. For the Doppler ultrasound in CH1, a two concentric elements probe is proposed. The inner element with a small circular aperture produces the wide beam, while the outer ring element produces the focused beam for the vector Doppler. A circular transducer in CH2 generates the focused beam for the M-mode and vector Doppler.

In detail, to generate the desired lateral beam patterns at the depth of 40 mm,

the center frequencies of the transmit pulse and aperture dimensions are determined. For the Doppler ultrasound, the center frequency of 2.5 MHz is chosen, and the inner diameter of the array is determined to be 2 mm, which gives a beam width of 12.6 mm. The diameter of the single element transducer is 6 mm. 5 MHz is chosen for the center frequency of the M-mode imaging pulse for the optimum trade-off of acoustic output and an axial resolution. As a result, the circular transducer with a center frequency of 3.3 MHz and a relative bandwidth of 100% is selected such that sufficient acoustic outputs can be generated at 2.5 MHz for the vector Doppler and 5 MHz for the M-mode. Finally, the outer diameter of an array is determined to be 7 mm to generate a beam width similar to the beam width produced by the single-circular transducer as shown in Figure 3-1.

Figure 3-1 also depicts the physical dimensions of the transducer assembly relative to the target vessel. The designed distance from each transducer to the cross-beam point is 40 mm corresponding to the skin depth of 21.7 mm. With these specifications, the two concentric elements probe (TransducerWorks, Central Hall, PA, USA) was

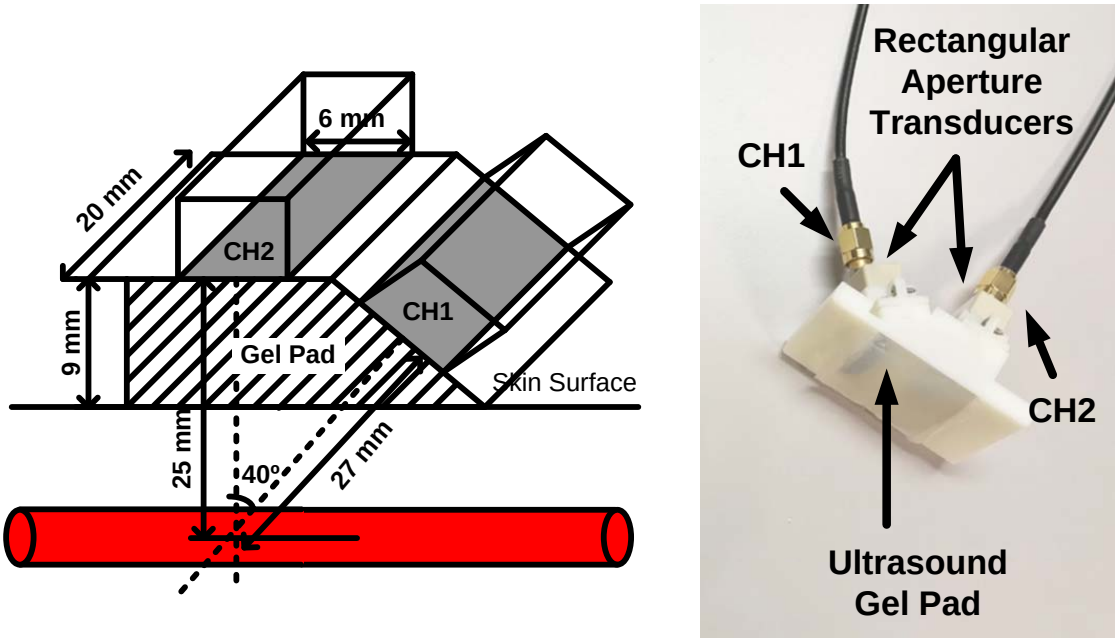

Figure 3-2: Second probe design for widebeam insonation with rectangular apertures for motion-tolerant ultrasound measurements used in the Valsalva maneuver study [70] and NEWEST study.

custom-designed and manufactured while the single-element transducer (C384-SU, Olympus NDT, Olympus, Waltham, MA, USA) was purchased off the shelf.

The second probe design, shown in Figure 3-2, incorporates two wide rectangular aperture ultrasound transducers in order to generate a laterally wide pressure field pattern. Similar to the first design, the transducer in CH1 is used for the Doppler ultrasound, while the other transducer in CH2 is also used the vector Doppler technique in addition to the M-mode. The two beam axes intersect at the cross-beam point at the distance of 25 mm from the transducer and the skin depth of 17 mm.

To generate a wide lateral pressure field pattern, the dimension of the rectangular aperture is determined to be 20 mm×6 mm, which is detailed in Section 5.1. The center frequency for the Doppler is 2 MHz, while that of the imaging pulse is either 3.5 MHz or 5 MHz. The wide rectangular ultrasound transducer (Imasonic, Voray-sur-l'Ognon, France) was custom-designed and manufactured. The second probe design was used in the device for the Valsalva maneuver study in Chapter 6 and NEWEST study in Chapter 7.

Plastic parts hold each transducer in pre-defined geometries as shown in Figures 3-1 and 3-2. These plastic parts were fabricated using 3D printers. In order to eliminate air gap between the transducers and the skin surface, a solid ultrasound gel pad was used in addition to a commercial ultrasound gel. For the proof-of-concept study, a commercial gel pad was sliced and fit into the plastic parts. In fact, the commercial gel pad is produced in certain dimensions. Due to its softness, slicing the gel pad in arbitrary dimensions is challenging. Instead, for the subsequent studies a hydrogel pad is custom-manufactured.

Agar-based hydrogel was investigated for tissue phantom [71, 72]. It is suggested that manufacturing agar gel is most straighforward and fast [72]. Mostly, agar solution with a mass concentration between 1-3% was suggested. The gel production process is briefly described following:

1. Prepare a water solution with approximately 2% agar powder.

2. Use a hot plate to heat up the solution beyond 100 °C, while occasionally stirring

to prevent clumping.

3. Once the solution becomes transparent, cool down the hot plate to about 50 °C, and let the solution cool down as well, while occasionally stirring up to prevent clumping.

4. Once the solution becomes slightly viscous, use a plastic Pasteur pipette to gradually fill up the mold. Put a small amount of solution into the mold and let it cool down to make sure any opening in the mold is covered.

5. Gradually fill the entire mold without big protuberance, and let it completely cool down.

The manufactured gel pads are stored in an air-tight zip-bag to prevent it from drying.

3.2 System Architecture

Ultrasound scanning consists of the transmit of an acoustic pulse and the receive of echoes. For pulsed ultrasound, the same aperture is used for both the transmit and receive in a time-interleaved manner. The received echoes are digitized and conditioned for subsequent post-processing and data analysis. Since several combinations of the pulse-echo operation are utilized in this work, the system should have programming flexibility. While time gain compensation (TGC) to equalize the attenuation in tissues is a common feature of commercial scanners, it is not considered here, as a target vessel is usually located at a specific depth.

The proposed architecture consists of mainly five blocks: an ultrasound transceiver (TRX), a field programmable gate array (FPGA), a microcontroller (MCU), a power management (PM) block, and peripheral circuitries. Figure 3-3 presents the block diagram.

The pulsed acoustic wave is transmitted by exciting the transducers with a high voltage bipolar square pulse generated by the pulsers in the TRX. This voltage pulse

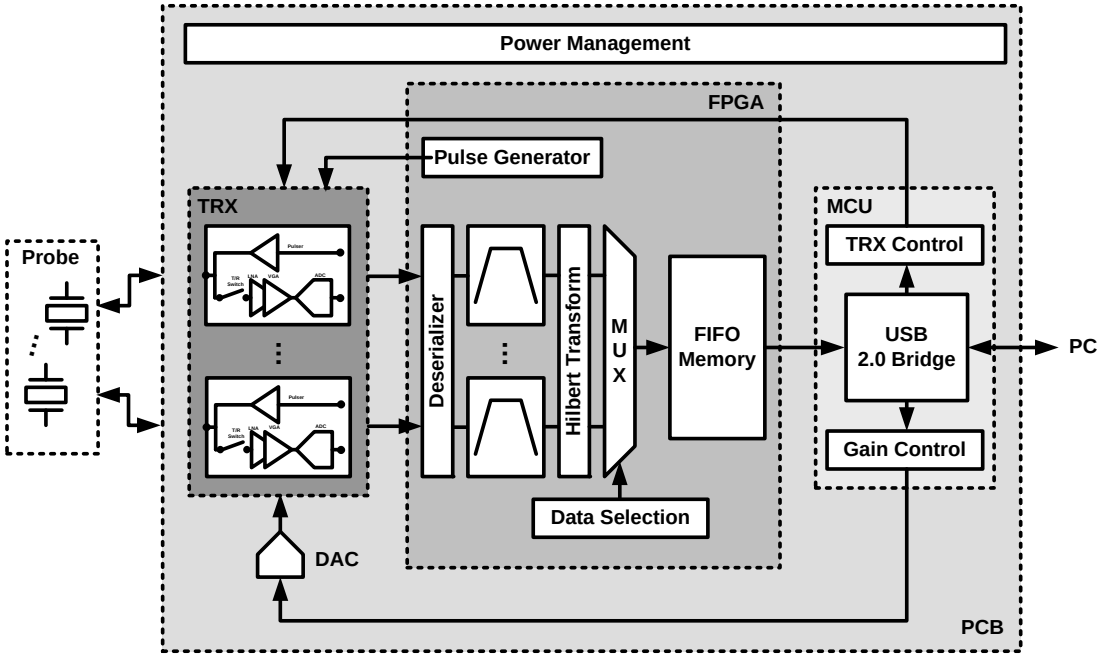

Figure 3-3: Block diagram of the custom-designed ultrasound system.

is generated from high voltage rails, which range between ±20 to ±30V, and control logic signals for the pulsers are fed by the FPGA. Since the transmit and receive signal paths to the transducer are shared, transmit/receive (T/R) switch protects the low-voltage-receive circuits during the transmit. Then, the T/R switch is closed to hear the echoes during the receive. The receive circuitry includes low noise amplifiers (LNAs), variable gain amplifiers (VGAs), anti-aliasing filters, high-pass filters, and analog-to-digital converters (ADCs). The digitized signals are then transferred to the FPGA in a serial fashion through a low voltage differential signal (LVDS) standard.

The FPGA controls digital signal processing. The serial bit streams are deserialized and filtered by bandpass filters whose respective center frequencies and bandwidths are determined by the spectral characteristics of the transmitted pulse. The bandpass filtering rejects out-of-band noise and interferences. The subsequent Hilbert transform filters produce complex signals with in-phase and quadrature parts. Following this, the data multiplexer selects which data samples to save into the First In First Out (FIFO) memory. The FIFO memory is constantly queried by the MCU for transferring available data. The FPGA also generates the logic signals to control the

pulsers and T/R switches operation.

The MCU establishes a primary communication link to the PC. A high-speed USB 2.0 interface achieves a data rate higher than 10 Mbps, which is the required data rate for this work. In addition, the MCU relays commands from the PC to either digital-to-analog converters (DACs) for controlling the gain of the VGAs or configuration bits in the FPGA and TRX. The communications between the off-the-shelf chips, except the serial bit streams from the TRX to FPGA, are all through a serial peripheral interface (SPI).

The PM blocks are divided into a high-voltage and a low-voltage generation block. To generate the bipolar high-voltage rails, switching regulators are used to up-convert the input DC voltage. The up-converted rails are linearly regulated. Otherwise, the transmitted pulse amplitude can be modulated by power line noises. For the Doppler ultrasound, due to the low echogenicity of erythrocytes, it is important to preserve the integrity of the Doppler signal path. For the low voltages, a switching regulator is used to down-convert the input DC voltage to an intermediate level in order to reduce power loss originated from high dropout for some lower voltage generation. Individual low-voltage rails are generated through linear regulators from either the original input or the intermediate voltage.

The peripheral circuit includes crystal oscillators for clock generation for the TRX and FPGA and the DAC.

3.3 System Implementation

The system is implemented on a printed circuit board using off-the-shelf components, as shown in Figure 3-4. The physical dimension of the board is 14.7 cm by 13.2 cm. The board consists of six metal layers including the top and bottom. Ground planes and linear regulators for an analog and a digital power domain are separated to produce clean analog supply voltages. The system is also equipped with other communication links and data storage, such as an SD card and a USB/UART interface directly from the FPGA. In addition, several test points and jumpers are in-

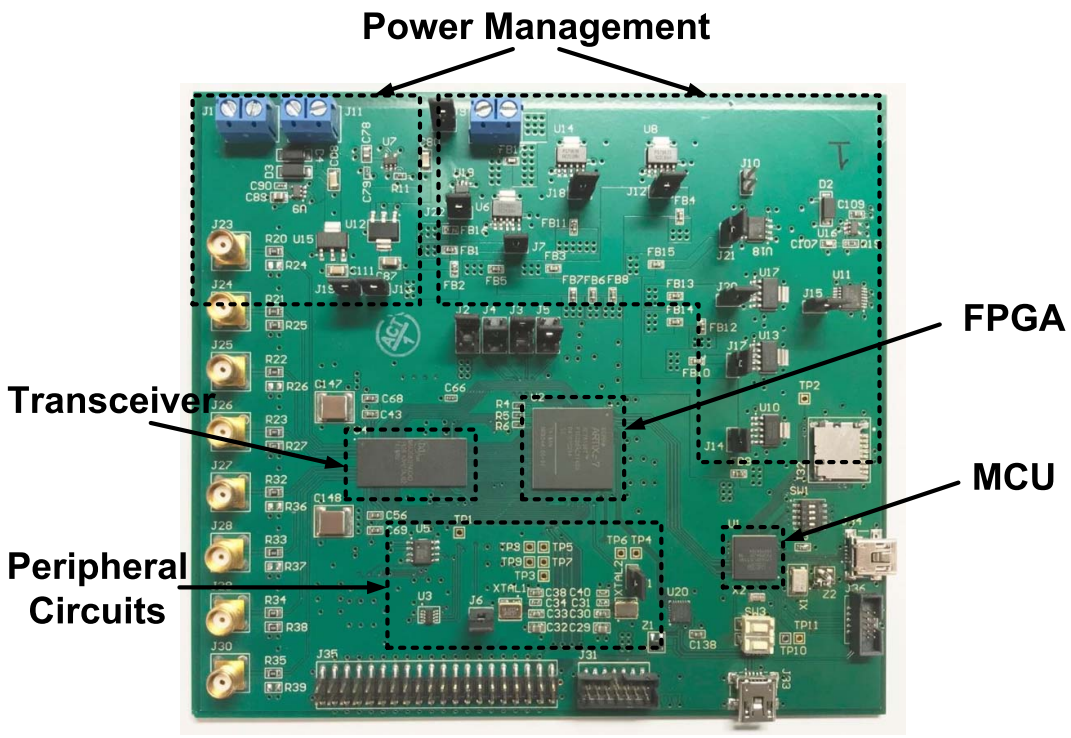

Figure 3-4: Designed portable ultrasound scanner system on a printed circuit board.

cluded for debugging purposes. Selection of the individual components of this design is presented in Figure 3-5.

The required voltages for the low-voltage circuits are ±5V, 3.3V, 2.5V, 1.8V, and 1.0V. The input DC voltage is chosen as 5.5V, leaving a room for the linear regulators' dropout. 5V and 3.3V are directly generated from 5.5V. The intermediate voltage is chosen as 3V to leave the room for 2.5V. The lower voltages are primarily generated from 3V, but they can be directly produced from 5.5V, if needed. -5V is generated via a linear regulator from -7V, which is converted from the input using an inverting switching regulator.

The high-voltage rails can be self-generated or provided from external power supplies. Since the highest voltages that the selected linear regulators of this design can handle are ±32V, higher voltages should be provided externally, if necessary. The output voltages of the switching and linear regulators in the high-voltage generation are tunable through potentiometers.

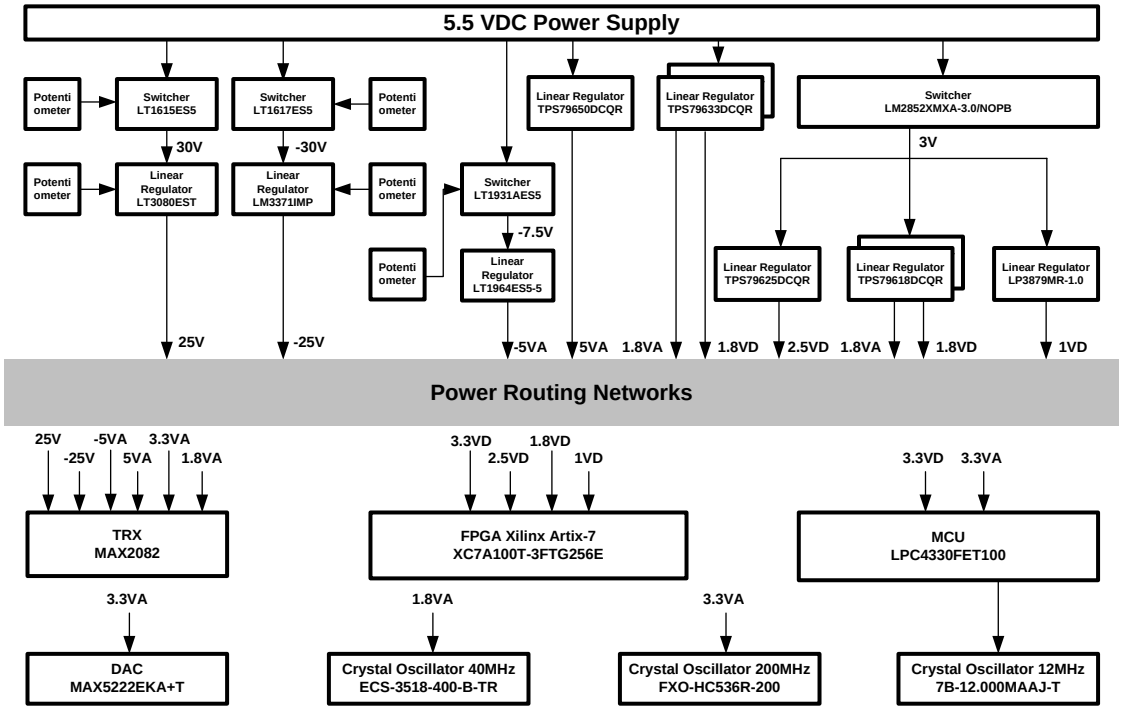

Figure 3-5: Implementation of the designed system with off-the-shelf chips.

In this design, the MAX2082 octal transceiver is used, which is equipped with eight channels of electronics. This transceiver packages the pulsers, T/R switches, and receive circuits, including amplifiers and 12-bit ADCs, altogether. The sampling frequency of the ADC is 40 MHz in order to faithfully capture spectral contents of the received echo. Finely sampled radio frequency (RF) signals are more useful to estimate a sub-wavelength echo displacement when the echo-tracking techniques are applied. Typically, signal-to-noise ratio (SNR) for the spectral Doppler is low, and the Doppler signal presents strong clutter. Given that an expected relative amplitude of the clutter to signal is between 30 and 50 dB, which is highly dependent on measurement situations, a dynamic range of 60 dB is required to achieve 10 dB SNR after the clutter rejection. The reported SNR of the selected transceiver ranges from 58 to 67 dB.

For the FPGA, Artix-7 from Xilinx is chosen based on the trade-offs between complexity, power, and speed. This FPGA supports the convenient implementation of digital finite impulse response (FIR) filters through Vivado Design Suites from Xilinx.

The 192-taps bandpass filter and 64-taps Hilbert transform filter are synthesized.

The digital system functions in two clock domains: a main clock and a sub clock. The two clock signals are generated from clock management blocks, which receive source clocks from external crystal oscillators. The main clock is fed from a frame clock of the LVDS signals. This clock controls the receive path, FIFO memory writing, and pulse generation to perfectly synchronize the transmit and receive operation. The FIFO memory reading and the SPI is controlled by the other clock domain, where the FIFO memory bridges the two clock domains.

Due to the limited data rate, selected data samples are transferred to the PC. A strobe signal, generated at the beginning of the pulse transmit, is used as a trigger to run internal counters to measure the depth of each RF data sample. Then, the samples at specific depths or within a certain range of depth are selected for writing in the FIFO memory.

In the SPI communication between the MCU and FPGA, the MCU acts as a master device. It continuously queries the FPGA to retrieve the saved data in the FIFO memory. If valid data are retrieved, it relays a packet of data to the PC over the USB interface. Otherwise, a pre-defined code is received by the MCU and discarded internally.

3.4 System Characterization

3.4.1 Acoustic Characterization

This subsection describes acoustic characterization of the designed system with various ultrasound transducers using a hydrophone (ONDA HNC-0400, Sunnyvale, CA, USA) whose position was controlled by a 3D-translational stage. Three different ultrasound transducers were used: a two concentric elements probe with a nominal inner and outer diameter of 2 mm and 7 mm, respectively (manufactured by TransducerWorks), a circular aperture transducer with a diameter of 6 mm (C384-SU, purchased from Olympus NDT), and a rectangular aperture transducer with a size of

20 mm by 6 mm (manufactured by Imasonic). In order to conduct ultrasonography as designed, sufficient acoustic outputs should be observed at prospective center frequencies for the acoustic pulses, and desired acoustic pressure field patterns should be generated as designed and predicted by the FIELD II simulation.

Figure 3-6 shows the measured magnitude responses of the transducers. The center frequencies of the response for both elements in the concentric elements probe are around 2.5 MHz, where the center frequency of C384-SU is 3 MHz. The center frequency of the rectangular transducer is approximately 3.5 MHz. The relative bandwidths of these transducers are 100% or higher.

Figure 3-7 shows the measured pressure field patterns compared to the simulated patterns from the FIELD II simulation. The lateral patterns were measured at the depth of 25 mm from the transducers. Figures 3-7(a) and (b) show a deep far-field pattern, as expected, at 25 mm because of the small aperture size. On the other hand, Figures 3-7(c) and (d) present a relatively focused beam because this depth is close to the natural focus. Figures 3-7(e) and (f) show near-field patterns with uniform intensities in a lateral dimension. These results suggest that the ultrasound transducers connected to the designed system generate the pressure fields close to what were desired and predicted. Small deviations from the prediction exist due to slight mis-orientation of the transducer relative to the axes in a 3D-translational stage

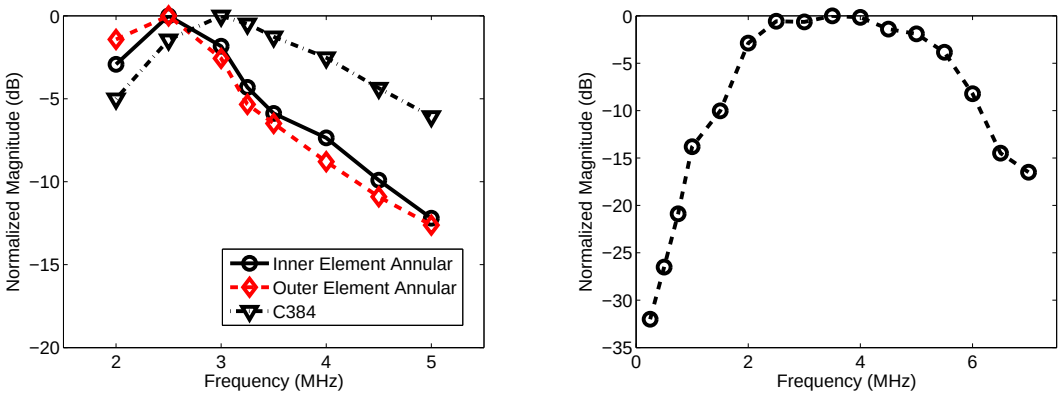

(a) Circular transducers

(b) Rectangular transducer

Figure 3-6: Measured magnitude responses of the ultrasound transducers.

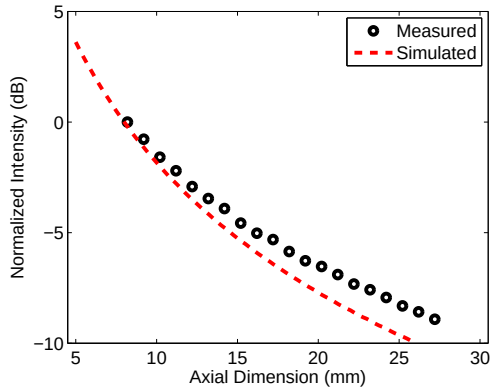

(a) Annular inner element, 2.5 MHz

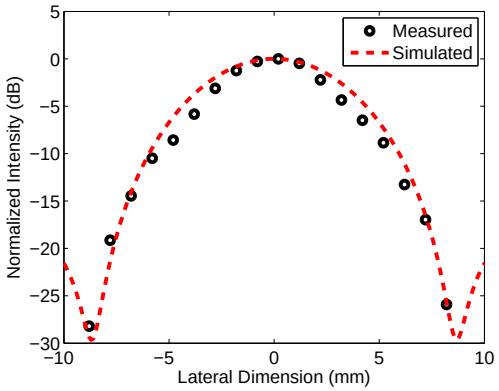

(b) Annular inner element, 2.5 MHz

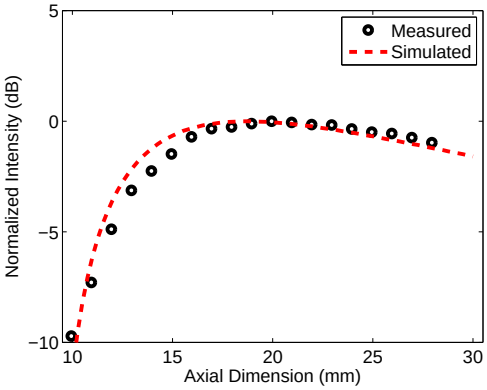

(c) Annular outer element, 2.5 MHz

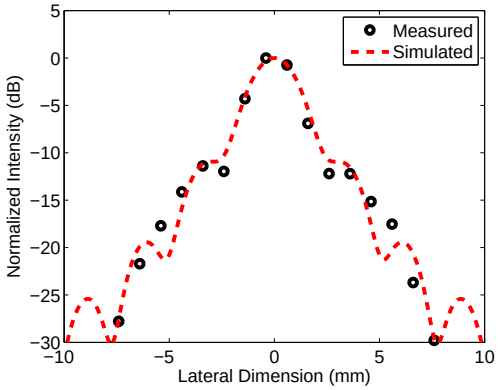

(d) Annular outer element, 2.5 MHz

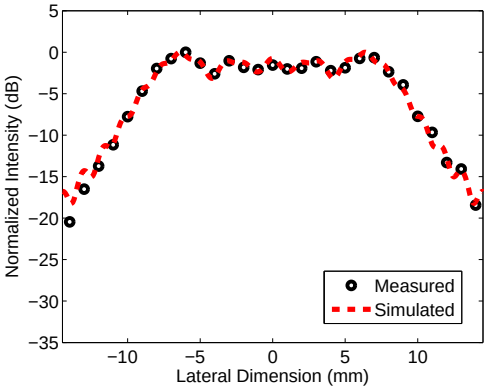

(e) Rectangular 2 MHz

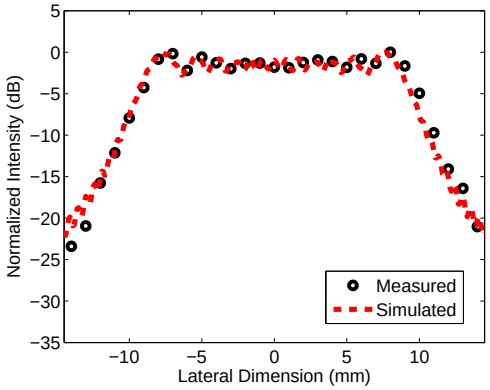

(f) Rectangular 5 MHz

Figure 3-7: Pressure field patterns in a lateral and an axial dimension with different apertures and center frequencies. The lateral patterns were measured at the depth of 25 mm. The simulated diameters for the two concentric elements probe are 2.3 mm (inner) and 6.8 mm (outer).

and the finite resolution of a hydrophone tip.

3.4.2 Electrical Characterization

Electrical characterization of the designed system consists of verification of integrity of the signal path, gain controls, and measurement of the high-voltage pulses. The signal integrity was tested by applying a clean sine wave into the input to the signal chain while the system was operated in the receive mode. Figure 3-8 shows the spectra of ADC outputs in various input conditions. The gain of the analog front end (AFE) is nominally set to 45 dB. Even when the input is grounded, the largest spur is at -70 dB, originated from a spur at 1.6 MHz due to the switching regulator that generates 3V from 5.5V. More specifically, the spur at 1.6 MHz in the 5.5V input power supply voltage is propagated to 5V and -5V, which supply the current on the T/R switch with a bridge diode topology. Due to its poor power supply rejection, the spur appears at the input of the LNA. When the connector to the probe is left open, many interference signals are injected to the input of the LNA. Figure 3-8 shows the spectra of the ADC output when a 2.5 MHz or a 5 MHz tone are injected. In these spectra, harmonics in addition to the interference are visible.

Figure 3-9 shows the spectra after the digital bandpass filtering. Although interference appears at the input of the LNA, it is outside the signal band. Through the bandpass filtering, the interference is suppressed below the noise floor, thereby improving the SNR. This filtering also transforms the width of data from 12 bits to 16 bits.

The Hilbert transform filter produces the analytic signal as shown in Figure 3-10. As a consequence, the negative frequency is suppressed by 60 dB. For the Doppler ultrasound, the Hilbert transform is needed to preserve directional information of the flow after down-sampling the raw RF data. On the other hand, for the M-mode, the Hilbert transform can be implemented at the PC because no down-sampling is performed. With this figure, the signal integrity for the M-mode is validated.

Figure 3-11 shows the spectra of the down-sampled baseband Doppler signal. The simulated Doppler shift is 3 kHz. The typical Doppler spectrum in tissues presents

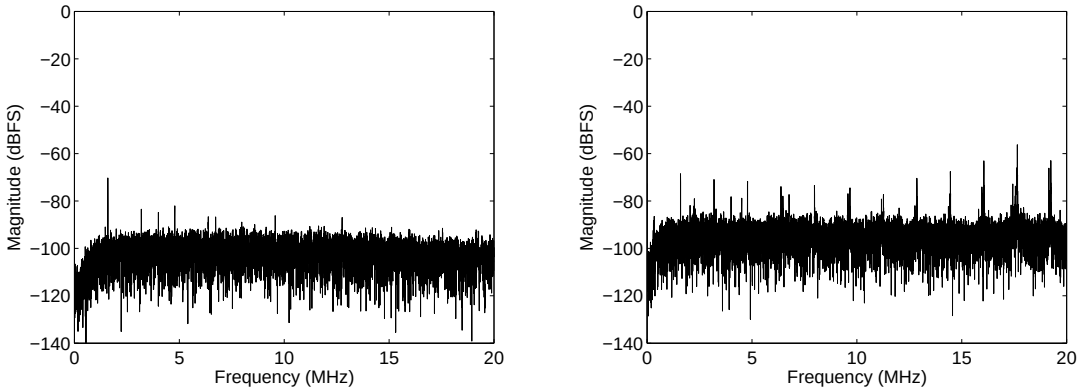

(a) Shorted to ground

(b) Floating

(c) 2.5 MHz sine wave

(d) 5 MHz sine wave

Figure 3-8: Spectra of the output of the ADC at various input conditions.

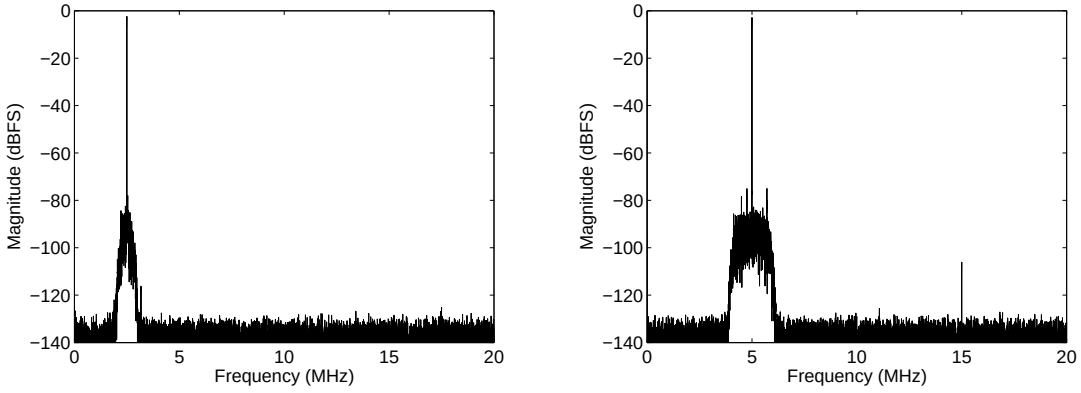

(a) 2.5 MHz sine wave

(b) 5 MHz sine wave

Figure 3-9: Spectra of the output of the digital bandpass filter at various input conditions.

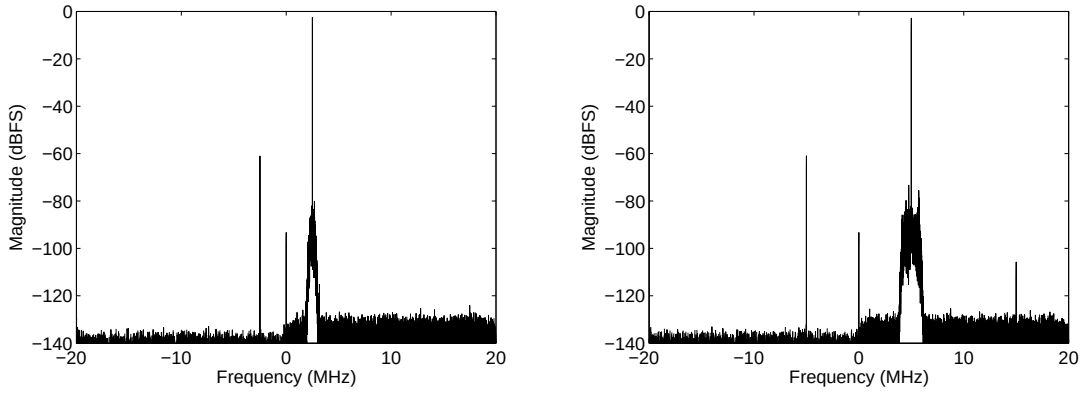

(a) 2.5 MHz sine wave

(b) 5 MHz sine wave

Figure 3-10: Spectra of the output of the digital Hilbert transform filter at various input conditions.

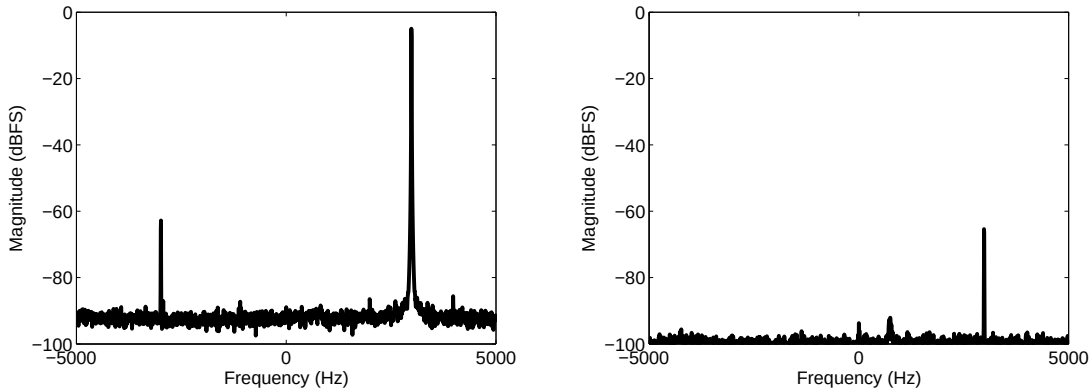

(a) A high amplitude

(b) A low amplitude

Figure 3-11: Spectra of the Doppler signals mimicking a 3 kHz frequency shift with different amplitudes.

strong clutter at DC while the blood flow signals appear with a finite bandwidth due to the velocity profile at much lower magnitudes. Since the Hilbert transform suppresses the negative frequency by 60 dB, Figure 3-11(a) presents a tone at -3 kHz, 60 dB lower than the original tone at 3 kHz. Figure 3-11(b) shows the Doppler spectrum with a lower amplitude. In this case, the tone at -3 kHz is buried under the noise floor. Overall, the signal integrity for the Doppler is also validated.

The gain of the AFE is controlled by a differential voltage that is externally set by the two DACs. Figure 3-12 shows the measured gains in comparison to the nominal

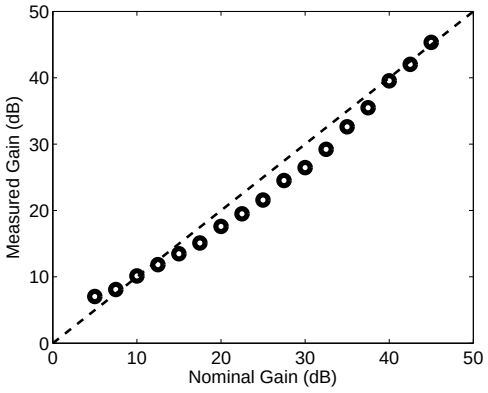

Figure 3-12: Measured gains of the analog front end.

gains. Although it is not perfectly linear, the measured gains monotonically increase with the nominal gain settings.

Next, the pulsers were tested. The pulser simply consists of a pull-up and a pull-down transistors. Figure 3-13 shows the produced bipolar voltage pulses with various load transducers. From the electrical circuit model in Subsection 2.1.3, the piezoelectric element consists of a series resonator in parallel with a capacitor. This capacitor is charged and discharged as the voltage across it alternates, which primarily determines the pulse waveform shape. In detail, for example, as the load is pulled-up, the voltage ramps up by charging the capacitor with the transistor operating like a current source in a saturation regime. As the transistor escapes the saturation, the voltage approaches the final value in an exponential manner with a varying time constant as the output resistance of the transistor varies. When this capacitor is large due to a large aperture, the slew rate is low, as shown by the comparison between Figure 3-13(a) and (e). Such a trend is also apparent between Figure 3-13(a) and Figure 3-13(b).

In addition, the impedance shows a peak at the anti-resonant frequency. While the pull up or down transistor works as a current source in the saturation, the resulting waveform shows inductive peaking at the anti-resonant frequency, which is higher than the center frequency of the pulse. This overshoot due to the peaking quickly fades away. Such a trend is shown in Figure 3-13. The high-voltage rails are $\pm$30V

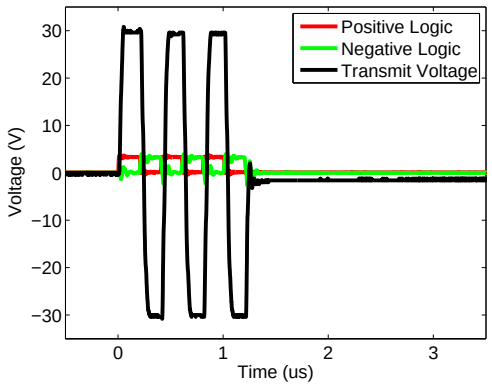

(a) Inner element of the concentric elements probe

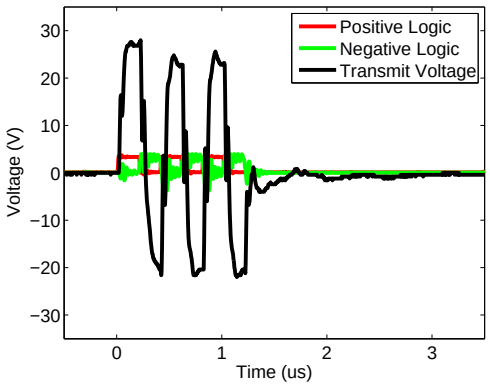

(b) Outer element of the concentric elements probe

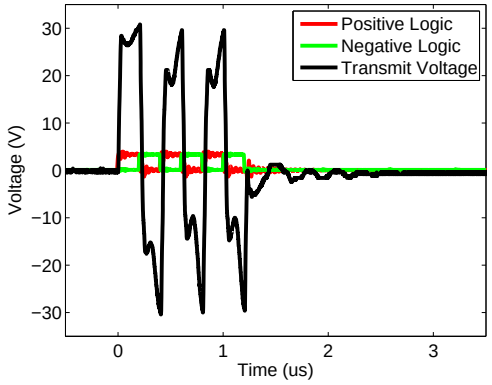

(c) Olympus C-384 2.5 MHz

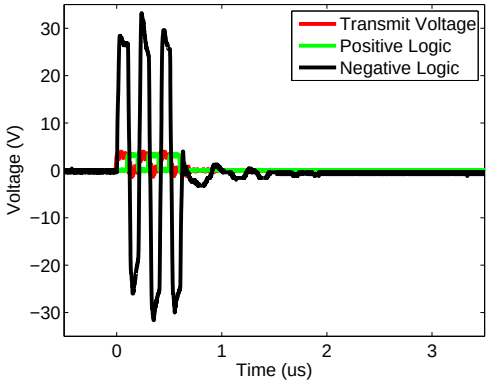

(d) Olympus C-384 5 MHz

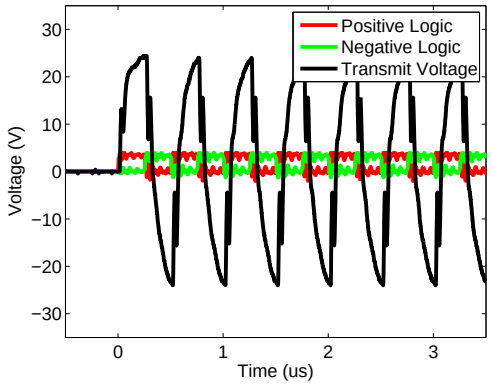

(e) Rectangular transducer, Doppler pulse

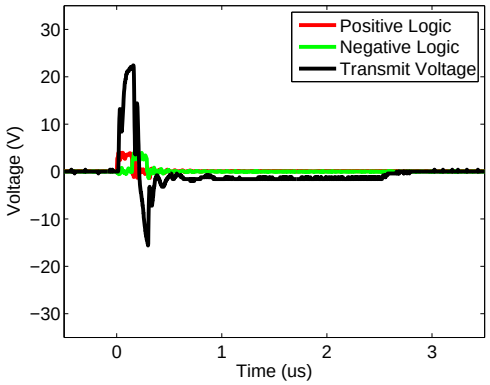

(f) Rectangular transducer, imaging pulse

Figure 3-13: Generated high-voltage square pulses for various ultrasound transducer loads. For (a) and (b), a two concentric elements probe was used, which was custom manufactured with a nominal inner and outer diameter of 2 mm and 7 mm, respectively. For (c) and (d), an off-the-shelf ultrasound transducer from Olympus NDT was used. For (e) and (f) a wide rectangular ultrasound transducer with a size of 20 mm by 6 mm from Imasonic was used.

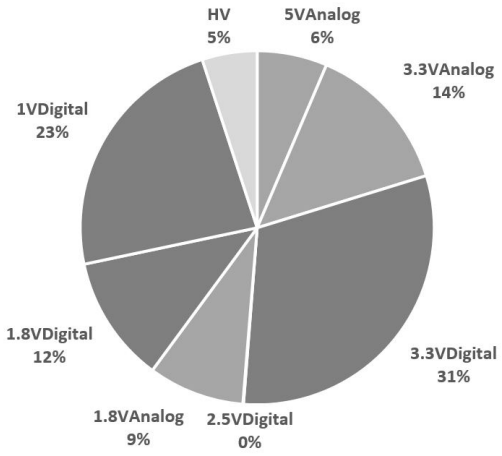

Figure 3-14: Power breakdown of various voltage levels.

for Figure 3-13(a) to (d) and ±25V for Figure 3-13(e) and (f).

Finally, Figure 3-14 shows power breakdown of the system. Typical power consumption of the system is reported between 5.5W and 6W. Since the FPGA and MCU used in this work are for generic purposes, their power consumption, such as 1V digital (FPGA internal core) and 3.3V digital (MCU), takes a large portion of the total power. Therefore, with the help of custom-designed digital integrated circuits, this power consumption can be greatly reduced.

3.5 System Operation

Figure 3-15 shows an example of a complete prototype device with the second probe design. For the proof-of-concept study in Chapter 4, the designed system is operated in two modes: a normal mode and an angle mode. During the normal mode, the Doppler ultrasound with the uniform insonation and the M-mode ultrasound are simultaneously performed. The inner element of the concentric probe is activated to transmit a three-cycle pulse for the Doppler with a pulse repetition frequency (PRF) of 10 kHz and a center frequency of 2.5 MHz, achieving a maximum detectable velocity of 2.36 m/s given the Doppler angle of 50°. The transducer for CH2 transmits a three-cycle pulse with a PRF of 250 Hz and a center frequency of 5 MHz. During the angle

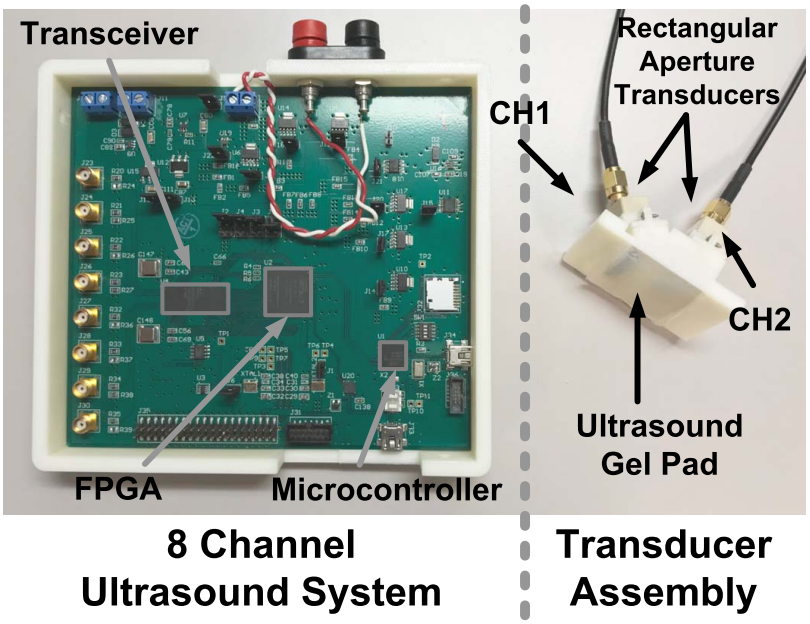

Figure 3-15: Prototype ultrasound scanner system used in the Valsalva maneuver study and NEWEST study with the second probe design [70].

mode, the vector Doppler technique is performed. In this mode, the outer element of the array is activated to transmit the Doppler pulse, while the transducer for CH2 transmits the same pulse at the same PRF.

For the Valsalva maneuver and the NEWEST study discussed in Chapters 6 and 7, the system is operated in a single mode while the vector Doppler is performed in background. For the Doppler ultrasound, a 26 or 32-cycle pulse with a PRF of 5 kHz and a center frequency of 2 MHz is used to excite the ultrasound transducer, achieving a maximally detectable velocity of 1.49 m/s given the Doppler angle of 50°. For the M-mode, a single cycle pulse with a PRF of 250 Hz and a center frequency of 3.5 or 5 MHz is used.

Several practical considerations are addressed to preserve the signal integrity. First, the pulses from each channel for the vector Doppler are transmitted in a time-interleaved manner. The pulsed Doppler ultrasound measures the flow velocity through a change of the round-trip time over multiple pulse transmissions, while the same aperture works for the transmit and receive. Unless the pulses are transmitted in an interleaved manner, one transducer acts as a transmit aperture while

the other may work as a receive aperture, picking up the false Doppler signal. For example, the transducer of CH2, although perpendicularly positioned to the vessel wall, may observe the signal with significant Doppler shifts. Therefore, the ultrasound pulses should be transmitted in a time-interleaved manner, assuming the flow velocity barely changes within the time-interleaving period.

In addition, the T/R switch operation is synchronized to the highest pulse repetition frequency to mitigate artifacts. The PRF of the M-mode (250 Hz) differs that of the Doppler (5 or 10 kHz). Due to the cross-talk in both the electrical or the physical domain, the Doppler signals can be compromised by having erratic samples at every 20 or 40 samples. This consideration is shown effective to eliminate the erratic samples. Otherwise, the Doppler spectrum would display tones at the multiples of 250 Hz.

Finally, the cross-talk in the physical domain can occur. Although the center frequencies for the imaging pulses (3.5 or 5 MHz) are usually outside the signal band for the Doppler, due to the wide band characteristics of the short imaging pulse, some acoustic energy at 2 or 2.5 MHz can be picked up by the Doppler channel at every 4 ms. Sufficient acoustic coupling not to limit the signal integrity should be maintained to reduce the reflection at the skin boundary to mitigate the cross-talk.

3.6 Graphic User Interface

A graphic user interface (GUI), as presented in Figure 3-16, is essential for the sonographer to correctly identify the target vessel and ensure the acquisition of high-quality images. The GUI, modified from a previous work [73], displays the real time Doppler spectrogram and M-mode images. In addition, several system parameters can be controlled from the GUI. For example, the depth of the Doppler pulse gate and the center depth of the M-mode image can be adjusted just like commercial ultrasound scanners. Several AFE settings, including the gain and filter settings, can also be adjusted to fully exploit the dynamic range without saturating the AFE. Additionally, several real-time data analyses are also feasible. For instance, the spatial

mean flow velocity can be calculated in real-time, if needed. Furthermore, the anterior and posterior walls can be tracked using the automated algorithm. Based on this tracking, a volumetric flow rate and cross-sectional area can be calculated in real-time to construct the flow-area plot and eventually to extract the local PWV. In addition, the vector Doppler technique is run in the background to estimate the angle of insonation. Combining all these physiological parameters, the pulsatile part of the ABP waveform can also be calculated in real time with pulse pressures without calibration.

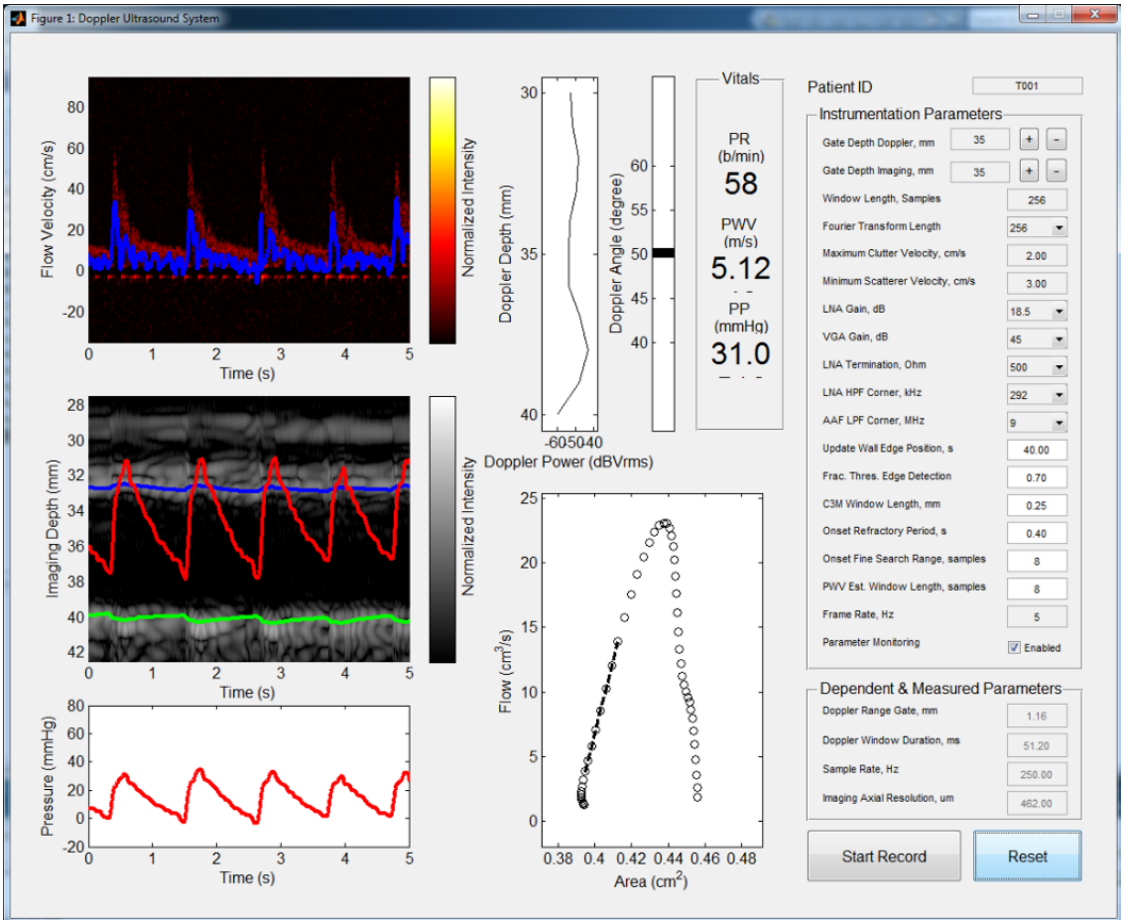

Figure 3-16: Graphic user interface with real-time Doppler spectrogram and M-mode imaging panels with several controls.

3.7 Summary

In this chapter, the design of portable ultrasound system for application-specific ultrasonography is detailed. The probe design with two apertures allows simultaneous spectral Doppler and M-mode ultrasound without a need of an array probe, keeping the electronics with a low channel count and achieving low-cost characteristics.

The electronics system is easily programmable and configurable such that the same device can be used for various combinations of ultrasonography. The system is shown capable of producing voltage pulses to emit the acoustic pulse and preserving the integrity of the ultrasound echoes for the spectral Doppler and M-mode. The produced pressure field patterns are generated as designed. Finally, the graphic user interface provides a real time user feedback in order to acquire high quality ultrasound images with various parameter controllability.

Chapter 4

Proof-of-Concept Human Subject Study

This chapter describes a clinical study conducted on nine healthy human subjects to demonstrate proof-of-concept of the proposed arterial blood pressure (ABP) waveform estimation. This study was approved by the Committee on Use of Humans as Experimental Subjects at the Massachusetts Institute of Technology. The work described in this chapter was published in [40].

4.1 Clinical Consideration

Prior art demonstrated that a spatial mean velocity and an arterial distension waveforms can be estimated using a two single-element ultrasound transducers system [39,46]. The flow velocity is estimated using pulsed Doppler ultrasound under uniform insonation. The distension waveform is estimated from M-mode imaging with echo-tracking. By combining these two parameters, a pressure waveform can be accurately estimated based on the model proposed in Subsection 2.3.1 [39, 46].

However, several challenges in the clinical use of this technique remain. First, the alignment of the probe to a target vessel becomes more challenging than in a flow phantom experiment because the vessel is hidden beneath the skin. Second, the Doppler angle is unknown, as anatomical structures vary from person to person.

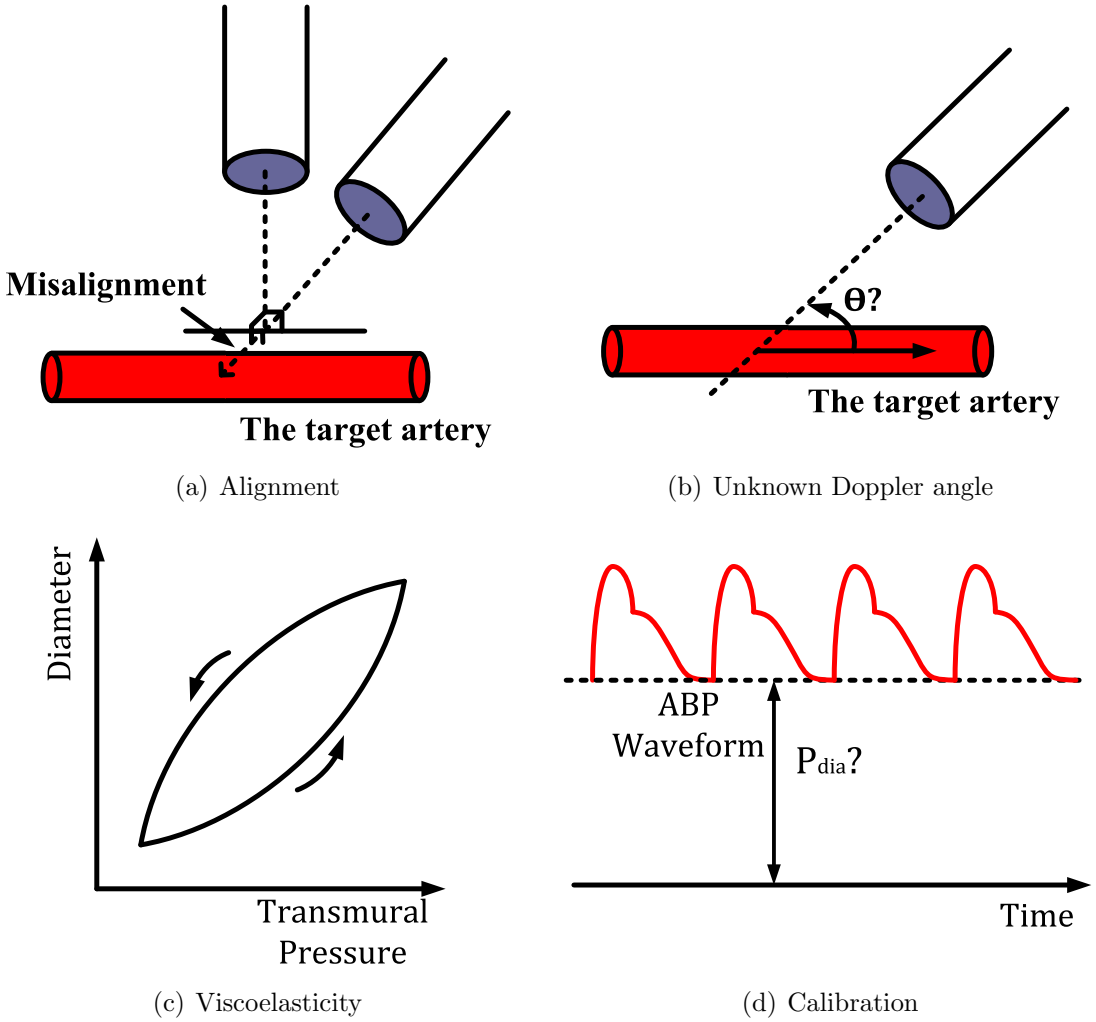

(a) Alignment

(b) Unknown Doppler angle

(c) Viscoelasticity

(d) Calibration

Figure 4-1: Challenges of the clinical use of the proposed ABP waveform estimation technique.

Third, unlike an elastic tube, the arterial wall presents viscoelasticity, as discussed in Subsection 2.2.2. The hysteresis between the pressure and the area due to the viscoelasticity is neglected in the proposed simple ABP waveform estimation model. Finally, the estimation model requires calibration of either the mean or diastolic pressure of the waveform while the pulse pressure can be estimated without calibration.

In order to ensure the alignment of the probe, the sonographer maneuvers the probe to see specific features in the ultrasound images. If the probe is aligned right on top of the vessel, the Doppler signal will be strongest and brightest with the highest peak systole flow velocity. However, given that the transmitted acoustic energy

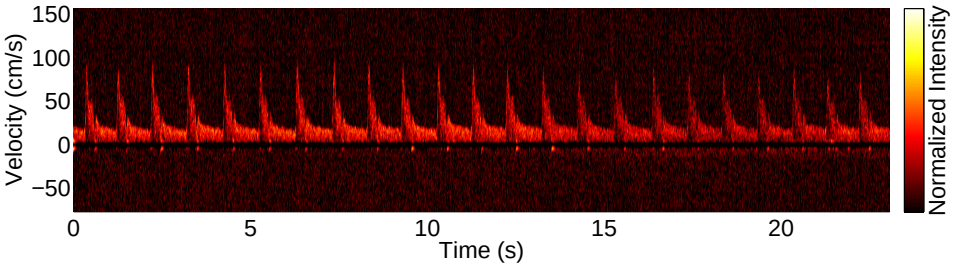

(a) Doppler spectrogram

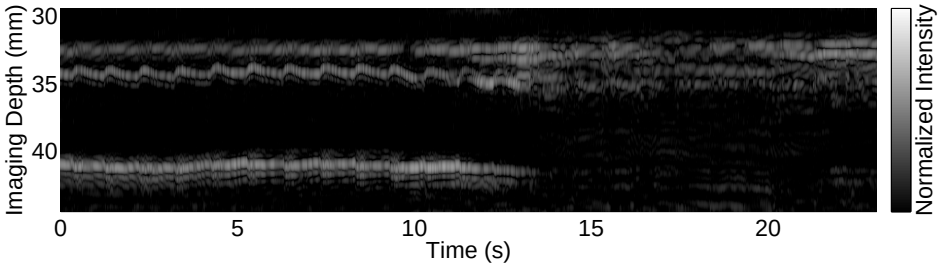

(b) M-mode image

Figure 4-2: Continuous changes of ultrasound images as the vessel tracking is being lost.

is spread due to the uniform insonation, this criterion may not be very sensitive. In the M-mode image, two strong echoes from the anterior and posterior wall will be expected and maximally spaced if the probe is aligned exactly. Since the focused beam is penetrating through the vessel, the echoes are generated strongly by specular scattering from the vessel walls while the lumen presents low echogenicity of erythrocytes. In addition, the distance between the two echoes should range between 6 and 8 mm, which is a reported diameter of the common carotid artery [74] while they are vigorously pulsating. This criterion is more sensitive to ensure the alignment of the probe. Figure 4-2 exemplifies that the probe was initially aligned but eventually displaced laterally to lose track of the vessel. As the probe becomes misaligned, the Doppler signal becomes weak while the strong echoes from the vessel walls are lost in the M-mode image.

For Doppler angle estimation, a cross-beam vector Doppler technique can be used. This technique is discussed in detail in Section 4.2. For this proof-of-concept study, the viscoelasticity is assumed negligible at the carotid artery [75] although it may

introduce small errors. Finally, the diastolic pressure is calibrated to match other measurements as diastolic and mean arterial pressure remains relatively constant over major arteries [33, 76].

4.2 Vector Doppler Technique

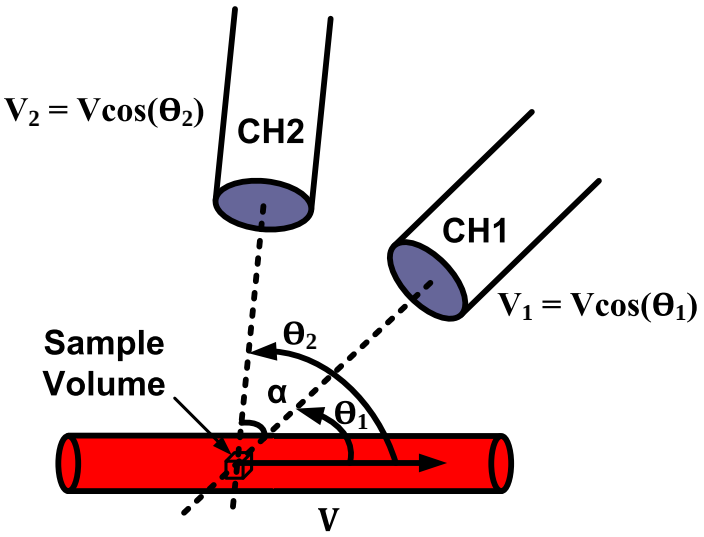

Figure 4-3: Schematic of a two-channel vector Doppler technique [40].

The vector Doppler technique refers to the Doppler angle estimation using multiple Doppler signals with different angles of insonation [77]. Figure 4-3 shows a schematic of the transducers' position in a two-channel vector Doppler. The two acoustic beam axes meet at the cross-beam point while the angle (α) between two axes is pre-defined. If the velocity estimates from each channel show cosine dependency, the Doppler angle (θ_1) can be back-calculated as:

$$\theta_1 = \tan^{-1}\left(\frac{1}{\tan\alpha} - \frac{1}{\sin\alpha}\frac{V_2}{V_1}\right) \quad (0^\circ \leq \theta_1 < 180^\circ) \tag{4.1}$$

where θ_i is the Doppler angle of i-th channel, and V_i is the velocity estimate of i-th channel. In this work, α is set to 40°.

Since the sample volume has a finite size and the flow is not a plug profile, the

velocity estimates depend on the relative size of the sample volume and the variation of the flow velocities inside the target vessel. Therefore, in order to attain the cosine dependency of the velocity estimate, the identical size sample volumes from each channel should be ideally defined at the same location. Such a condition is achieved by the transducers transmitting the same ultrasound pulse, looking at the same sample volume from the equal distances.

Figure 4-4 shows angle estimate errors with the various Doppler angles (θ_1). Two circular ultrasound transducers with a diameter of 6 mm and a center frequency of 2.5 MHz were used in this experiment. The flow was maintained constant. The measured velocity for the high flow was 0.84 m/s, and 0.43 m/s for the low flow.

The figure presents a distinctive pattern. The error becomes small as the Doppler angle deviates from 50°. However, as the Doppler angle reaches 50°, the error increases. From Equation 4.1, the angle estimate is solely dependent on the velocity ratio $\frac{V_2}{V_1}$. Ideally, the velocity estimates should present perfect cosine dependency, but due to high-pass clutter rejection filters, the speeds of flow are overestimated. Such an effect is more pronounced usually in CH2 as most of the Doppler signal is concentrated at low frequencies. This distortion results in the inaccurate velocity ratio, thereby causing greater errors as θ_1 reaches 50°, while θ_2 reaches 90°. Interestingly, when the Doppler angle (θ_1) is exactly 50°, the error is minimized. Due to inherent

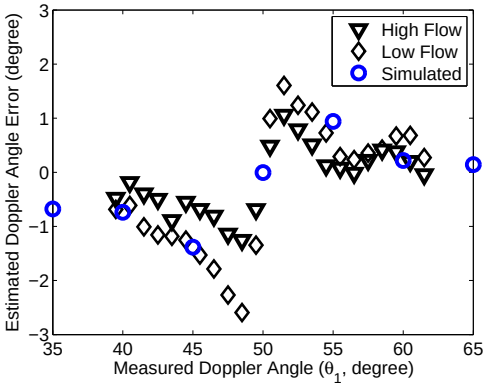

Figure 4-4: Measured and simulated Doppler angle estimate errors in the vector Doppler technique with various flow rate conditions.

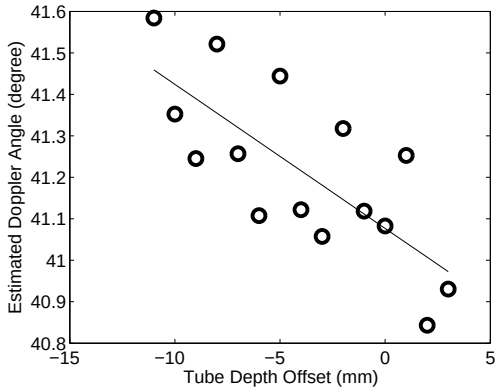

Figure 4-5: Doppler angle estimates with the depth offsets from the targeted depth.

spectral broadening [78], the Doppler spectrum from CH2 appears symmetric around zero frequency, producing a mean frequency shift of zero. The resulting velocity ratio is accurately estimated as zero, producing the correct angle estimate of 50°. This distinctive pattern is also seen in the simulation results overlaid in Figure 4-4. It is noteworthy that the estimate error should be zero when the Doppler angle (θ_1) is 70° because the distortion by the clutter filters for both channels is exactly balanced to result in the correct velocity ratio [77].

The estimate error is smaller with a high-flow setting. In this case, a smaller fraction of the Doppler spectrum is affected by the clutter filters, thereby mitigating the distortion discussed above. This result implies that the systolic flow velocity rather than the diastolic flow velocity is preferred for accurate Doppler angle estimation.

It is shown that the Doppler angle can be estimated with the maximum error between 1.2° and 3° depending on the actual flow velocity. However, in practical situations, the target vessel may not necessarily lie at the cross-beam point. Then, due to the different distances from the aperture, the size of the sample volume inside the lumen from each transducer is different because the beam width changes with depths. If the vessel lies beyond the expected depth, the defined sample volume by CH1 will become larger than that of CH2, although both of them become larger than they are originally intended. The Doppler signals are no longer acquired preferentially from a high-flow line, thereby decreasing the velocity estimates from both channels. The

decrease of V_1 is greater, and the velocity ratio is overestimated. As a consequence, the Doppler angle is underestimated. If the vessel lies shallower than the expected, the Doppler angle will be overestimated because the velocity ratio is now underestimated. Figure 4-5 shows such a trend. Still, the deviation of the velocity ratio is not significant so that even with the 5 mm depth offset, the expected angle error due to the depth error is roughly 0.2°.

4.3 Clinical Study Design

4.3.1 Study Protocol

The main purpose of this study is the proof-of-concept of the proposed ABP waveform estimation on healthy human subjects. The exclusion criteria stated known diagnosis or history of cardiovascular diseases, usage of alcoholic beverages of sedatives in the past 24 hours, prior issues with medical ultrasound, pregnancy, and ages below 18 years or above 60 years. The subjects were recruited verbally. After the prospective subjects were fully briefed, the informed consent was obtained.

The estimated ABP waveform from ultrasound is compared to other blood pressure measurements including a waveform at the finger using a volume clamping method and a sphygmomanometer using an auscultatory method, which was conducted by a nurse at the MIT Clinical Research Center (CRC). The finger waveform was monitored by a Nexfin hemodynamic monitoring device (Edwards Lifesciences, Irvine, California). The sphygmomanometer measurement was done at the contralateral side to the finger waveform measurement.

The subject's left common carotid artery was chosen for the target. The left carotid artery is a major artery which directly branches out from the aortic arch. The carotid artery was adequate in this study because of its dimension, proximity to the heart, and the anatomical structure of not being branched until carotid bifurcation. Figure 4-6 shows the example of placement of the ultrasound probe.

During the study session, the subjects were asked to lie down to eliminate hydro-

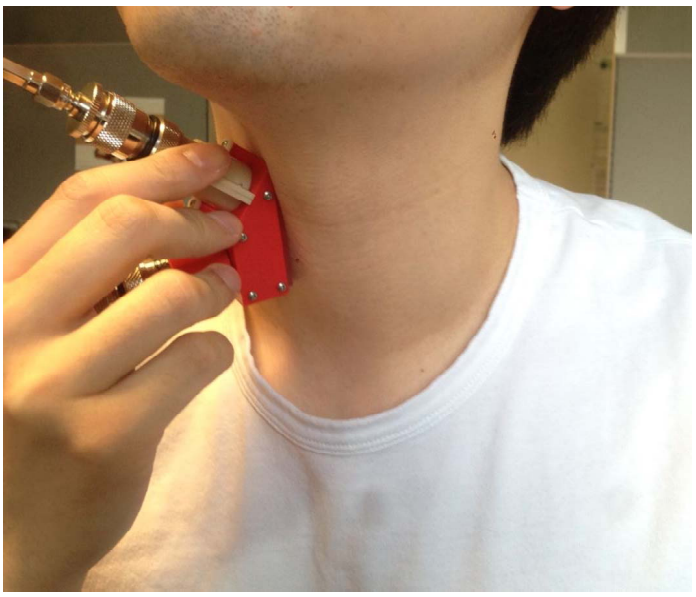

Figure 4-6: Application of the ultrasound probe on the common carotid artery.

static pressure difference between the finger, neck, and upper arm. The finger ABP waveform was continuously recorded while the cuff measurement was conducted every 10 minutes. Once the probe was aligned by the operator, ultrasound images were first captured in the angle mode for several seconds. The system was subsequently switched to the normal mode to record simultaneous Doppler and M-mode images as long as the alignment was maintained. The image acquisition was repeated multiple times.

4.3.2 Signal Processing

For the Doppler angle estimation, the velocity estimates and their ratio are calculated if the velocity estimate from CH1 exceeds a certain threshold (e.g., 0.3 m/s) to only include the high-flow velocity. Then, the Doppler angle estimate is calculated at each time instance. Following this, these estimates are averaged to produce the final Doppler angle estimate.

Due to the wide beam, venous flow from the jugular vein may appear in the acquired Doppler signal. Although the arterial flow profile may contain backflow, as expected by the Womersley's model in Subsection 2.2.1 especially at the aortic valve

closure, the flow velocity during the early systole is of great importance to calculate local PWV based on the flow-area method, which is mostly positive. Therefore, the Doppler spectral intensity beyond the noise floor in the negative frequency band is rejected. Then, the mean frequency shift is calculated to produce the spatial mean velocity waveform. The estimated waveform is low-pass filtered to reject high frequency noise with a cutoff frequency of 30 Hz because 95% of the frequency contents are contained below 12 Hz [79].

To produce the diameter waveform, the wall positions are either manually or automatically identified using a sustain attack filter approach [65]. Then, the echo-tracking windows are applied around the identified depths for the vessel walls. The C3M estimator estimates the displacements of the walls between consecutive pulses [68]. By integrating the displacements, the change of diameter waveform is estimated with a fine spatial resolution. On top of the initial absolute diameter, the complete diameter waveform is produced. Finally, the distension waveform is also low-pass filtered with a cutoff frequency of 30 Hz to reduce high frequency noise.

To calculate the local PWV using the flow-area method, a reflection-free period should be identified. First, an onset detection algorithm is applied on the distension waveform to detect the onset of the systolic upstroke. The algorithm is comprised of two steps: First, a candidate point is identified using the slope sum function approach [80]. Then, the maximum acceleration point around the candidate is identified every beat as the final onset. The same algorithm is also applied to the finger ABP waveform for the onset detection.

From the simultaneously acquired diameter and velocity waveforms, the flow-area loop is plotted every cardiac cycle. Since every heart beat is different, the PWV is calculated from the average of individual PWV estimates from the noisy flow-area plots of individual beats instead of using the ensemble averaged waveforms. The end of the reflection-free period is determined based on the second peak in the acceleration of the vessel walls after the identified onset.

Once the onsets for the pulsating waveforms are annotated, the estimated carotid and measured finger waveform are first synchronized based on heart rate variability.

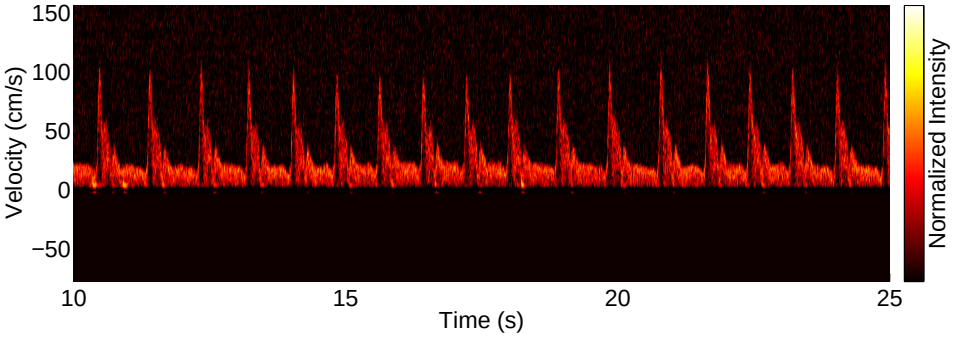

(a) Doppler spectrogram

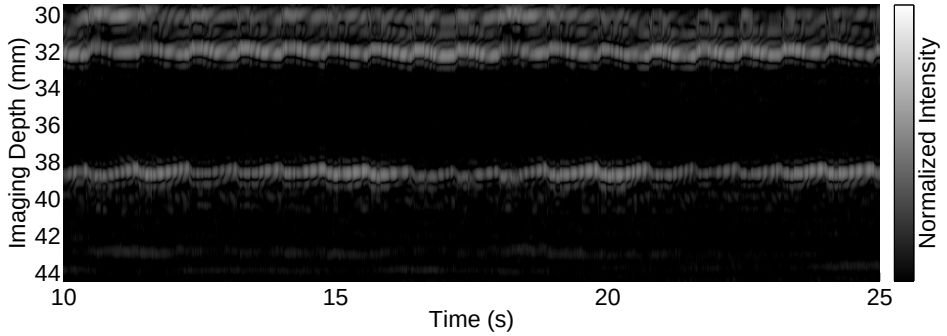

(b) M-mode image

Figure 4-7: Example of raw ultrasound images obtained from the proof-of-concept clinical study.

Subsequently, a delay is added to result in the highest correlation between the two waveforms. The diastolic blood pressure of the carotid waveform is matched to the finger ABP waveform for closer comparison of the pulsatile portion of the waveform.

The similar signal processing procedures were applied for the Valsalva maneuver study and comparison study to an arterial-line in later chapters.

4.4 Clinical Study Results

A total of nine healthy subjects (seven male and two female subjects) participated in this study. Figure 4-7 shows an example of the Doppler spectrogram and M-mode images simultaneously acquired at the common carotid artery of the subjects. The achieved SNR of the Doppler is above 8 dB. The M-mode image shows strong echoes

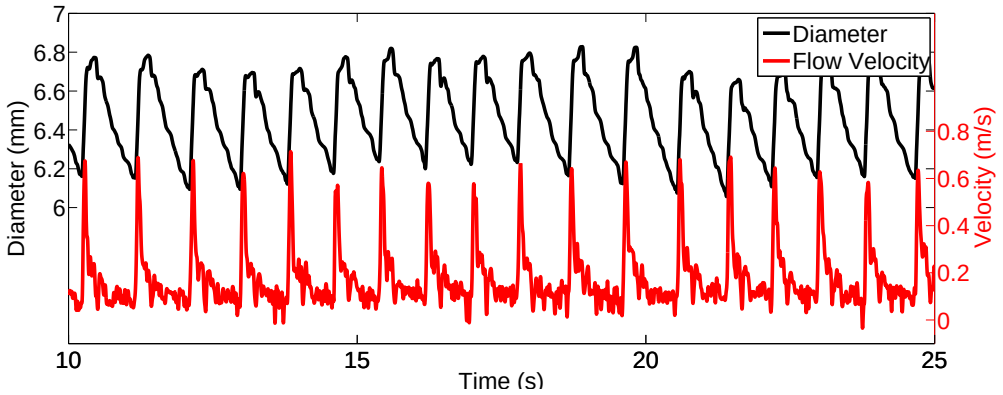

Figure 4-8: Extracted spatial mean flow velocity and diameter waveforms from the raw ultrasound images.

reflected from the anterior and posterior walls. The middle region between the two echoes shows low echogenicity, implying that the focused beam was aligned with the center of the artery. The estimated physiological waveforms from the raw ultrasound images are plotted in Figure 4-8. The flow velocity and diameter waveforms show expected quantitatve behavior with approximately 10% diameter changes relative to the diastolic diameter.

From the physiological waveforms, the flow-area plots are constructed to extract the local PWV. Figure 4-9 shows two examples. The loop starts from the systolic onset and maintains a linear relationship for 40–50 ms between the flow and area where the slope indicates the local PWV. Once the reflected pulse comes back, the loop rotates clockwise. This is because the pressure component of the reflected wave is added to the forward wave while the flow component is subtracted. At the aortic valve closure, slight decrease of flow and area occurs simultaneously. Then, the flow and area gradually return to the baseline during the diastole.

The comparison of the estimated ABP waveform to the finger waveform shows a good agreement in Figure 4-10. In fact, both waveforms present a slow baseline fluctuation. Natural blood pressure fluctuations are believed to be caused by mainly three reasons: respiration, baroreflex (i.e., the spontaneous cardiovascular control loop to maintain the central ABP at a constant level), and thermoregulation at the

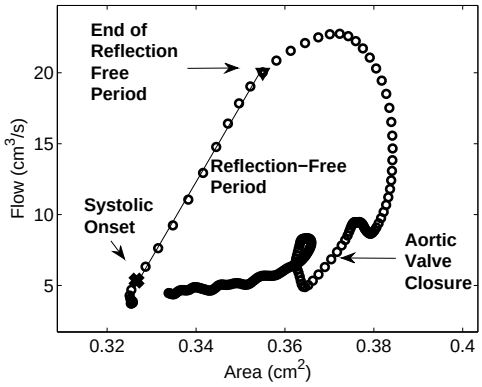

(a) S2 Flow-Area Plot

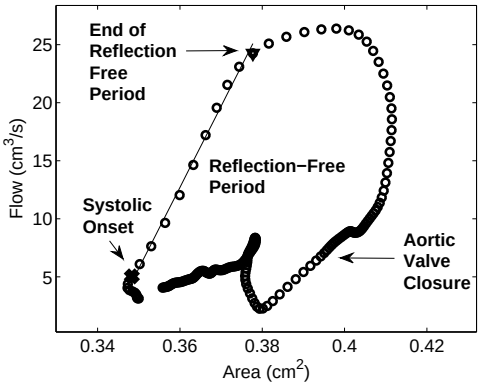

(b) S6 Flow-Area Plot

Figure 4-9: Examples of the flow-area plots obtained from the proof-of-concept clinical study [40].

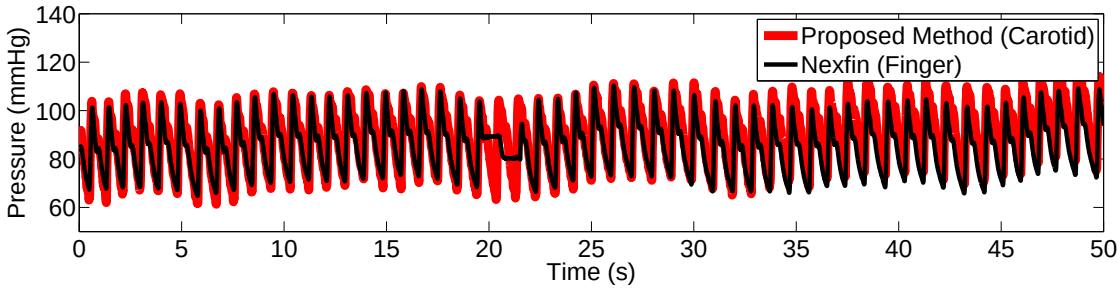

(a) Subject ID: S2

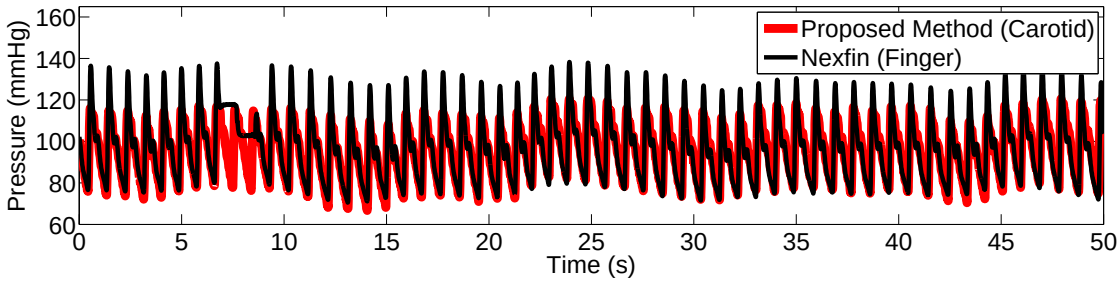

(b) Subject ID: S9

Figure 4-10: Direct comparison of the estimated carotid ABP waveform to the measured finger ABP waveform from the nexfin device in a long-time scale [40].

peripheries [24]. A spectral analysis of the ABP waveform revealed that three separate bands exist for each physiological cause. The respiration corresponds to the high frequency band above 0.25 Hz while the baroreflex is corresponding to the mid

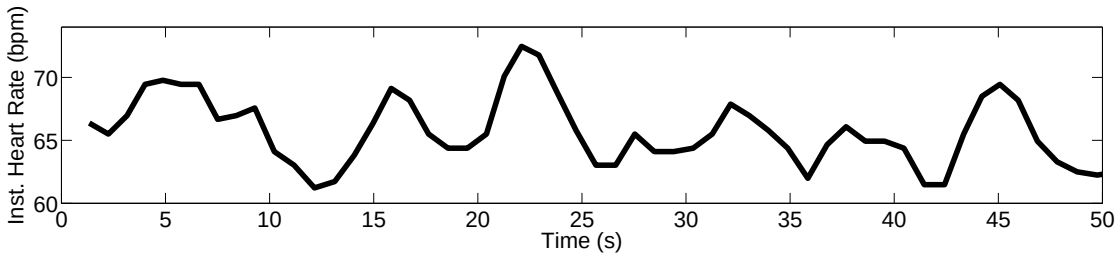

Figure 4-11: Instantaneous heart rate of S9 calculated from the beat-to-beat cardiac period.

band around 0.1 Hz. Based on a period of the observed fluctuation, which is roughly 8–10s, it is likely caused by the baroreflex. In addition, Figure 4-11 supports that an instantaneous heart rate change leads the variation of the baseline ABP, further suggesting orchestration by the baroreflex. Figure 4-10 suggests that the ultrasound measurement to estimate the ABP waveform is capable of tracking the slow baseline fluctuation caused by the underlying cardiovascular control loop, which may be important but not studied extensively yet.

Figure 4-12 shows the detailed comparison on a shorter time scale. Notable discrepancies are observed during the systole. The finger ABP waveforms show much sharper peaks than the estimated carotid waveform. Given that the finger is distal in the arterial tree and closer to the major reflection sites, the finger ABP waveform is expected to display a more augmented shape due to the pulse pressure amplification discussed in Subsection 2.2.2. Hence, these discrepancies are originated from the difference of the measurement sites.

Nevertheless, the discrepancy between the two waveforms is quantified by root mean square error (RMSE). The summary of the estimated PWV and RMSE for each subject is presented in Table 4.1. The standard deviation of the PWV represents intra-subject variability from one data acquisition to the other.

Since the proposed ABP waveform estimation provides the pulsatile portion of the waveform without calibration, the pulse pressure is compared to the other blood pressure measurements. Figure 4-13 compares the pulse pressure estimated from the proposed method to that of the sphygmomanometer and the finger waveform. The

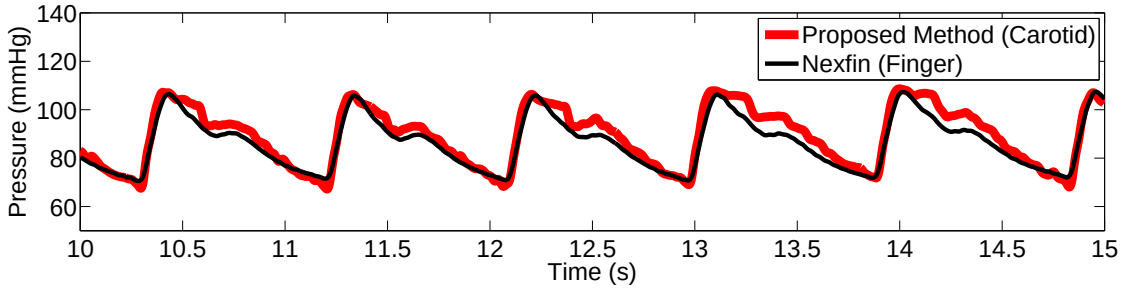

(a) Subject ID: S2

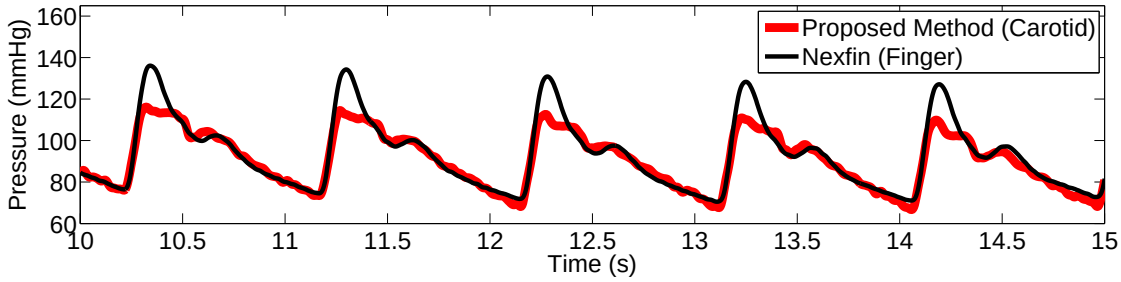

(b) Subject ID: S9

Figure 4-12: Direct comparison of the estimated carotid ABP waveform to the measured finger ABP waveform from the nexfin device in a short time scale [40].

Table 4.1: Pulse wave velocity and root mean square error of waveform comparison in the data with highest integrity [40].

Subject ID	**Age**	**PWV (m/s)**	**RMSE (mmHg)**
S1	23	4.2±0.7	N/A
S2	29	5.6±0.5	6.7
S3	26	7.1±0.7	13.2
S4	29	4.4±0.6	12.1
S5	29	6.3±1.8	4.9
S6	30	6.9±0.6	12.0
S7	26	4.9±0.5	6.4
S8	24	7.2±0.6	17.5
S9	31	5.9±0.6	7.1

error bar represents the intra-subject variability from one data acquisition to the other. The variability of the proposed method is typically a little larger than the other measurements. Except S4, the three measurements generally agree. The differences between the averaged estimation within individual subjects to the intra-subject

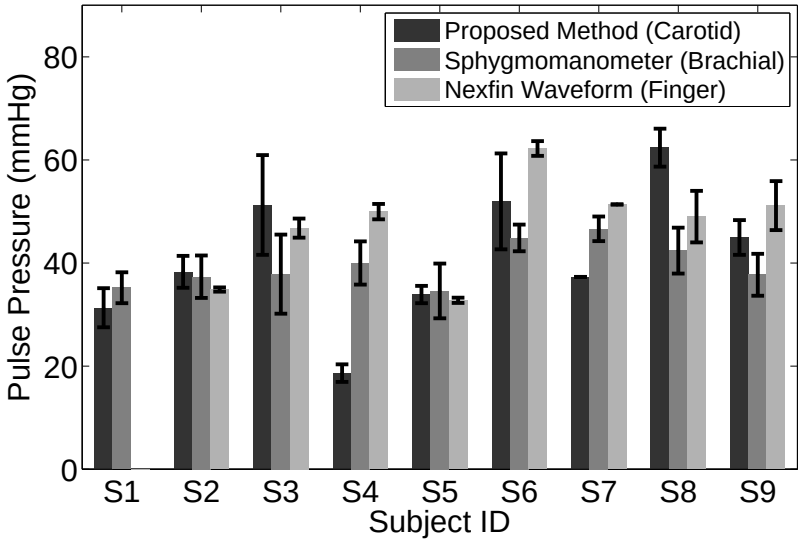

Figure 4-13: Pulse pressure comparison of the proposed method to the sphygmomanometer and the finger ABP waveform. Three data sets with high integrity in the proposed method are selected for comparison except S7 (only one data set) and S9 (two data sets). The data integrity is evaluated based on the linearity of the reflection-free period in the flow-area plot, the stability of a diameter waveform, and the signal-to-noise ratio of the Doppler signal. The data set of S1 misses the Nexfin waveform [40].

averaged sphgymomanometer measurement and the finger waveform are 1.49±11.7 mmHg and -4.92±12.9 mmHg. The difference between the sphygmomanometer and the finger waveform is -7.09±6.46 mmHg, which is not significantly better than the other comparisons. Still, the correlation between the sphygmomanometer and the finger waveform is higher than the others. The subject S4 had two study sessions which resulted in consistent under-estimation of the pulse pressure. It is suspected that the ultrasound images were obtained at or close to the carotid bifurcation where the fluid dynamics is not simple as the proposed model assumes. The proposed estimation shows modest overestimation in the subject S8. Due to the pulse pressure amplification, the pulse pressure at the carotid is normally expected slightly lower than the pulse pressures at the other sites. However, such a pattern is less evident due to the relatively high variations of the proposed estimation.

This pulse pressure comparison shows the general agreement of the proposed

method to the other measurements. Nevertheless, this plot also shows that improvements can be made. In fact, it should be emphasized that neither the sphygmomanometer nor the finger ABP waveform are the gold standard, as they are also non-invasive and measured at different sites.

4.5 Summary

This clinical study validates that the designed prototype device is capable of producing the proposed ABP waveform estimation on healthy human subjects at the common carotid artery. The device measures the spatial mean flow velocity and diameter waveform simultaneously in addition to the Doppler angle based on the vector Doppler technique. The designed prototype was proven feasible at the common carotid artery and convenient for a spot check at ambulatory clinical settings.

The measured physiological waveforms are used to construct the flow-area plots to extract the vessel elasticity. As expected, the flow-area plot has a highly linear segment, indicating the reflection-free period where the local PWV is extracted from the slope.

The estimated ABP waveform shows the baseline fluctuation possibly caused by the baroreflex, which is an essential part of the cardiovascular control system. However, this control system has not been extensively studied due to the lack of the non-invasive ABP waveform measurement techniques at the central sites. This study, using the prototype, shows the promising potential to acquire ABP waveform in ambulatory clinics. However, the technique leaves ample room for improvements for more accurate and consistent estimation of the pulse pressure and the ABP waveform.

Chapter 5

Motion-tolerant Ultrasound Measurements

The proof-of-concept study discussed in Chapter 4 suggests that the pulse pressure estimation has room for improvements. In addition, the results show beat-to-beat variation of the ABP orchestrated by the cardiovascular control loop.

Further studies on this variation require continuous monitoring of the ABP waveform for an extended period of time. In that sense, an operator-less application of the device is preferable. In addition, to minimize uncertainty in the ultrasound measurements due to the alignment, the measurements need to be desensitized to the misalignments. This chapter introduces motion-tolerant ultrasound measurements for physiological waveform monitoring including arterial blood pressure (ABP) waveform. The content of this chapter was published in [81].

5.1 Widebeam Insonation

Typical commercial ultrasound scanners transmit and receive a focused beam generated by a transducer array to achieve high spatial resolution. The duration of the acquired images usually spans several seconds while the sonographer holds the probe steady and aligned to the target. If the focused beam is sent in a fixed direction like the M-mode, the target will be easily lost with small displacements of the probe.

Unlike the M-mode, B-mode uses multiple focused beams to scan a wide region to ensure coverage of the target by compromising temporal resolution (i.e., frame rate). To regain a high frame rate, a plane wave is transmitted while the focusing is done at digital parallel receive beamformation. This approach is recently enabled with the help of advancement in graphical processing unit-based platforms [82]. Nevertheless, these platforms are power hungry and unsuitable for the goal of designing a low cost and portable system.

In this ABP waveform estimation, a high temporal resolution is required to capture the fast traveling pulse waves. Unfortunately, the M-mode using the focused beam faces challenges of vessel motion, a possible significant source of errors. Prior art utilized a beam steering approach to attain reliable tracking of the middle cerebral artery [73]. This approach continuously evaluates the quality of transcranial Doppler signals and updates the beam direction as necessary. The prototype system with a 64-channel two-dimensional array is justified for tracking deep anatomical structures where manual scanning is demanding. However, for superficial arteries, a system with a low channel count may be sufficient. In addition, the smaller number of electronics channels advances the goal of a portable, lower cost system. In this section, the use of single-element unfocused imaging to maximize the lateral offset tolerance of the measurements is proposed. Similar to plane wave imaging, an unfocused plane wave with a wide beam width is transmitted. In addition, the received beam is acquired in a plane wave manner using a single element transducer.

Doppler ultrasound

The pulsed Doppler ultrasound with uniform insonation is used to measure spatial mean velocity. The wide beam width ensures the reception of blood flow signals with lateral offsets. To achieve the necessary uniformity, a near-field pattern, which is laterally uniform within the size of the aperture, is considered. Typically, the axial pattern along the beam axis is messy especially when created by a circular aperture. Thus, the rectangular aperture with a high aspect ratio is proposed to reduce intensity variation while achieving sufficient axial uniformity.

An axially long sample volume is defined by transmitting a long ultrasound pulse

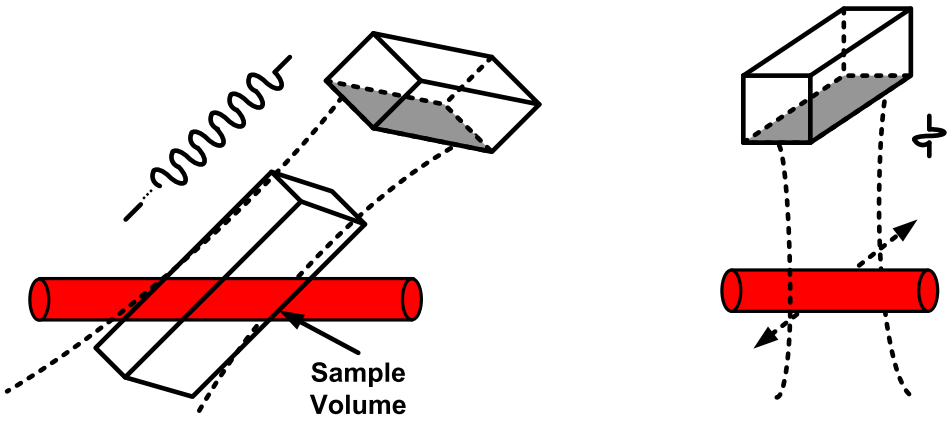

(a) Doppler ultrasound (b) M-mode imaging

Figure 5-1: Beams generated by a wide rectangular ultrasound transducers for (a) Doppler ultrasound and (b) M-mode imaging.

to completely cover the cross-section. Figure 5-1(a) illustrates such a sample volume. Due to backscattering from adjacent tissues, the clutter strength generally increases. Fortunately, the spectral characteristics of the clutter are distinctively separated from the blood flow. Therefore, unless the clutter saturates the analog front end, the clutter rejection highpass filter eliminates the clutter and preserves the Doppler signal integrity. As a result, the accurate spatial mean velocity measurement remains intact.

M-mode Imaging

In this wide beam unfocused imaging, the echoes reflected from the vessel walls are consistently received even with lateral offsets. Figure 5-1(b) illustrates the use of a rectangular aperture transducer to produce the wide beam for the M-mode. In addition, if the beam pattern is uniform, the strength of these echoes is consistent even with offsets. However, the clutter, assumed stationary because it originates from the stationary tissues, again increases due to backscattering from the adjacent tissues. Unlike the Doppler ultrasound, it is challenging to eliminate the increased clutter because of its similar spectral characteristics to the echoes of interest in the RF domain.

It is noteworthy that a fundamental trade-off between signal-to-clutter ratio (SCR) and the lateral beam width exists. The excessive clutter corrupting the echoes of

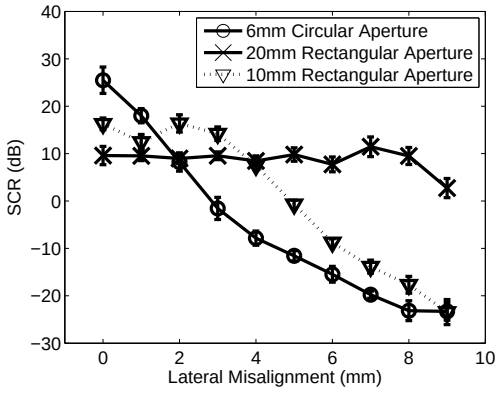

Figure 5-2: Simulated contrasts of the M-mode image with the lateral misalignments when different apertures are used.

the vessel walls may result in underestimation of the echo displacements because the clutter is mostly stationary. Therefore, the key consideration is to extend the beam width, which directly determines the offset tolerance, until the SCR or contrast (i.e., relative strength between the echo of interest to clutter) reaches the minimally acceptable level for accurate diameter waveform estimation. In fact, the expected contrast can still be high due to the strong specular scattering from the vessel walls.

Figure 5-2 shows the simulated SCR changes as the lateral misalignments vary using various apertures. If the focused beam, generated by the circular aperture, is used, the highest SCR is obtained at zero offset, but the SCR quickly drops below 10 dB which is initially considered acceptable. With rectangular apertures of the widths of 10 mm and 20 mm, the SCR at no offset is lower than that with the focused beam, but the same level is maintained over a wide range of misalignments. From the previous clinical study, the observed contrast is typically above 25 dB with the circular aperture that the simulation mimics, the SCR of 10 dB can be achieved with a 20 mm width rectangular aperture transducer. As a result, the aperture size is for carotid imaging is chosen to be 20 mm$\times$6 mm.

Additionally, contrast enhancement techniques can be employed to better locate the arterial walls and place the tracking windows. Simple highpass filtering using an FIR filter or blind source separation-based methods were introduced in prior art [83].

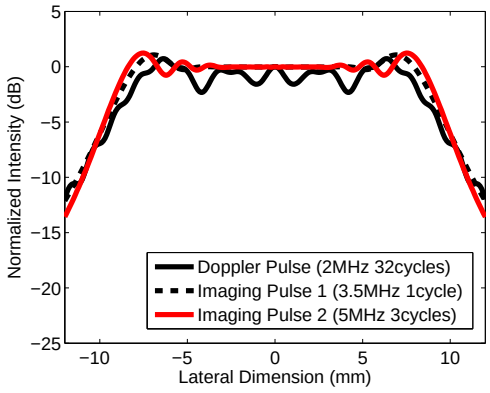

Figure 5-3: Simulated pressure field intensity patterns at the depth of 25 mm in a lateral dimension with various pulsing conditions [81].

Finally, Figure 5-3 shows that the lateral pressure field intensity patterns are uniform in all pulsing conditions with the proposed rectangular aperture transducer at the depth of 25 mm. The pressure field shows a small variation when the Doppler pulse is simulated. However, this variation is insignificant compared to the variation in the developed velocity profile. Therefore, the vessel cross-section is considered uniformly insonated for the pulsed Doppler. If a higher frequency ultrasound pulse such as the imaging pulses is transmitted, lateral uniformity generally improves.

5.2 Intensity Reduction Model Estimator

In the previous chapters, echo-tracking techniques such as the C3M estimator based on cross-correlation were utilized to produce a change of diameter waveform. As the stationary clutter increases, the echo displacements are subject to underestimation. This section describes an intensity reduction model (IRM) estimator to mitigate such influences [81].

Cross-correlation based methods estimate a phase shift between RF lines obtained from consecutive pulse transmissions. Instead, the IRM estimator focuses on intensity reduction of a residual RF line after subtracting consecutive RF lines due to the movement of the echo of interest. For example, if the echo from consecutive RF lines is barely shifted due to no scatterer movement, the residual echo will have a low

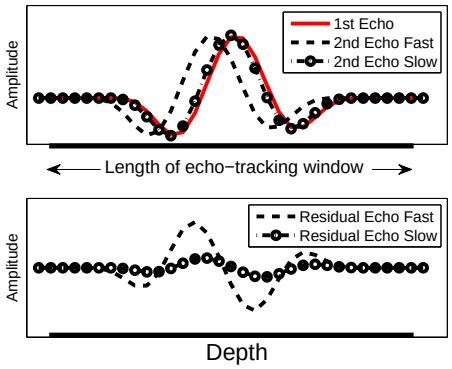

Figure 5-4: Consecutive echoes and residual echo after subtraction produced by a fast or a slow moving scatterer cases [81].

average intensity. However, if the scatterer moves significantly, the residual echo will have a higher average intensity. Figure 5-4 illustrates this phenomenon.

To detail the theory of operation, consider $y_i(t)$ is the RF line acquired from i-th pulse, and $z_i(t)$ is the residual RF line after the subtraction of y_i and y_{i+1} as:

$$\begin{aligned} y_1(t) &= g(t)e^{j2\pi f_0 t}, \quad y_2(t) = g(t-T_d)e^{j2\pi f_0(t-T_d)} \\ z_1(t) &= y_2(t) - y_1(t), \quad T_d = \frac{2v}{cPRF} \end{aligned} \tag{5.1}$$

where $g(t)$ is the envelope, f_0 is the center frequency of the pulse, PRF is the pulse

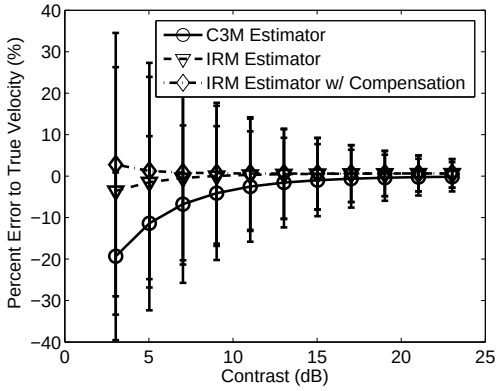

Figure 5-5: Numerically simulated performance comparison between the C3M and the IRM estimator in various contrast environments [81].

repetition frequency, c is the speed of sound, v is the speed of the scatterer, and T_d is the increase of round-trip time of the pulse. Then, the averaged intensity reduction (IR) normalized to the original intensity can be formulated as [81]:

$$\begin{aligned}
I_{y_1} &= \int_{-\infty}^{\infty} |y_1(t)|^2 dt = \int_0^{\frac{M}{f_0}} |g(t)|^2 dt \\
I_{z_1} &= \int_{-\infty}^{\infty} |y_2(t) - y_1(t)|^2 dt \\
&= \int_{-\infty}^{\infty} |g(t)|^2 + |g(t-T_d)|^2 - 2g(t)g(t-T_d)\cos(2\pi f_0 T_d) dt \\
&= \int_0^{\frac{M}{f_0}} |g(t)|^2 dt + \int_{T_d}^{\frac{M}{f_0}+T_d} |g(t-T_d)|^2 dt \\
&\quad - 2\cos(2\pi f_0 T_d) \int_{T_d}^{\frac{M}{f_0}} g(t)g(t-T_d) dt \\
&= 2\int_0^{\frac{M}{f_0}} |g(t)|^2 dt - 2\cos(2\pi f_0 T_d) \int_{T_d}^{\frac{M}{f_0}} g(t)g(t-T_d) dt \\
IR &= \frac{I_z}{I_{y_1}} \simeq (2 - 2\cos(2\pi f_0 T_d))
\end{aligned} \tag{5.2}$$

assuming the envelope $g(t)$ is heavily concentrated and evenly distributed between T_d and $\frac{M}{f_0}$ where M is the number of a pulse cycle. Therefore, the speed of the moving scatterer can be determined as:

$$v = \frac{cPRF}{4\pi f_0} \cos^{-1}(\frac{2 - IR}{2}) \tag{5.3}$$

To implement the IRM estimator, the high-pass filtered M-mode image is generated by subtracting the consecutive RF lines, which is equivalent to applying an FIR filter with coefficients of [1 -1] in the time domain at every depth. Then, the echo-tracking windows are defined around the identified wall positions to calculate the intensity reduction. From the intensity reduction, the displacement or the wall velocity can be calculated at each time instance, which is integrated over time to produce the change of diameter waveform.

Figure 5-5 compares the performance of the echo-tracking methods in numerical simulation. The simulation assumes the length of the tracking window is twice the

pulse length. Since identification of the exact wall positions can be challenging in low contrast environments, it is desirable to have margins to ensure that the window captures the echoes of interest. In addition, a sine wave with the same center frequency as the pulse is assumed as the simplest stationary clutter model.

The simulation results show that on average the IRM estimator experiences less underestimation of the echo displacement as the clutter increases. In high contrasts, the velocity estimates from both estimators are accurate. The velocity estimates from both estimators display increased variation as the contrast gets lower due to the interference between the clutter and the echo of interest in random phases. However, this effect is averaged out as the phase relation progressively changes as the echo slides over the static clutter in the background. As a result, the average estimate performance generally determines the distension waveform measurement accuracy. The simulation results clearly show that the IRM estimator outperforms the C3M estimator in low contrasts.

In fact, the intensity of the original echo is overestimated due to the contribution from the clutter. From Equation 5.3, underestimation of the intensity reduction (IR) leads to velocity underestimation. The amount of overestimation is a function of the contrast and the relative length of the tracking window to the transmitted pulse length. Thus, this overestimation can be pre-calculated and compensated for. If pre-calculated compensation is introduced, the velocity underestimation will be further mitigated in low contrast environments, as Figure 5-5 shows.

5.3 Adaptive Clutter Rejection for Doppler Angle Estimation

In Section 4.2, the vector Doppler technique is discussed to estimate the Doppler angle. This technique can also be utilized in the proposed unfocused imaging for motion-tolerant ultrasonography. The Doppler signals are acquired using the uniform insonation with laterally wide and axially long sample volumes. In comparison to

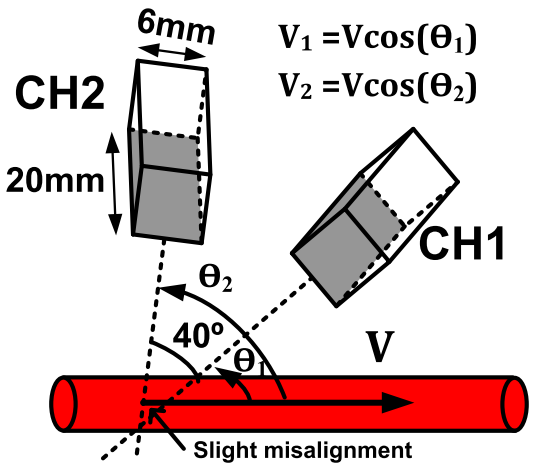

Figure 5-6: Representation of two wide rectangular ultrasound transducers for the vector Doppler technique with the uniform insonation [81].

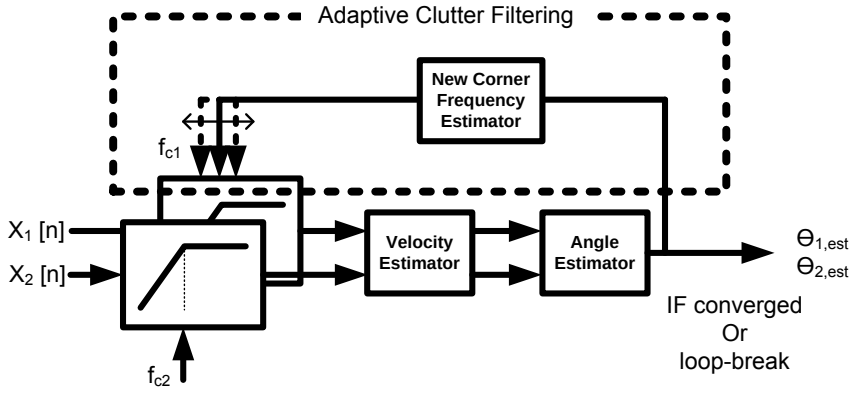

Figure 5-7: Block diagram of the corner velocity adjustment loop for adaptive clutter filtering [81].

the case in which the vector Doppler signals are acquired preferentially from the high flow, the angle estimate error with the uniform insonation increases. Since the Doppler signals from the uniform insonation contain a greater portion of low frequency contents, they are more distorted by the clutter rejection filters.

To limit the Doppler angle error of $\pm 2°$, equivalent to the percentage error of $\pm 5\%$, adaptive clutter filtering is proposed [81]. Adaptive filtering helps balancing distortion by the clutter rejection filters among individual channels by iteratively adjusting the corner velocity of the clutter filter. Equation 4.1 shows the Doppler

angle estimate is determined solely by the velocity estimates ratio ($\frac{V_2}{V_1}$). By adjusting the corner velocity of the CH1 clutter filter, the correct velocity ratio is obtained, thereby producing less angle errors. Figure 5-7 illustrates a feedback loop to adjust the corner velocity. First, the Doppler signals are filtered with the same corner velocities, producing an initial angle estimate. Based on the current estimate, the highpass corner velocity for CH1 is increased, which distorts the velocity estimate V_1. Then, the velocity ratio is re-calculated, giving an updated angle estimate. This procedure iterates until the angle estimate converges.

5.4 Experimental Validation

5.4.1 Flow Phantom Setup

To validate the proposed motion-tolerant ultrasonography, a flow phantom was constructed that consists of a latex rubber tube, a diaphragm pump, and a reservoir. The phantom circulates blood-mimicking fluid (Shelly Medical Imaging Technologies, London, ON, Canada) [84]. The inner and outer diameters of the tube are 6.35 mm and 12.7 mm, respectively. The experimental setup has a 3-D translational stage to finely control the position of the ultrasound probe with a 1 mm resolution. In addition, the rotary stage is attached to fine-tune the angle of insonation with a 1° resolution.

Besides the flow phantom experiment, ultrasound images on a human subject were also collected to test the performance of the IRM estimator in low contrast environments by using artificial clutter as well as *in-vivo* clutter.

The ultrasound probe consists of two wide rectangular (20 mm× 6 mm) transducers fixated by plastic parts. The transducers were custom-designed and manufactured (Imasonic, Voray sur IOgnon, France). The center frequency of the transducer is 3.65 MHz, and the relative bandwidth is about 100%.

The supply voltage of the pump was modulated to produce pulsatile pressure and flow. A flowmeter for water was used to measure a volumetric flow rate. Figure 5-8

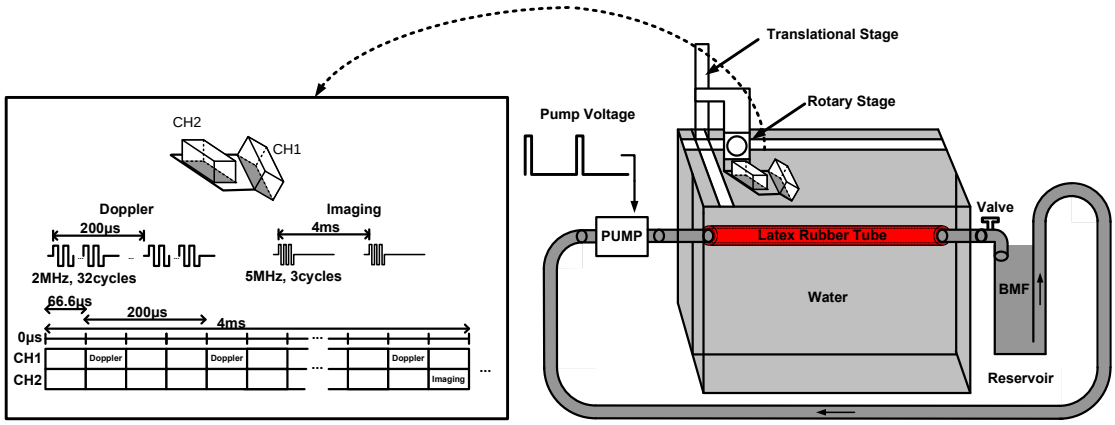

Figure 5-8: Schematic of the flow phantom setup [81].

shows a schematic diagram of the experimental setup.

5.4.2 Data Acquisition

The acoustic pulse for the Doppler ultrasound is generated by exciting the transducer with a 32-cycle square voltage pulse. The center frequency of the Doppler pulse is 2 MHz. The pulse for the M-mode is a three cycle voltage pulse at 5 MHz. The acoustic beam generated by the CH1 transducer nominally insonates the tube at 50°, and the other transducer makes perpendicular insonation. The PRFs for the Doppler and the M-mode are 5 kHz and 250 Hz, respectively. For the M-mode on human subjects, the center frequency was switched to 3.5 MHz for a narrower elevational beam width at the target depth while a single cycle pulse is transmitted. The designed ultrasound scanning system, detailed in Chapter 3, was configured to accommodate the described ultrasonography. The usage of the designed system was approved by the Committee On the Use of Humans as Experimental Subjects at the Massachusetts Institute of Technology.

5.4.3 Experimental Results

Flow velocity, distension waveform, and Doppler angle measurement

Figure 5-9 shows the integrated Doppler power and spatial mean velocity estimates

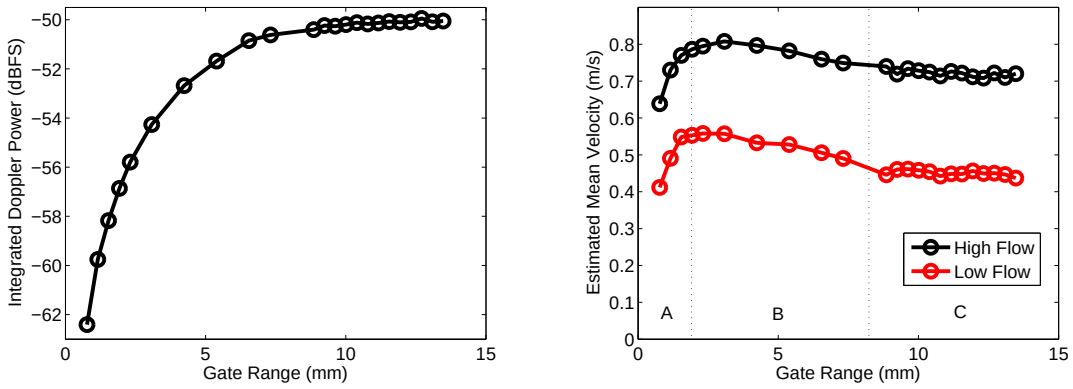

(a) (b)

Figure 5-9: (a) The change of the integrated Doppler power and (b) the spatial mean flow velocity estimates as the gate range increases [81].

as the gate range increases, which determines the length of the sample volume. While the center of the sample volume is fixed at the center of the tube, the integrated Doppler power increases as the Doppler signal is received from a greater number of scatterers. Beyond the gate range of 9 mm, the Doppler power increases insignificantly because the tube cross-section is already completely insonated. In fact, the increase of the Doppler power is linearly related to the coverage of the elliptical cross-section originated from the oblique angle of insonation.

Figure 5-9(b) shows the resulting spatial mean velocity estimate. In region A and B, the Doppler signal is preferentially acquired from the high flow lines. In region A, due to low SNR, the velocity estimate decreases with the shorter pulse. In contrast, the trend in region B is dominated by the effect of including lower flow lines as the gate range expands. Nevertheless, the velocity is over-estimated. In region C, the Doppler signal is obtained from the uniform insonation while maintaining high SNR, thereby resulting in the correct velocity estimate. Beyond the complete cross-section coverage at 9 mm, the velocity estimate reaches the terminal value.

Figure 5-10 presents the averaged Doppler spectra in various gate ranges. With a gate range of 0.8 mm, the Doppler intensity is too weak while the profile accentuates high frequencies. At 4.2 mm, the intensity increases, but the high frequency content is still overemphasized. Beyond the gate range of 9.2 mm, the Doppler spectra

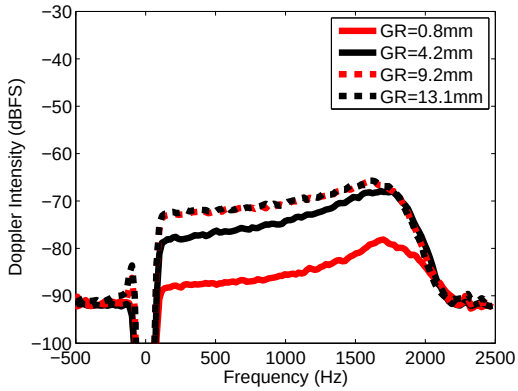

Figure 5-10: The change of the Doppler spectra as the gate range increases [81].

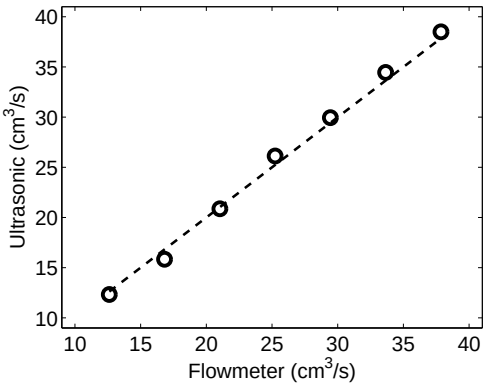

Figure 5-11: Validation of the ultrasound velocimetry compared to the flowmeter measurement while water is circulated [81].

converges, faithfully representing the velocity profile consistent with the explanation above.

While transmitting a long ultrasound pulse, volumetric flow rate estimation is validated in comparison to the measured flow rates in Figure 5-11. Since the flowmeter is designed for water, micro air bubbles were generated by agitating tap water, which acted as primary ultrasound reflectors. Normalized root mean square error (NRMSE) is 2.66% between two measurements, suggesting that the proposed ultrasound velocimetry is accurate.

The diameter change waveform estimated using the unfocused imaging is directly compared to that from the focused beam in Figure 5-12. The NRMSE between the

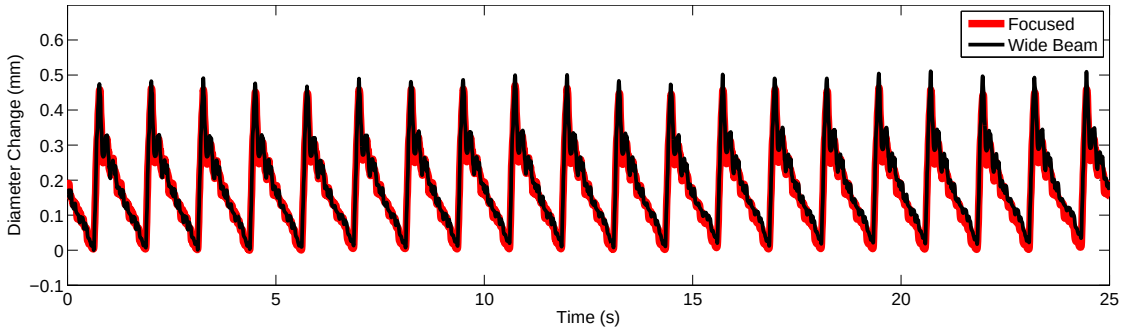

Figure 5-12: Comparison between the estimated diameter waveforms using the wide unfocused beam and the focused beam [81].

two waveforms is calculated as 4.63%.

The Doppler angle is also estimated while the vector Doppler techniques are performed using the uniform insonation achieved by the proposed unfocused imaging. Figure 5-13(a) shows the angle estimate error in the high and low flow settings. The angle error generally decreases when the angle is estimated at the high flow. Figure 5-13(b) shows improvement of the Doppler angle estimation thanks to the proposed adaptive clutter filtering. As the adaptive filtering balances the effect of the clutter filters to restore the velocity ratio, the RMSE of angle estimates is reduced from 3.0° to 1.3°. The maximum estimate error is also contained within ±2° even with the low flow settings.

Figure 5-14(a) presents the progression of the angle estimate error as the corner velocity adjustment loop runs. As the corner velocity is updated, the angle estimate error gradually decreases toward zero. Figure 5-14(b) shows the progression of the updated corner velocity. The corner velocity of CH1 starts at 4 cm/s to a higher final value. If the actual Doppler angle (θ_1) greatly deviates from 50°, the final corner will velocity increase a little because the Doppler signal of CH2 is not greatly affected either. However, if the Doppler angle is close to 50°, the final corner velocity will be high to match the large distortion of the Doppler signal at CH2. Especially, if the Doppler angle is very close to 50°, excessive filtering of the Doppler signal may break this adjustment loop to avoid instability otherwise a new corner velocity may be set infinite. From these results, the spatial mean flow velocity, diameter waveform, and

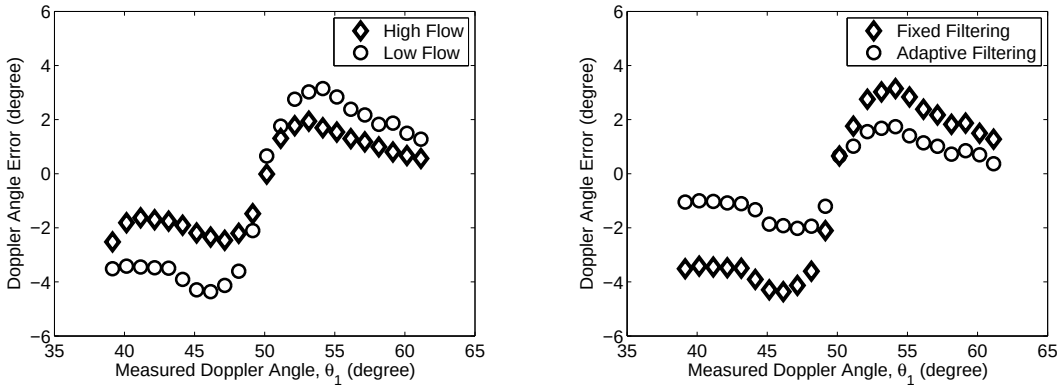

(a) (b)

Figure 5-13: (a) The Doppler angle estimate error plots with different flow rate settings (b) The performance comparison between the fixed and adaptive clutter filtering approach in the low flow setting [81].

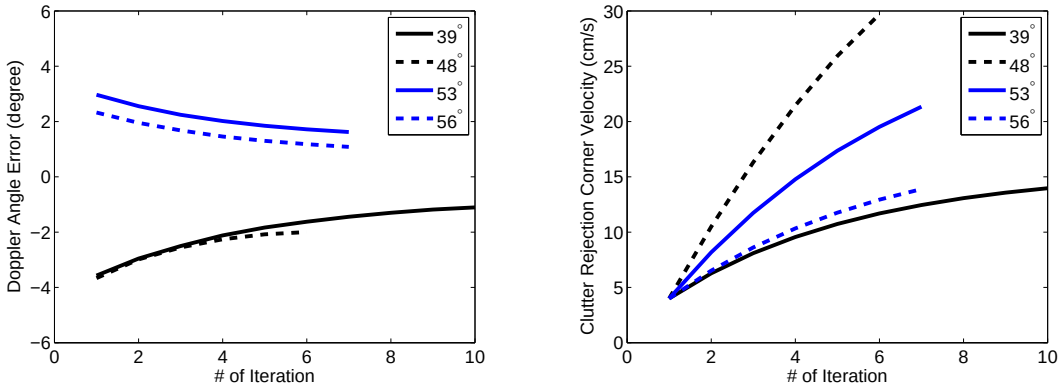

(a) (b)

Figure 5-14: The progression of (a) the angle estimate errors and (b) the high-pass corner velocities as the adjustment loop progresses.

Doppler angle measurements are validated under no lateral offset.

Misalignment Tolerance

Now, the estimation consistency of these parameters is tested with various lateral offset conditions. Figure 5-15 shows the spatial mean flow velocity estimates with lateral offsets under various flow rate conditions. The estimates are consistent within $\pm 5\%$ over ± 8 mm offsets except at ± 7 mm. The variation is attributed to the variation in the lateral pressure field pattern. In that regard, the overestimation at ± 7 mm is

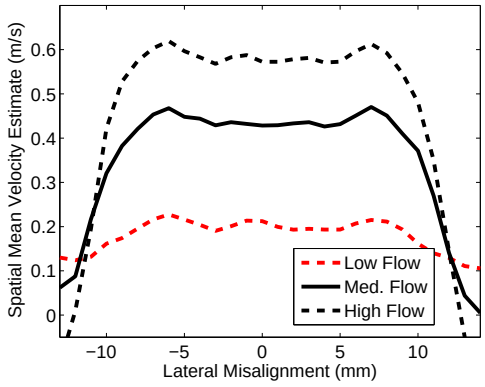

Figure 5-15: The spatial mean velocity estimates with lateral offsets [81].

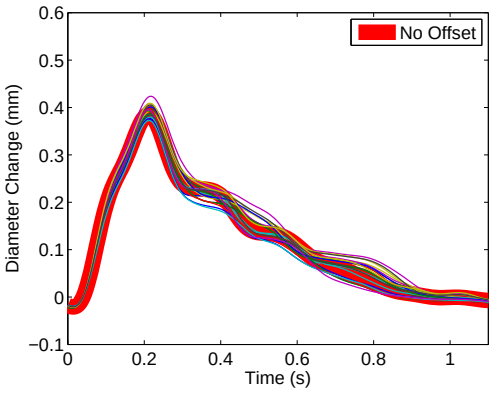

Figure 5-16: Diameter change waveforms with various lateral offsets up to ±8 mm compared to the waveform without offset [81].

attributed to the edge effect that slightly accentuates high flow in the center of the tube.

The diameter change waveform is also tested in various lateral offsets as shown in Figure 5-16. The figure shows the ensemble averaged diameter change waveforms up to ±8 mm offsets compared to the waveform at no offset. The normalized root mean square deviation from the waveform without offset is 3.44%. Slight discrepancies among the waveforms are attributed to the non-uniform lateral field pattern. The discrepancy at the early systole may induce slight variations in the local PWV estimation based on the flow-area method.

These results demonstrate that the spatial mean flow velocity and diameter wave-

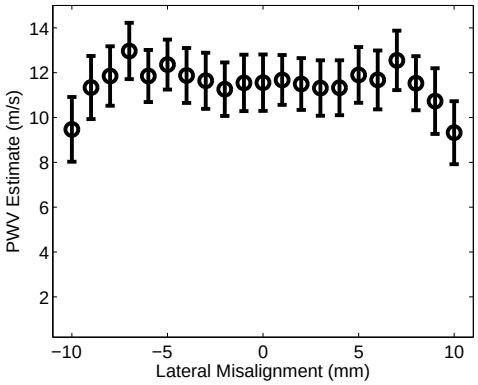

Figure 5-17: The PWV estimates with various lateral offsets [81].

forms can be consistently estimated regardless of the lateral offsets roughly up to the beam width. In addition, given that the Doppler ultrasound is tolerant to the lateral offsets, it is implied that the Doppler angle estimation is also tolerant of the lateral offsets. In addition, the uniform insonation through unfocused imaging eliminates the dependency of the flow velocity estimates on depth. Therefore, the Doppler angle estimate also becomes tolerant to depth errors.

Provided the relevant physiological waveforms are consistently estimated, the PWV estimation is also tested with the lateral offsets as Figure 5-17 shows. Each data point is derived from five independent data sets consisting of 30 simulated cardiac cycles. The PWV estimates show overestimation at ± 7 mm. Except for these offsets, the PWV estimates are consistent up to ± 8 mm. The slight overestimation is attributed to overestimation of the flow velocity in Figure 5-15.

Finally, the pressure waveform estimation was tested while random lateral offsets within ± 8 mm were introduced manually through the 3-D translational stage. The Doppler spectrogram and the M-mode image show consistent pulsation patterns in spite of lateral motions as shown in Figure 5-18. The M-mode image clearly shows the echoes from the inner boundaries of the anterior and posterior walls. The PWV of the tube is calculated from the moving average of PWV estimates for the past 24 simulated cardiac cycles to reduce variability. The estimated pressure waveform shows the consistent pulsatile pressure changes and pulsation patterns. Although 24

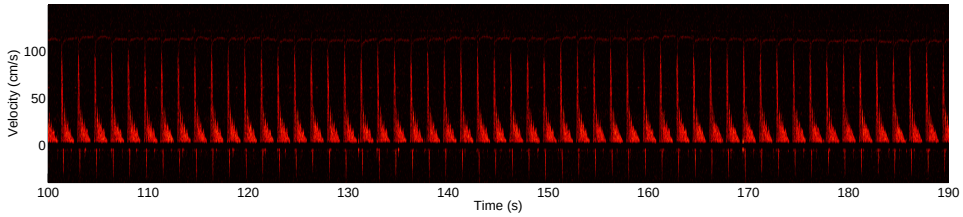

(a) Doppler spectrogram

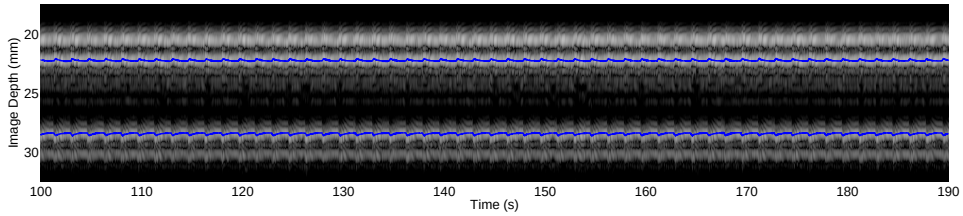

(b) M-mode image

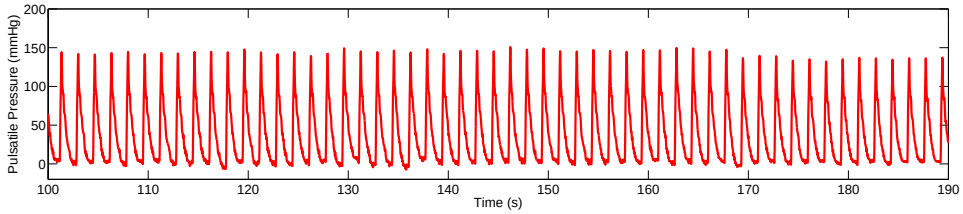

(c) Estimated pressure change waveform

Figure 5-18: (a) Doppler spectrogram, (b) M-mode image, and (c) the estimated pressure waveform with random lateral motions confined up to ±8mm under the plane wave imaging in the flow phantom experiment [81].

cardiac cycles are used to average the PWV estimates, a greater number of cardiac cycles can be used to further reduce the variability in the PWV estimate. On the other hand, a smaller number of cycles should be used if the elasticity change with a shorter time scale, possibly caused by smooth muscle contraction, is to be tracked. Figure 5-18 shows that the pressure waveform can be reliably estimated despite the random lateral motion and misalignment.

Evaluation of IRM estimator

Previous experimental results were obtained from the flow phantom in which no clutter from the adjacent tissues was simulated. The IRM estimator is further tested for accurate distension waveform estimation with low contrast settings.

First, various contrast levels are simulated by adding artificial clutter with various amplitudes and patterns to the high contrast M-mode images acquired using the

focused beam. This synthetic clutter is generated by bandpass filtering random noise with the frequency response similar to the spectral characteristics of the transmitted pulse. The distension waveform obtained from the original high contrast image is considered a reference waveform, and the accuracy of the estimated distension waveform with the artificial clutter is quantified using the NRMSE.

Figure 5-19 shows the performance comparison between the C3M and IRM estimator. Both echo-tracking methods result in accurate distension waveform estimation in high contrasts. In low contrasts, the IRM estimator outperforms the C3M estimator, resulting in the smaller NRMSE. With the help of the pre-calculated compensation, the NRMSE of the IRM estimator further decreases. These results show that by using the IRM estimator, the distension waveform can be more accurately estimated within the NRMSE of 5% when the contrast is as low as 5 dB.

Finally, the feasibility of the IRM estimator is tested in the presence of *in vivo* clutter. Figure 5-20 compares the pulsatile diameter change of the IRM estimator on the M-mode image obtained from the unfocused imaging technique to a reference method. The reference method uses high contrast M-mode images using the focused beam and makes the diameter waveform estimation using the C3M estimator. The width of the bar represents the time duration of the acquired ultrasound images, and the error bar represents beat-to-beat variations. The estimated pulsatile diameter

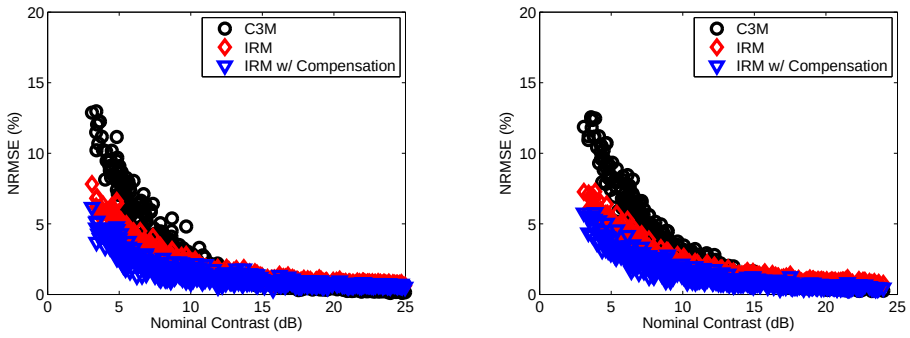

(a) Data Set 1 (b) Data Set 2

Figure 5-19: Accuracy comparison of the estimated diameter waveform between the C3M estimator and the IRM estimator under various simulated clutter environments [81].

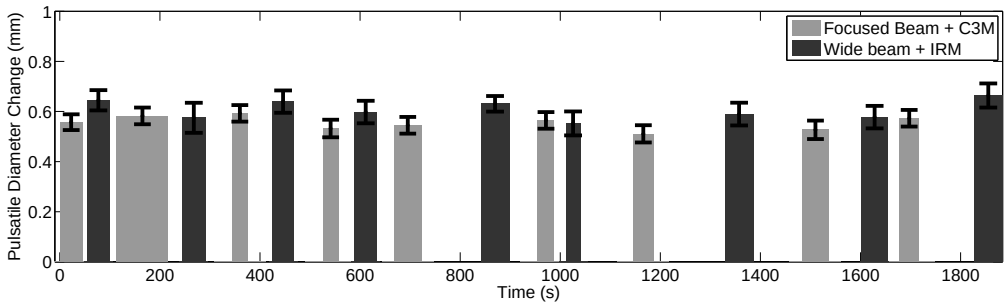

Figure 5-20: Comparison of pulsatile diameter changes in a cardiac cycle of the proposed method using the IRM estimator under plane wave imaging to the reference method using the focused beam and the C3M estimator [81].

change from the proposed method is 0.6 mm on average, which is within a physiological range. The diameter changes between two methods are comparable as can be seen in Figure 5-20.

5.5 Summary

In this chapter, the motion-tolerant unfocused imaging with the widebeam insonation demonstrates that the Doppler ultrasound and M-mode imaging can be performed to acquire physiological parameters such as a flow velocity and diameter waveform with a wide range of lateral offsets. The estimated parameters are validated compared to the other reference measurements, showing insignificant errors. Given that ultrasonography is a viable imaging modality to measure hemodynamics parameters, this demonstration suggests continuous monitoring of hemodynamics for an extended period of time with a low-cost and portable ultrasound scanning device.

The proposed adaptive clutter filtering also helps mitigate the angle estimate error in the vector Doppler technique. Although the improvement is demonstrated while the vector Doppler ultrasound was performed under the uniform insonation, it can also be applicable more generally to cases with the focused beam.

Finally, the proposed IRM estimator is validated as useful in the simulated and real low-contrast environments with synthetic and *in-vivo* clutter, respectively.

Chapter 6

Human Subject Validation during Valsalva Maneuver

This chapter describes a human subject validation study of the designed system under hemodynamic stress. The hemodynamic stress was imposed through the Valsalva maneuver performed by participating subjects. This study was approved by the Committee on the Use of Humans as Experimental Subjects at the Massachusetts Institute of Technology.

This chapter first discusses the background on the physiology of the Valsalva maneuver followed by study protocol details. Study results are presented, and their implications are summarized in the last section. The content of this chapter was published in [70].

6.1 Valsalva Maneuver Physiology

The Valsalva maneuver is a forced expiratory effort against a closed airway, and it is a well-established maneuver to diagnose heart problems or autonomic nervous system deficiencies [85]. During the maneuver, abdominal muscles push the diaphragm upward to build intrathoracic pressure, as shown in Figure 6-1. Quantitatively, if a manometer were used, the maneuver would require airway pressure of approximately 40 mmHg maintained over ten to thirty seconds.

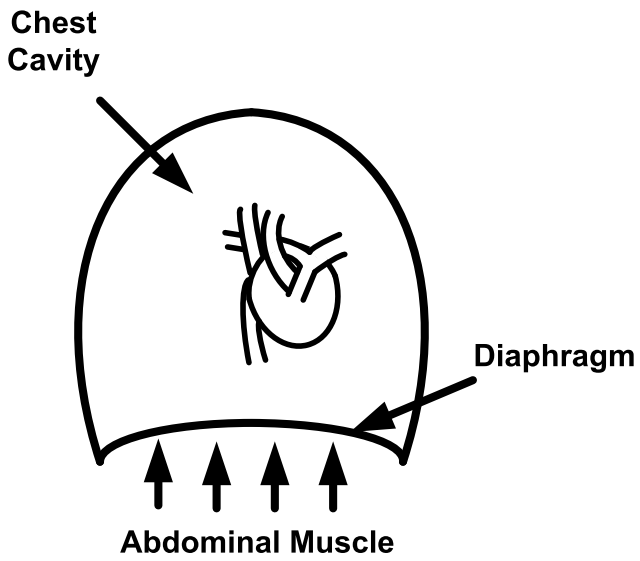

Figure 6-1: Illustration of the intrathoracic pressure changes during the Valsalva maneuver.

One of the clinical use cases of this maneuver is a bubble study during echocardiogram to detect significant opening in the atrial septum, called patent foreman ovale. While a four-chambers view ultrasound image is being obtained, agitated saline water containing microbubbles is injected intravenously, which first appears as bright dots in the right heart in the images. Shortly after the injection, the Valsalva maneuver is performed to increase the pressure in the right heart to open the foreman ovale. Normally, these bubbles are filtered by pulmonary capillaries so that no bubble appears at the left atrium. However, if the foreman ovale is significant, it acts as a shortcut for the bubbles to bypass pulmonary circulation and appear in the left atrium.

In fact, cardiovascular responses during the maneuver are orchestrated by an autonomic nervous control. These responses are primarily triggered by neural signals from baroreceptors, although additional contributions originate from pulmonary stretch receptors and chemoreceptors due to the increase of carbon dioxide [85]. The direct ramifications of the Valsalva maneuver are decreased preload (i.e., left ventricular end diastole volume) and reduced venous return caused by increased resistance in vena cavas. Due to the decrease of cardiac output and eventually blood pressure, baroreflex modulates the heart rate as a compensatory mechanism. In detail, the cardiovascular

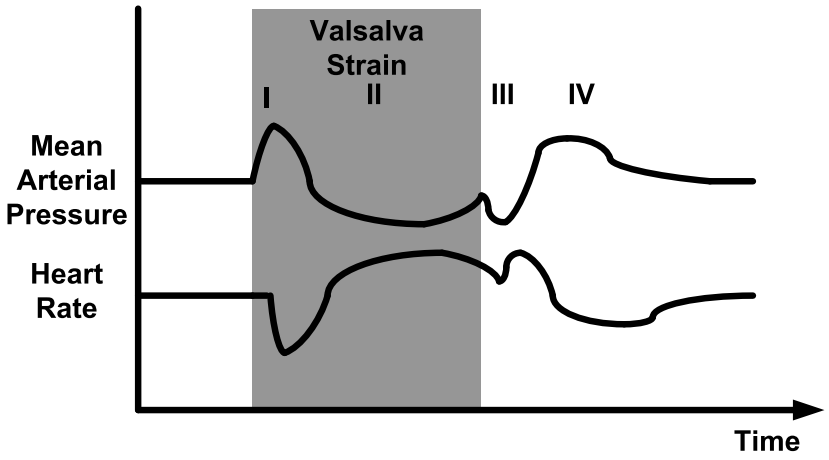

Figure 6-2: Hemodynamics changes during the Valsalva maneuver [85].

responses are divided into four phases: Phases I, II, III, and IV, as shown in Figure 6-2.

Phase I refers to the onset of the Valsalva strain when a slight increase of mean arterial pressure (MAP) occurs due to the sudden increase of intrathoracic pressure. Phase II refers to the continued strain phase. At the early phase II, the decrease of preload causes a reduction of stroke volume (i.e., blood volume ejected per beat), thus dropping pulse pressure (PP). In addition, the impeded venous return due to the occluded vena cavas reduces cardiac output, thereby dropping MAP. As a compensatory mechanism, heart rate increases. As the strain continues, sympathetic activities cause the increase of systemic resistance through vasoconstriction and the heart's contractility to compensate the decreased MAP and PP. Phase III refers to the onset of the strain release when MAP immediately drops because the intrathoracic pressure decreases to normal. Phase IV is defined as a continued recovery phase when cardiac preload returns to normal and reduced venous return is restored. Due to the remaining sympathetic activities, ejection fraction (i.e., the ratio of ejected blood volume to the preload) remains slightly elevated at the beginning [85]. Because of this, PP and MAP may overshoot initially, but they gradually return to the baseline.

In addition to the well-known hemodynamics responses, the morphology change of the ABP waveform was also reported [86]. The measured aortic pressure waveform

showed that the late systolic peak that was present in the control phase gradually became absent during the Valsalva strain. This peak reappeared after releasing the strain. Based on decomposing the ABP waveform into a forward and a backward traveling reflected wave, the reflected wave was shown to be significantly reduced during the Valsalva strain, thus not contributing to augmenting PP at the late systole. A subsequent study suggested that renal artery branching produces non-negligible local reflection, and it was implicated that a transmural pressure drop throughout the intrathoracic aorta helps improve matching at this reflection site, thereby reducing the wave reflection [87].

6.2 Clinical Study Design

The main purpose of the human subject validation during the Valsalva maneuver is to demonstrate that the designed device using the motion-tolerant ultrasound measurement can reliably track the changes of hemodynamics parameters during the Valsalva maneuver. Due to the impeded venous return, an internal jugular vein adjacent to the common carotid artery expands during the Valsalva strain, pushing the artery to a different location. Therefore, motion and misalignment tolerance of ultrasound measurements to reliably acquire a spatial mean flow velocity and a distension waveform during the Valsalva maneuver is essential.

Only healthy human subjects who reported no known diagnosis of cardiovascular diseases participated in this study. The same inclusion and exclusion criteria as specified in the proof-of-concept study discussed in Section 4.3 were applied. The study session consisted of an entry questionnaire, an ultrasound image recording with eight to nine repetitions, and an exit questionnaire. The image recording consisted of 36 seconds of rest to establish the baseline and 25 seconds of the Valsalva maneuver, followed by 43 seconds of recovery.

For the entire duration, the subjects wore an assembled ultrasound probe as shown in Figure 6-3. The probe was primarily secured by two rubber bands wrapped around the neck. Two pads at the end of the bands intended to distribute tension to mit-

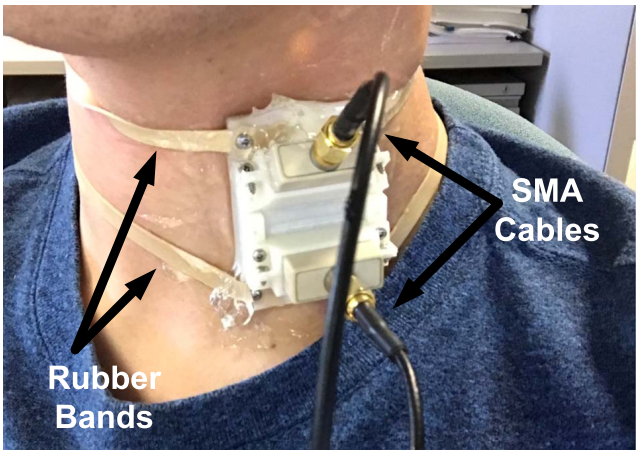

Figure 6-3: An example of an operator-less application of the second probe design secured by two rubber bands [70].

igate discomforts. Occasionally, the probe was manually held by the operator to enhance acoustic coupling and image qualities. In addition, a sphygmomanometer measurement using an automated monitor was conducted in the middle of ultrasound recordings on the left upper arm. The volume clamping type device, a Nexfin hemodynamic monitoring device (Edwards Lifesciences, Irvine, CA, USA), was used to monitor the finger ABP waveform at the contralateral side. Similar signal processing was conducted to analyze the ultrasound images as in Subsection 4.3.2

6.3 Clinical Study Results

Table 6.1: Ages of the subjects and their estimated pulse wave velocities (PWVs) in the Valsalva maneuver study [70].

Subject ID	**Age**	**PWV (m/s)**
S1	27	6.8±0.7
S2	31	7.6±0.8
S3	27	6.3±1.0
S4	24	6.5±1.3
S5	24	7.8±0.9
S6	27	7.3±0.7
S7	31	8.8±0.3

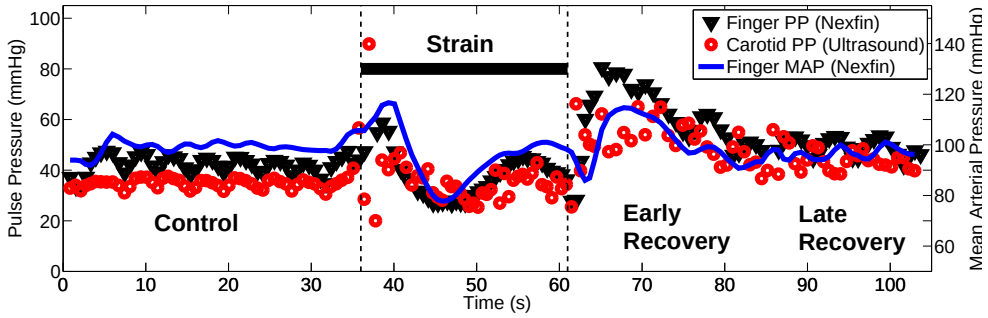

(a) Subject ID: S2

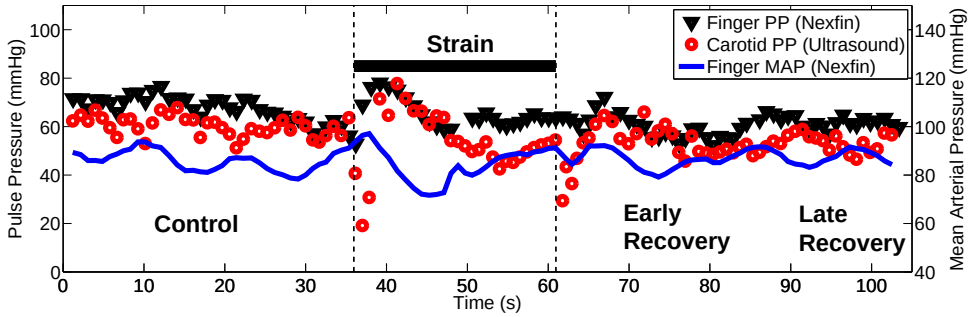

(b) Subject ID: S4

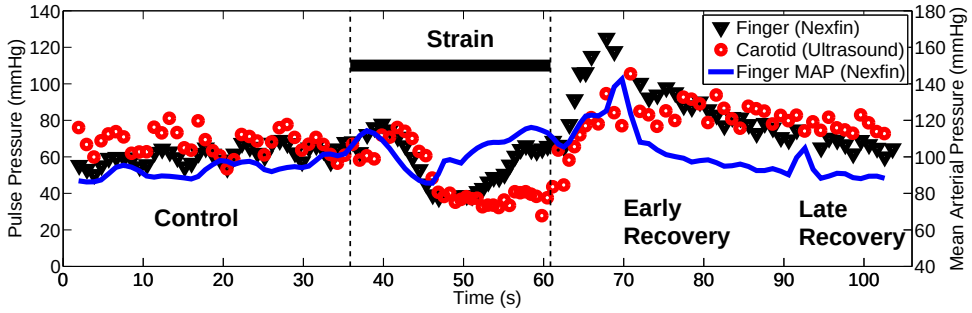

(c) Subject ID: S7

Figure 6-4: Pulse pressure (PP) and mean arterial pressure (MAP) changes during various phases in the Valsalva maneuver. MAPs between the carotid and the finger are assumed to differ by only hydrostatic pressure difference [70].

Table 6.1 summarizes the basic information of the study subjects. Seven healthy human subjects who reported no history of cardiovascular diseases participated in the study session.

Figure 6-4 presents the observed changes of PP among various subjects. During the control, PPs measured at the finger and estimated at the carotid artery remain mostly unchanged or present mild modulation by respiration. Through the baroreflex, the instantaneous pulse rate is also modulated by respiration, as shown in Figure 6-5.

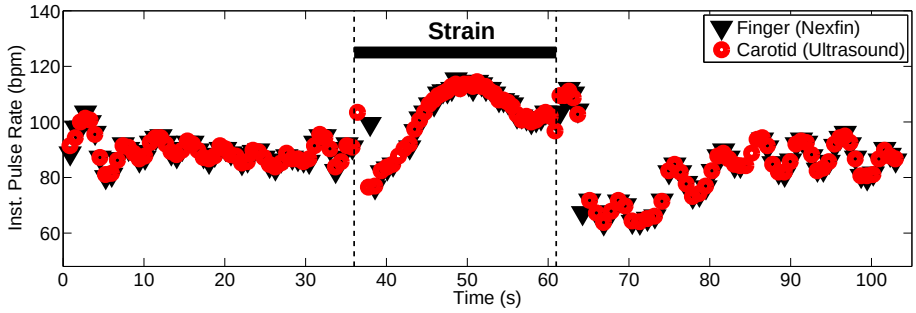

(a) Subject ID: S2

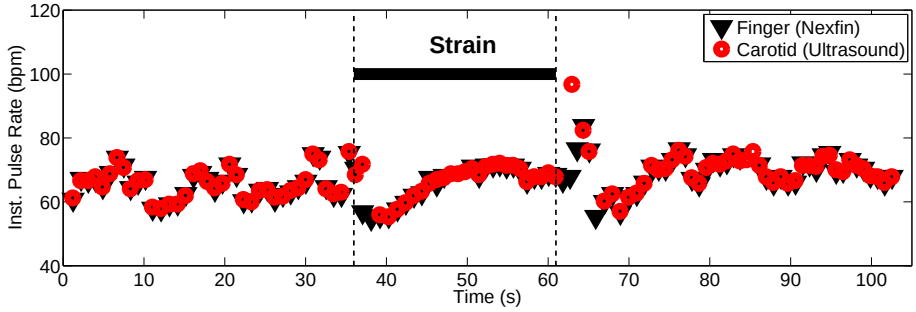

(b) Subject ID: S4

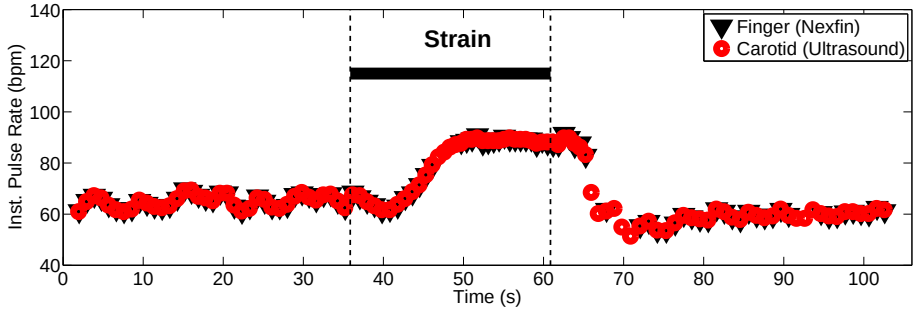

(c) Subject ID: S7

Figure 6-5: Instantaneous pulse rates during various phases in the Valsalva maneuver measured from a distension waveform of the finger and the carotid [70].

At the onset of the Valsalva strain, due to the decreased preload, PP drops, indicating the decrease of stroke volume assuming total arterial compliance remains unchanged. In response, the pulse rate increases to compensate cardiac output. At the late strain phase, the compensatory increase of vasomotor tones and the heart's contractility may occur, partially restoring PP and MAP. A slight discrepancy between the finger and carotid PP is sometimes observed as shown in Figure 6-4(b) and (c).

The elevated sympathetic activities continue during the early recovery phase. However, due to the restored preload, stroke volume and PP overshoot, as evidenced in the finger PP. However, the estimated carotid PP does not necessarily track such a trend. In fact, the aortic PP also presented an overshoot, as reported in prior art [88]. On one hand, this discrepancy may be attributed to the limitation of the echo-tracking to reliably produce a distension waveform which can be challenging if the movement of underlying structure is significant between different phases in the Valsalva maneuver. On the other hand, the discrepancy may be attributed to the different degrees of PP augmentation between at the finger and the carotid under the vasoconstriction. The augmentation due to vasoconstriction is much more dramatic at the peripheral site than at the central site because of the difference between time alignment of a forward traveling and a reflected pulse wave for each site. Due to the overshoot of MAP and PP, the pulse rate presents an undershoot. During the late recovery, both the pulse rate and blood pressures are stabilized to the baseline, and the discrepancy between the two PPs gradually decreases.

The morphology of the ABP waveform also changes during the Valsalva maneuver, as reported in prior research [86,87]. The representative estimated ABP waveforms in different phases are presented in Figure 6-6. These waveforms are produced by taking ensemble averages of the estimated waveform synchronized to the identified systolic onset of each heart beat. During the strain phase, a dicrotic notch (i.e., a small dip in the pressure and flow waveforms caused by aortic valve closure) is significantly depressed, which is quantified by a parameter, referred to here as a depression index. The depression index is defined by the ratio of relative heights of the dicrotic notch to the peak during the diastole as presented in Figure 6-6. The waveform during the early recovery phase presents a pronounced late systole peak, while the waveforms during the control and the late recovery do not usually present such a pronounced peak.

In fact, the depression of the dicrotic notch implicated a reduction of the reflected pulse wave in the aorta [87]. The pressure at the aortic arch is seen as a source of pressure which generates a forward traveling pulse wave at the inlet of the common

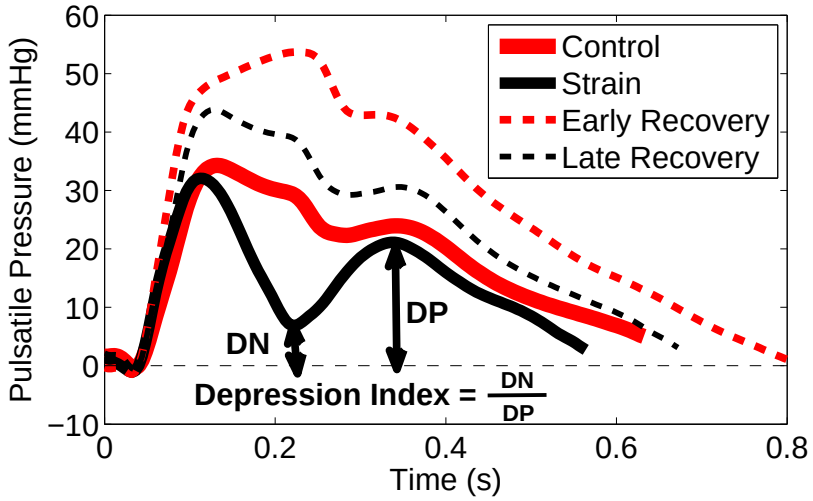

Figure 6-6: Ensemble averaged estimated ABP waveform at the carotid in various phases in the Valsalva maneuver. The depression index is defined as relative heights of the dicrotic notch and a peak during diastole from the baseline [70].

carotid artery. The previous study showed that during the Valsalva maneuver, the local reflection at the renal branching in the thoracic aorta was reduced. Usually, the reflected pressure wave obscures a sharp dip in the forward wave. During the Valsalva maneuver, the reduction of the wave reflection unveils this sharp dip, resulting in the depression of the dicrotic notch in the estimated ABP waveform. On the contrary, the stronger reflected wave not only almost obscures the dicrotic notch but also creates significant PP augmentation in the late systole at the aortic arch, which was typically evidenced in the carotid ABP waveform, especially during the early recovery. Therefore, the pronounced late systolic peak may imply the increase of pulse reflection in general, possibly rooted from the vasoconstriction.

Figures 6-4 and 6-5 show the baroreflex in response to the change of ABP. It is noteworthy that the baroreceptor responds to both static and pulsatile stress although Figure 6-7 only plots the instantaneous pulse rate with the measured PP at the finger and the estimated carotid PP at the carotid artery. Due to the delay in the ABP control feedback loop, a delay is added that results in the highest correlation. The figures show strong negative correlations between the PPs and the pulse rate as expected.

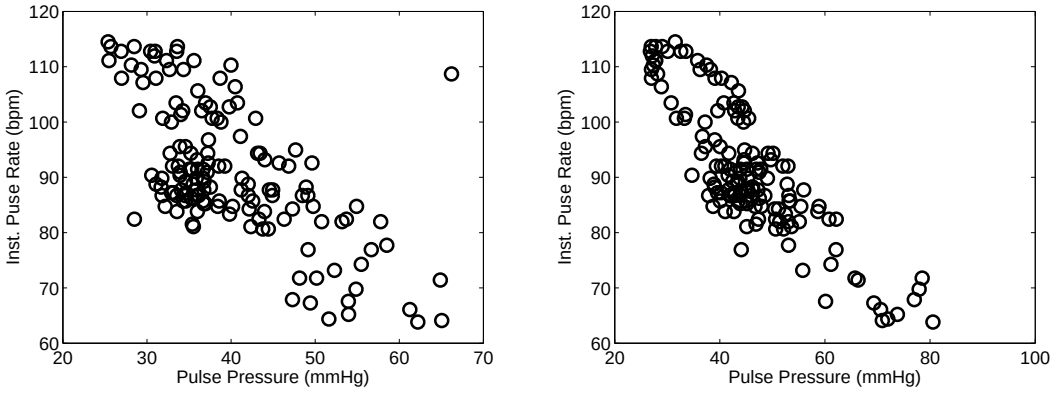

(a) Carotid (b) Finger

Figure 6-7: Baroreceptor sensitivity curve displaying the instantaneous pulse rate with PP (a) estimated at the carotid and (b) measured at the finger. A delay, determined to result in the highest correlation, is added to account for the delay in the cardiovascular control loop.

Figure 6-8 shows the comparison of PP between the estimation at the carotid artery to the other measurements including an automated cuff measurement and the finger waveform during the control phase. The PP estimation error in comparison to the finger waveform among all qualified image acquisitions is 3.98±15.59 mmHg, which is calculated from individual ultrasound recordings, not from intra-subject averaged values.

The proposed method shows higher standard deviations in the PP estimation than the other measurements. This variation is mainly attributed to the variation of the PWV estimation, and there are mainly two reasons: First, the local PWV estimation has variation due to stochastic nature of the Doppler signal. Since the spatial mean flow velocity waveform presents noise-like variation, the local PWV estimation based on the flow-area method displays the variation. An independent experiment showed that individual PWV estimates have the standard deviation of roughly 20% of the average of the PWV estimates. As the number of cardiac cycles to calculate the mean PWV increases, the standard deviation of the average of PWV, which is used to represent the vessel elasticity for the duration of the entire ultrasound image, decreases. Second, the ultrasound measurements can have minor dependency on the

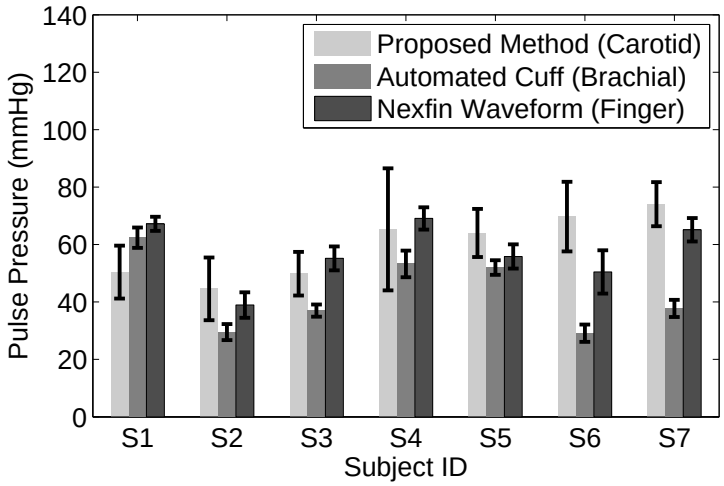

Figure 6-8: Pulse pressure (PP) comparison between the estimation at the carotid to an automated cuff measurement and a finger waveform during the stable control phase. Ultrasound images with a contrast more than 8 dB and the Doppler signal-to-noise ratio (SNR) more than 8 dB are included.

orientation of the probe relative to the target vessel because of the directionality of the ultrasound beam while the other measurements are inherently not. As a result, different probe alignments, such as a twist angle of the probe, can cause the variations in the measured physiological waveforms especially given that the accurate alignment is only visually inspected from the real-time ultrasound images, not highly sensitive.

On the contrary, the cuff placement for the brachial and finger ABP measurement remained unchanged for the duration of the session. Therefore, if the longer duration of the image were used (e.g., more than 30 s for the initial control phase before this Valsalva maneuver), the variability would decrease. In addition, more consistent placement of the probe relative to the vessel would be possible through automated image quality evaluation algorithms.

The continuous monitoring capability of the change of PP is quantified by correlation coefficients between the estimated carotid PP and the finger PP for all four phases. Figure 6-9 shows the statistics of the correlation coefficients among the seven subjects. In most cases, positive correlations are obtained while some subjects, such as S3, S4, and S6, result in small values. These low values are attributed to the sub-

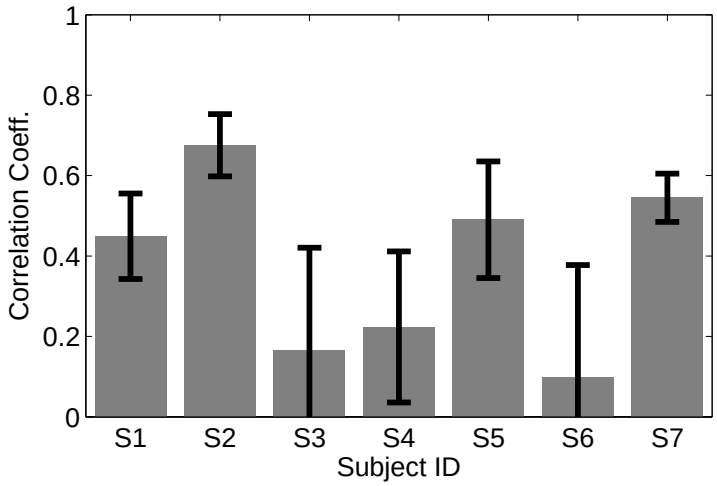

Figure 6-9: Correlation coefficients between the estimated carotid PP and the measured finger PP over all phases of the Valsalva maneuver [70].

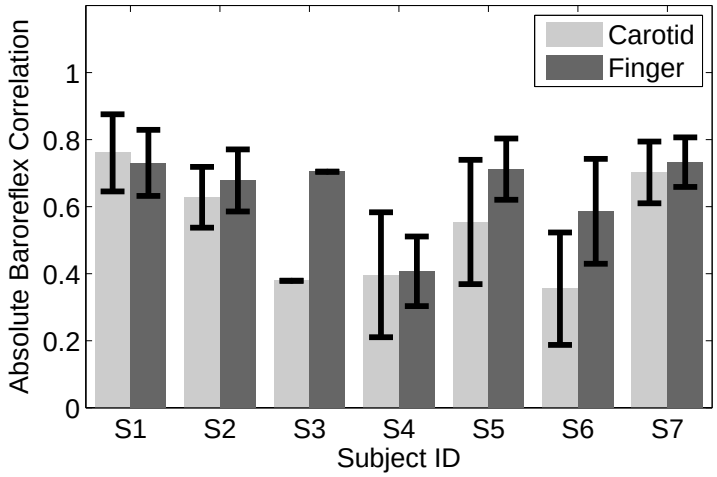

Figure 6-10: Baroreceptor sensitivity correlation coefficients among the seven subjects.

jects being unable to create a significant and correct Valsalva strain, such that only small changes of PP are observed. The correlation coefficient is more prone to being penalized when the measured variable changes a little. It is noteworthy that S3 and S6 are female subjects who may have been unable to create sufficient increase of intrathoracic pressure. In addition, the discrepancies in the late strain phase and early recovery phase certainly hinder perfect correlation. Nevertheless, the estimated PP

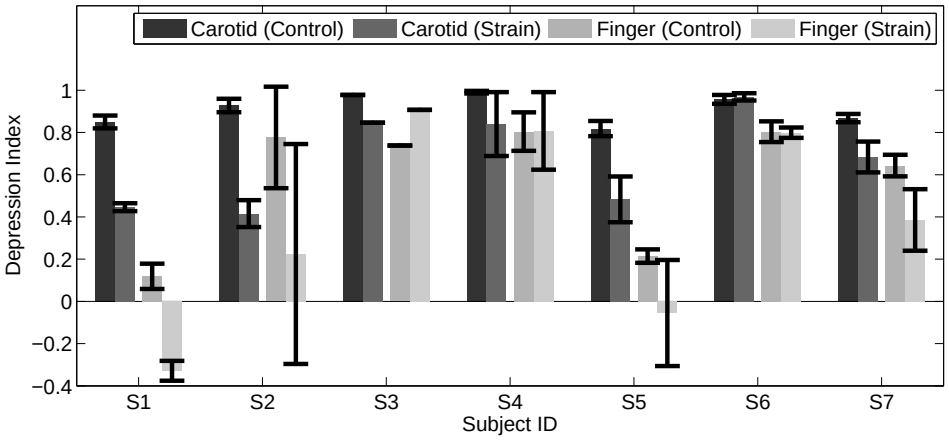

Figure 6-11: Depression index comparison between the control phase and the strain phase among the seven subjects [70].

is shown to correlate to the PP at the finger, demonstrating PP tracking capability of the designed device during the entire Valsalva maneuver.

While the correlation coefficients attempt to quantify the direct correlation between the PPs, the correlation to the instantaneous pulse rate can also indirectly support that the estimation tracks the change of PP which naturally triggers the change of the pulse rate. Given that the baroreflex is dependent on both static (MAP) and pulsatile (PP) stress, a two variables linear regression model is assumed to calculate baroreflex sensitivity correlation coefficients. Figure 6-10 presents the absolute value of the baroreflex correlation coefficients, which display high values. For subjects S3, S4, and S6, their coefficients are relatively lower than the others due to the suspected lower degree of the Valsalva strain.

Finally, the morphology change of the ABP waveform quantified by the depression index is presented in Figure 6-11. Except for subjects S3, S4, and S6, the depression of the dicrotic notch is quantified as statistically significant during the strain phase in the carotid waveform, implicating a clear change of the ABP waveform shape. This figure may also support that the degree of the Valsalva strain created by subjects S3, S4, and S6 is lower than the others.

From this Valsalva maneuver study, it is demonstrated that the proposed proto-

type device is capable of tracking hemodynamics changes during the Valsalva maneuver, such as the change of PP and the morphology of the ABP waveform.

6.4 Summary

In this chapter, the Valsalva maneuver study and its results are detailed to demonstrate the feasibility of the designed prototype in estimating the ABP waveform under hemodynamic stress. Thanks to the motion-tolerant ultrasound measurements described in Chapter 5, the spatial mean flow velocity and arterial pulsation can be reliably monitored even with possible displacements of the carotid artery due to the expansion of the adjacent jugular vein. In addition, the estimated ABP waveform shows qualitatively the expected hemodynamics changes which are also evidenced by the ABP waveform continuously monitored at the finger, such as the reduced PP as well as the morphology changes. Alongside the initial proof-of-concept study in Chapter 4, this study shows that this non-invasive ABP waveform estimation device using ultrasound can be useful for tracking the hemodynamics changes.

Chapter 7

Human Subject Validation with Comparison to Arterial Line

This chapter describes a human subject validation study wherein a designed prototype system was evaluated in comparison to the gold standard arterial-line (A-line) arterial blood pressure (ABP) waveform measurement at the radial artery. This clinical study, named the Non-invasive Evaluation of an arterial pressure WavEform uSing ulTrasound (NEWEST) trial, was approved by the institutional review board at the Boston Medical Center, and the Committee on the Use of Humans as Experimental Subjects at the Massachusetts Institute of Technology ceded its right to review.

This chapter first introduces techniques to estimate a central ABP waveform from a peripheral ABP waveform. Since the designed system estimates the ABP waveform at the carotid, measurement site mismatch is an expected source for discrepancy. In that sense, these techniques can be useful in largely eliminating this concern as a carotid pulse contour is similar to an aortic contour [57]. The study design and results are presented herein, followed by the summary.

7.1 Transfer Function Techniques

As mentioned in Chapter 1, several studies showed that the central ABP is more closely associated with the cardiovascular diseases [10, 11]. Unfortunately, cardiac

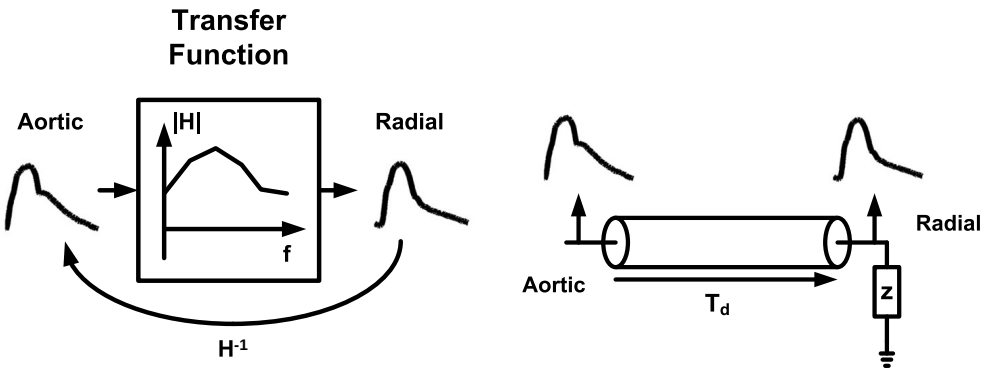

(a) Generalized transfer function (b) Adaptive transfer function

Figure 7-1: Illustration of transfer function techniques to translate a peripheral (radial) ABP waveform to a central (aortic) waveform.

catheterization including a coronary arteriogram is the only method available to acquire central ABP in clinical settings, and the procedure is not suited for continuous monitoring. Although the A-line is considered the gold standard for a full waveform, it provides a radial ABP trace. Given the shape of the ABP waveform progressively changes along an artery tree, as discussed in Subsection 2.2.2, the radial trace, although useful for the purpose of continuous monitoring, may have limited clinical significance in prognostic and diagnostic applications.

Because of these progressive changes, several studies have introduced models to estimate the central ABP from the peripheral ABP waveform from the A-line or non-invasive methods, including vascular unloading (i.e., volume clamping method) and arterial tonometry [12–14, 89, 90]. These efforts are mainly categorized into two groups: generalized transfer function and adaptive transfer function.

7.1.1 Generalized Transfer Function

A generalized transfer function (GTF) approach produces an arbitrary transfer function which, indeed, translates the central waveform to the peripheral waveform [12, 91]. This transfer function was calculated from a direct comparison of spectral contents of simultaneously acquired central and peripheral ABP waveforms over numerous patients [12, 89, 90].

Usually, the magnitude response of this transfer function typically presents a peak of around 4 to 5 Hz [91]. A high frequency content in the central ABP waveform is accentuated through this transfer function to create a peripheral waveform with a sharper systolic peak. Once the transfer function is constructed, the inverse of the transfer function is used to translate the peripheral to central waveform as shown in Figure 7-1(a). In fact, the inverse of the transfer function is not causal because the peripheral waveform is delayed by a pulse transit time. To implement this, a filter is constructed to have a frequency response corresponding to the inverse of the established transfer function in addition to an extra group delay to make it causal. Then, the peripheral ABP waveform is filtered by this filter to estimate a delayed version of the central waveform. The delayed version is subsequently advanced by the added group delay to correctly estimate the central ABP waveform.

Although the GTF approach basically rewinds the progressive amplification of pulse pressure, it is often criticized due to neglecting person-specific variations in the population-averaged transfer function.

7.1.2 Adaptive Transfer Function

Because of this criticism, an adaptive transfer function (ATF) technique was introduced to incorporate variations between individual persons [13,14]. This technique assumes an arterial tube-load model that encapsulates pulse wave propagation and wave reflection at the distal beds.

The ATF technique is mainly characterized by a reflection coefficient at the terminal load and a pulse transit time between the central and the peripheral sites. Figure 7-1(b) shows the tube-load model with an elastic tube with negligible resistance terminated by a terminal load impedance. In this model, a peripheral (e.g., radial artery) ABP waveform originates from the summation of a forward and a reflected pressure wave without a misalignment of time. On the contrary, the central waveform originates from the summation of the two traveling waves but with an appropriate pulse transit time (T_d) advance and delay, respectively. The forward and backward traveling waves are mathematically acquired by decomposing the peripheral ABP waveform

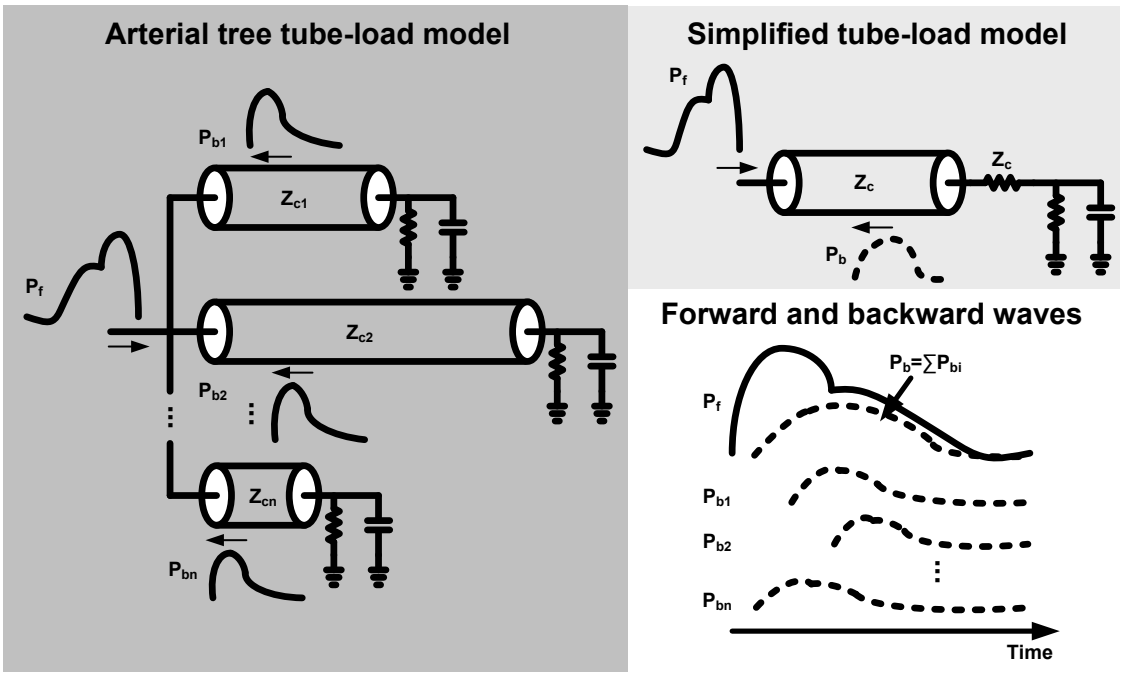

Figure 7-2: Illustration of an arterial tube-load model and a simplified single tube-load model for the whole arterial system assumed in the adaptive transfer function approach.

based on the reflection coefficient (Γ). This intuition can be formulated as:

$$\begin{aligned} P_{\text{central}} &= P_f(t+T_d) + P_b(t-T_d) & Q_{\text{central}} &= Q_f(t+T_d) + Q_b(t-T_d) \\ P_{\text{peripheral}} &= P_f(t) + P_b(t) & Q_{\text{peripheral}} &= Q_f(t) + Q_b(t) \\ \Gamma &= \frac{P_b(f)}{P_f(f)} = -\frac{Q_b(f)}{Q_f(f)} = |\frac{\Gamma_0}{1+j\frac{f}{f_c}}| & Z_C &= \frac{P_f(t)}{Q_f(t)} = -\frac{P_b(t)}{Q_b(t)} \end{aligned} \tag{7.1}$$

where P_f and P_b are the forward and backward traveling pressure waves, respectively; Q_f and Q_b are the forward and backward traveling flow waves, respectively; Γ_0 and f_c are an asymptotic reflection coefficient at DC, and a lowpass corner frequency, respectively; and Z_C is the characteristic impedance. Γ_0, f_c, and T_d are the parameters that characterize the estimation process. In prior research, the reflection coefficient was assumed to present one-pole characteristics [13] to roughly match the observed frequency dependency in the global reflection coefficient [54]. This frequency depen-

dency can be understood in two-fold: First, the load impedance presents a minor capacitive component due to compliance at the arterioles, as shown in load impedances of individual branches in Figure 7-2. Second, the reflected backward wave seen at the central site displays dispersion due to the summation of individual reflected waves with different round trip times from different terminal branches. Therefore, when a simplified single tube-load model, assumed in the ATF approach, is used, the terminal load is modeled with a three element windkessel model to have the reflection coefficient with a single pole characteristic in Figure 7-2.

However, the direct measurement of these parameters is challenging. Instead, these parameters are estimated based on several assumptions often justified by well-established observations. For example, the estimated aortic flow waveform (Q_{central}) should present the lowest variation during the diastole because no significant flow occurs after the aortic valve closure. Based on this criterion, a frequency dependent reflection coefficient can be determined [13]. In addition, the estimated central ABP waveform should present an exponential decay during the diastole, as predicted by the two-element Windkessel model discussed in Subsection 2.2.1, when most of the pulse wave dies out. Based on this criterion, the pulse transit time can be determined [14]. Once these model parameters are identified, the adaptive transfer function can be constructed as follows:

$$\begin{aligned} P_{\text{central}}(f) &= \frac{e^{j2\pi f T_d} + \Gamma e^{-j2\pi f T_d}}{1+\Gamma} P_{\text{peripheral}}(f) \\ Q_{\text{central}}(f) &= \frac{e^{j2\pi f T_d} - \Gamma e^{-j2\pi f T_d}}{Z_C(1+\Gamma)} P_{\text{peripheral}}(f) \end{aligned} \tag{7.2}$$

The ATF technique allows for the estimation of person-specific parameters. However, the transfer function only has the specific form as shown in Equation 7.2, having a lower degree of freedom than the GTF approach. In addition, this model drastically simplifies an entire arterial tree into the single elastic tube with the terminal load.

The mathematically estimated central ABP waveforms using the GTF and ATF applied on the radial ABP waveform are also compared to the estimated ABP wave-

form at the carotid artery using ultrasound in the study results.

7.2 Clinical Study Design

The main purpose of the NEWEST study is to demonstrate the viability of the proposed ABP waveform estimation in comparison to the A-line measurement, conducted in intensive care settings. The study was conducted in collaboration to the team at the Boston Medical Center.

Prior to the study session, the informed consent was obtained from prospective subjects. The inclusion criteria were an age of older than 18 years and patients presenting with an arterial line in intensive care units. Furthermore, only patients who were able to consent in English were included. Several exclusion criteria were specified such as pregnancy, inability to access the neck or upper arms, inability to lie down, and known issues with medical ultrasound, and/or hemodynamic instability as evaluated by the attending physician.

The study session began with the acquisition of ultrasound images on the left carotid artery using a commercial scanner (CX-50, Philips Healthcare, Andover, MA, USA) by a study team clinician. A vascular probe (L12-5) was used to image the carotid artery while the scanner was configured in carotid vascular preset. One long-axis and two short-axis (proximal and distal sites) B-mode images were acquired in addition to the spectral Doppler image for four images in total. The A-line trace at the radial artery was continuously monitored and recorded for the entire duration of the session by a data acquisition cart. Following the acquisition using a commercial scanner, the designed investigational device acquired ultrasound images after the

Table 7.1: Ages of the subjects, estimated pulse wave velocities (PWVs), and the number of eligible beats for data analysis in NEWEST trial.

Subject ID	**Age**	**PWV (m/s)**	**Number of Beats**
S1	68	4.8±0.3	185
S2	66	4.5±0.6	55

clinician maneuvered the probe to align. The total duration of the study session was limited to 45 minutes.

7.3 Clinical Study Results

Table 7.1 summarizes the demographics, pulse wave velocities estimated, and the number of eligible beats for data analysis over the subjects. Two subjects who underwent an open heart surgery while presenting the A-line participated in this study.

7.3.1 Ultrasound Images and Physiological Waveforms

Ultrasound images captured by the commercial scanner give basic information about anatomical structures of the subject and possible plaque formation evidenced by severely turbulent flow. The images were not used for actively guiding the placement of the probe from the designed investigational device. Figure 7-3 shows example images from the subject S1. This figure shows that the carotid blood flow has no

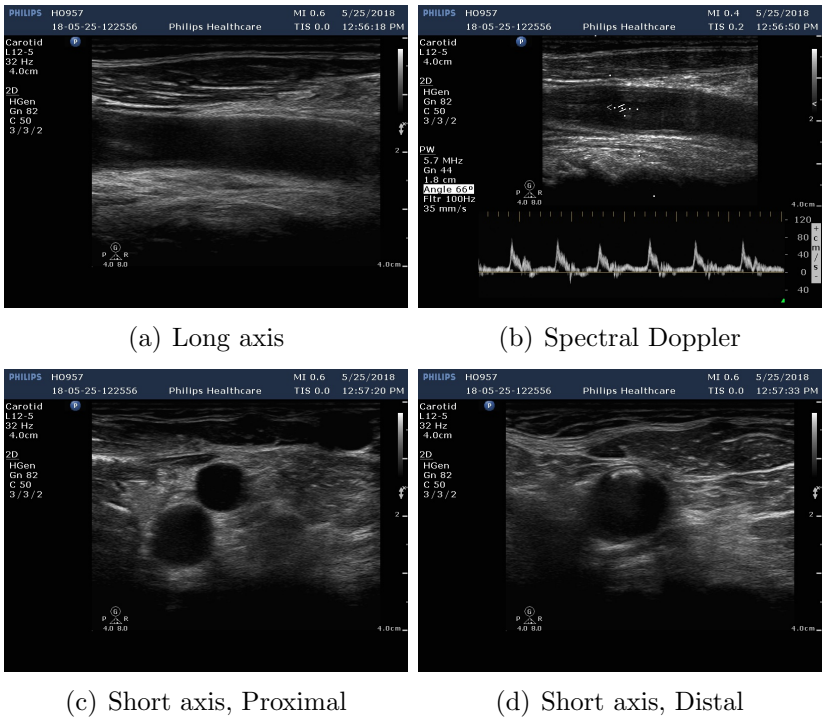

(a) Long axis (b) Spectral Doppler

(c) Short axis, Proximal (d) Short axis, Distal

Figure 7-3: Ultrasound images captured by a commercial ultrasound scanner.

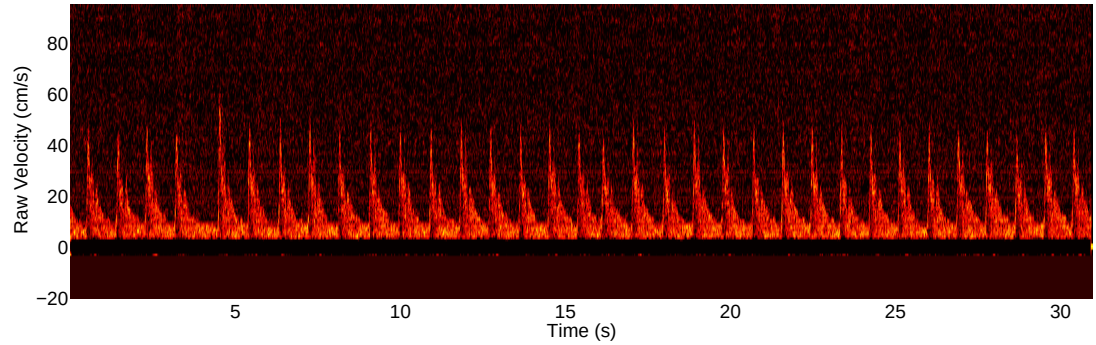

(a) Doppler Spectrogram, CH1 - Insonating nominally at 50°

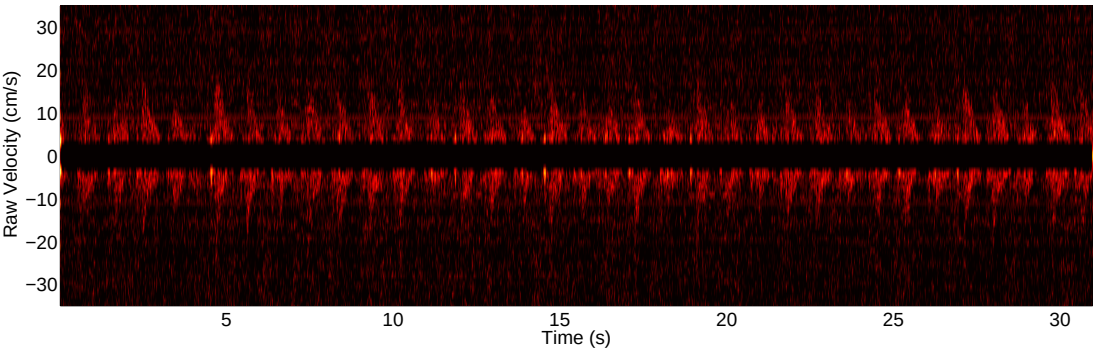

(b) Doppler Spectrogram, CH2 - Insonating nominally at 90°

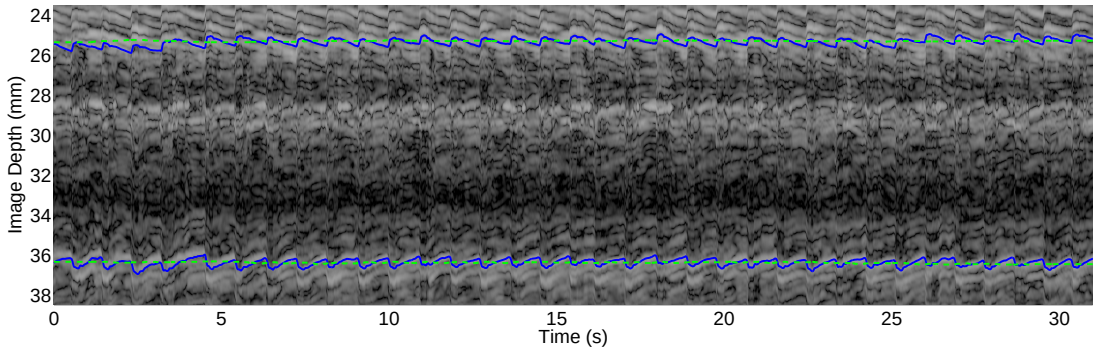

(c) M-mode image

Figure 7-4: Ultrasound images captured by the investigational prototype device shown in Figure 3-15. The Doppler signals are not angle corrected. The Doppler signal from CH1 shows a strong flow signal. The Doppler signal from CH2 presents symmetric spectrum around zero frequency due to its perpendicular insonation. The green traces in the M-mode image indicates the locations of the echo-tracking windows where the blue traces are resulting displacement traces of the wall movements.

turbulent flow although the short axis view at the distal site, close to the bifurcation, may indicate mild plaque formation. The inner diameter of this subject's carotid artery is estimated to be roughly 10 mm to 11 mm.

Typical ultrasound images acquired using the designed prototype system are shown in Figure 7-4. Some artifacts in the Doppler spectrogram were pre-processed, such as horizontal lines caused by an epicardial wire temporarily placed inside the post-operative subjects. In addition, the signals in the negative frequency band were removed as only the arterial flow matters. Other than these, similar signal processing is conducted as in Subsection 4.3.2

The Doppler spectrogram before the Doppler angle correction from channel 1 (CH1) in the second probe design, discussed in Section 3.1, clearly displays pulsation of blood flow. Although a heart beat looks fairly regular in Figure 7-4, the other subject's data often present ectopic beats and occasionally prolonged cardiac cycles. Figure 7-4(b) shows the Doppler intensity is symmetric around zero frequency since the transducer for CH2 perpendicularly insonates the target vessel. By combining these two Doppler signals, the Doppler angle is estimated through the vector Doppler technique to ensure proper angle correction in the calculated flow velocity waveform. The M-mode clearly shows pulsation of the carotid artery while clutter is visible due to the nature of wide-beam insonation. After identifying the depths for the anterior and posterior walls (green traces), the echo-tracking windows are defined to finely track the movement of the walls (blue traces), as shown in Figure 7-4(c).

With the angle correction, the spatial mean flow velocity and the diameter waveform are calculated as shown in Figure 7-5. The diameter waveform presents a roughly 10% pulsatile diameter change to the baseline. The flow velocity waveform displays a sharp systolic upstroke. Systolic onsets are identified based on the maximum acceleration point in every cardiac cycle, which is the same criterion as that which was used in the previous clinical studies.

7.3.2 Parameter Estimation in Transfer Function Techniques

For the GTF approach, the transfer function is adopted from published prior research [91]. For the ATF approach, the optimization processes are conducted to determine the reflection coefficient and the pulse transit time. A grid search is conducted on the DC reflection coefficient (Γ_0) and the pole (f_c) of the frequency dependent re-

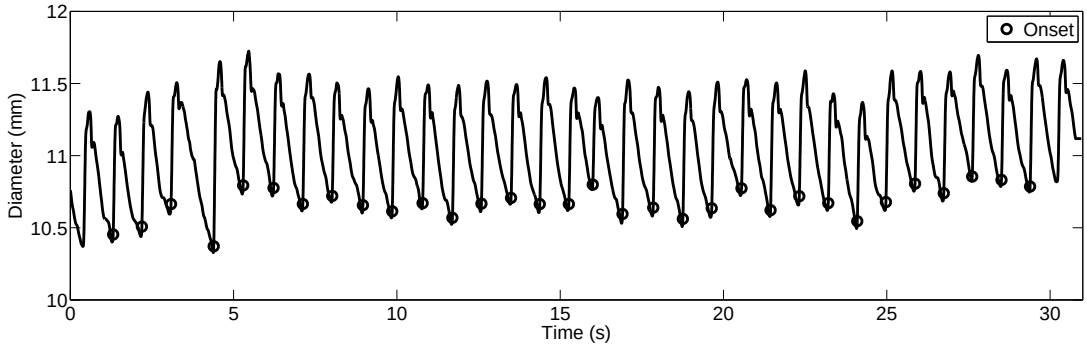

(a) Spatial mean flow velocity

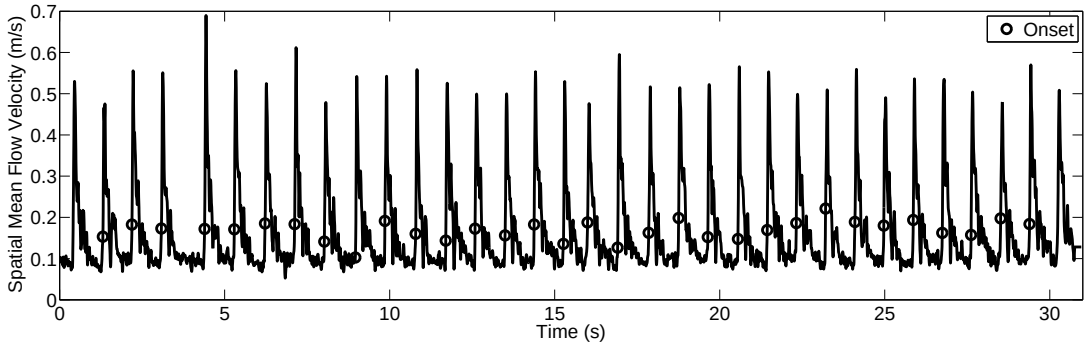

(b) Diameter waveform

Figure 7-5: Estimated spatial mean flow velocity and distension waveforms from the raw ultrasound images acquired by the designed prototype system.

flection coefficient (Γ). A pair of Γ_0 and f_c values that results in the lowest diastolic flow waveform variation are selected. In addition, the pulse transit time that results in the lowest root mean square deviation from the exponential fit on the estimated central ABP waveform during diastole is selected.

7.3.3 Waveform Comparison

The estimated ABP waveform using the proposed method in this thesis is directly compared to both the A-line trace at the radial artery and the estimated central ABP waveforms using the transfer function techniques (i.e., GTF and ATF). Delays are added appropriately to synchronize all waveforms at the beat-to-beat level. The first four beats are used for calibration purposes to match mean arterial pressure (MAP) between all waveforms, taking out hydrostatic pressure difference, as MAP remains

constant over major arteries due to negligible flow resistance [33, 76].

Across all subjects, the A-line traces present a much sharper systolic peak than the estimated carotid waveform using ultrasound as presented in Figure 7-6. This is mainly due to the pulse pressure (PP) amplification, as expected. The estimated central ABP waveforms from the GTF and ATF, present more rounded systolic peaks, and their PPs are comparable to PP of the estimated carotid ABP waveform using ultrasound as presented in Figure 7-7. Nevertheless, the amplitudes of the carotid ABP waveform are, in general, smaller than those of other waveforms.

Root mean square error (RMSE) and a correlation coefficient are used to quantify the overall agreement between the estimated carotid waveform and the other waveforms. Figure 7-8(a) shows that the RMSE is higher when compared to the A-line where the RMSEs are lower versus the estimated central ABP waveforms using the

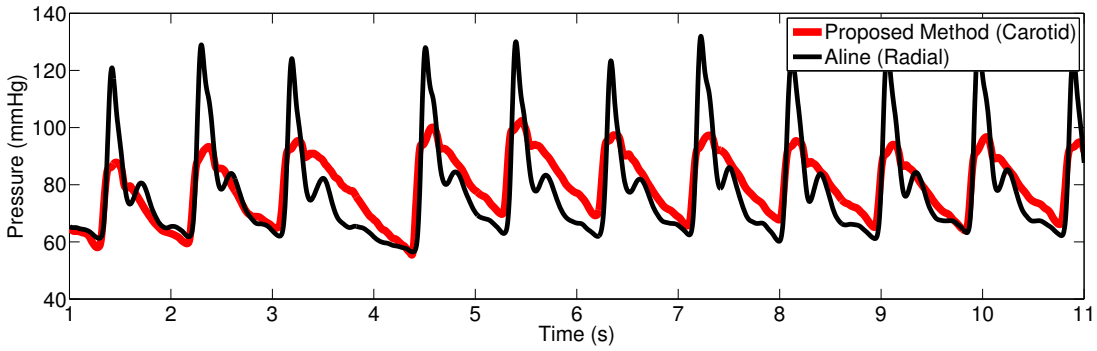

(a) Subject ID: S1

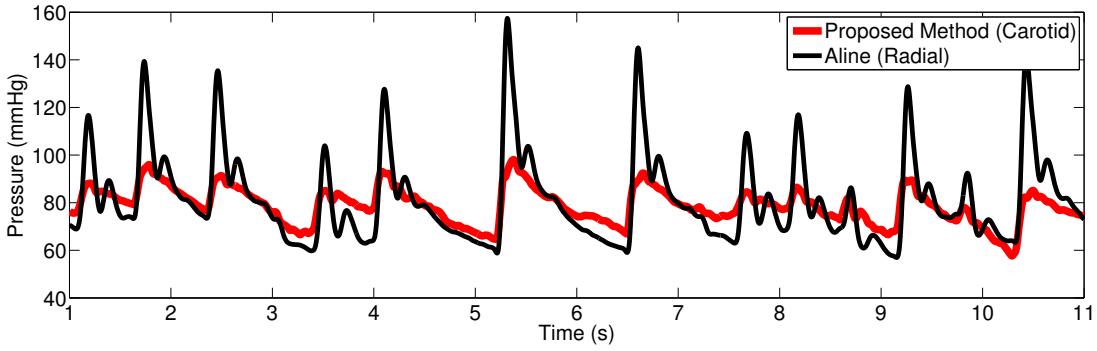

(b) Subject ID: S2

Figure 7-6: Comparisons of the estimated carotid ABP waveform using the proposed method to the A-line trace at the radial artery.

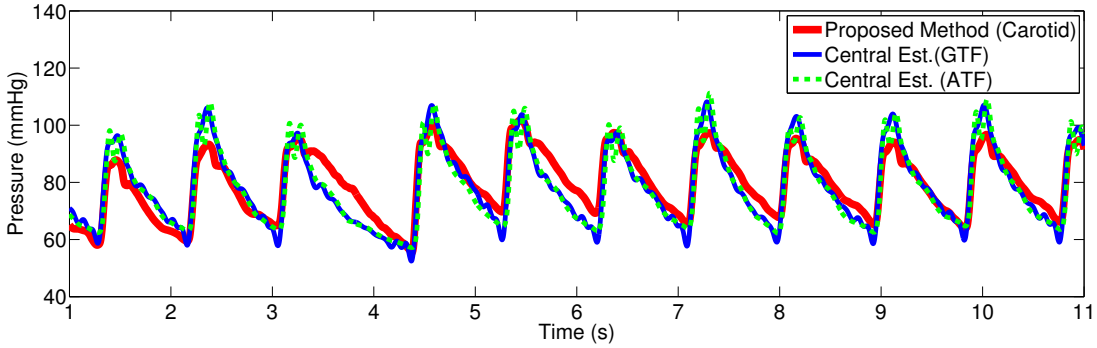

(a) Subject ID: S1

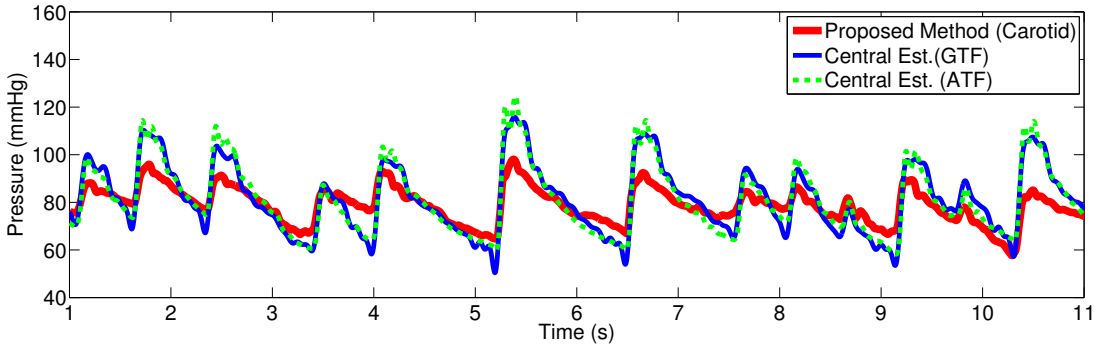

(b) Subject ID: S2

Figure 7-7: Comparisons of the estimated carotid ABP waveform using the proposed method to the estimated central waveforms using a generalized transfer function (GTF) and an adaptive transfer function (ATF).

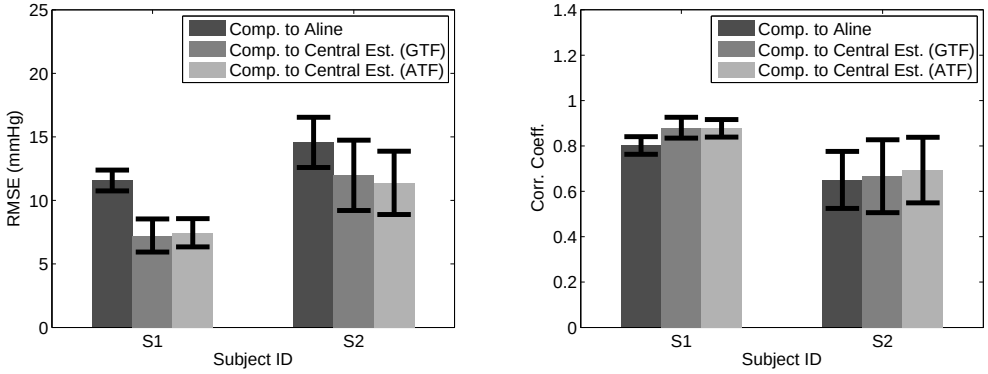

(a) Root mean square error

(b) Correlation coefficient

Figure 7-8: Overall agreement of the estimated carotid ABP waveform using ultrasound to the radial trace (A-line) and the estimated central waveforms from the GTF and ATF techniques, quantified by RMSE and correlation coefficients.

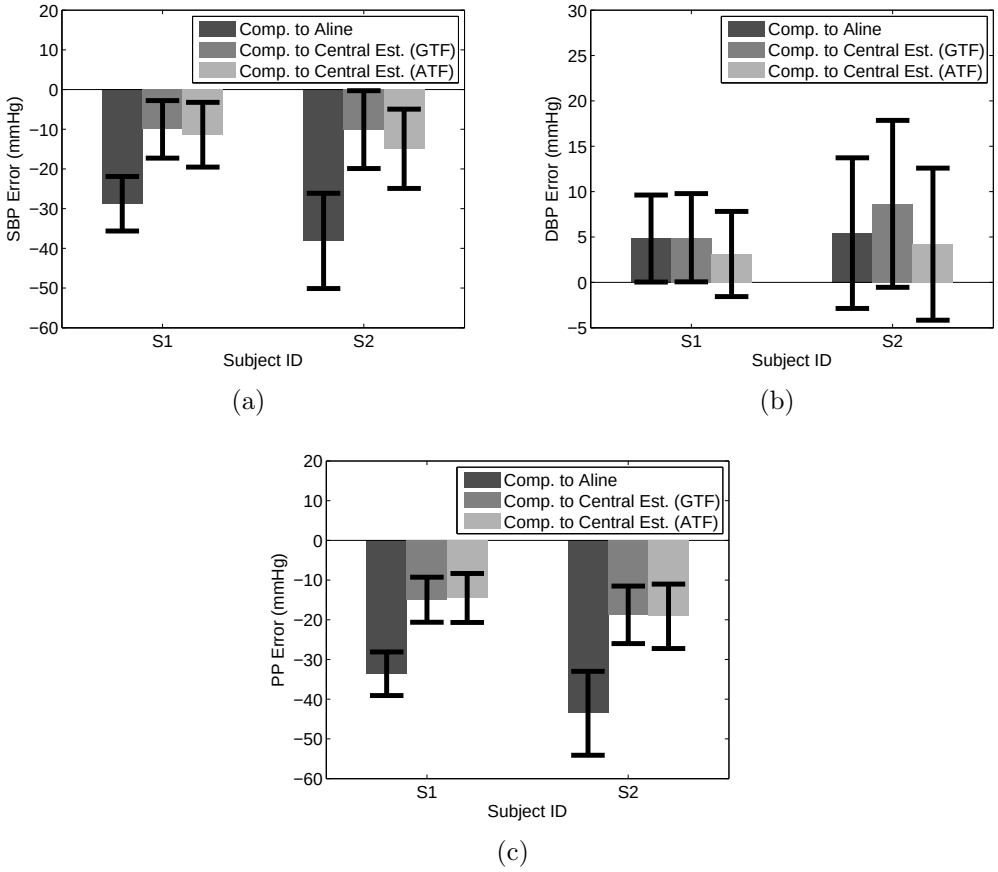

Figure 7-9: Statistics of systolic, diastolic, and pulse pressure estimation performance of the proposed method in comparison to the radial ABP (A-line) and the estimated central ABP from the GTF and ATF techniques

GTF and ATF. Figure 7-8(b) shows that the correlation coefficient usually increases when compared to the estimated central waveforms using the GTF and ATF.

The blood pressure estimation errors, presented in Figure 7-9(a) and (b), imply that the proposed method tested in this study underestimates systolic blood pressure and slightly overestimates diastolic blood pressure. As a result, the PP is underestimated in comparison to the other references. It is worth mentioning that, although the A-line trace is more accurate than the other non-invasive methods, such as arterial tonometry or the volume clamping method, it measures the radial ABP trace rather than the carotid trace. At the same time, the estimated central waveforms attempt to account for the site-mismatch, which is an expected source of error, even though they

are based on mathematical models. Therefore, the PP discrepancy is likely to be less than what is presented in comparison to the A-line. The data of subject S2 presented a higher standard deviation partly because the estimated diamter waveform shows large baseline fluctuation due to relatively poor image quality, which hinders reliable diameter estimation with the stable baseline.

Several factors may contribute to the underestimation of the PP. First, underestimation of the pulse wave velocity can lead to the underestimation of the PP. For example, minor wave reflection with a positive coefficient at the carotid bifurcation may contribute to the underestimation of the pulse wave velocity as it causes a flow-area loop to rotate clockwise earlier. In that case, it lowers the slope and obscures the end of a reflection-free period, making the pulse wave velocity estimation challenging. Given that atherosclerotic plaque is more developed with aging, the minor local reflection could be a possibility for the slight underestimation of PP. Figure 7-3(d) indicates the possibility of mild plaque formed close to the carotid sinus. In addition, the distension waveform, due to the viscoelasticity, may not preserve a sharp systolic peak, potentially lowering the amplitude of the estimated ABP waveform in the proposed method using ultrasound.

In addition to the physiological sources of error, remaining uncertainties in the ultrasound measurement could potentially increase error and variation in the blood pressure estimation. For example, non-circular cross-section of the vessel may produce an error in the area measurement solely based on the diameter. Figure 7-3(d) shows that, at the distal site, the cross-section presents minor eccentricity, as the common carotid artery bifurcates into the internal and external carotid arteries. If the probe insonates the distal site, the cross-sectional area may potentially be mis-calculated depending on the orientation of the ultrasound beam. The other uncertainty includes the twist angle between the probe and the target artery. The twist angle within 15°, which should be ideally 0°, can lead to the 5% change of the flow velocity. In addition, if the target vessel is placed at the edge of the lateral pressure field pattern, the flow velocity can also be over-estimated roughly by 7%. Visual inspection on the displayed ultrasound images were not very sensitive to control these sources of uncer-

tainty. These are expected to be more tightly regulated based on more sophisticated algorithms to decide the alignment of the ultrasound probe.

7.4 Summary

In this chapter, non-invasive evaluation of the carotid ABP waveform using ultrasound is compared to the radial ABP waveform obtained from the A-line measurement and the estimated central waveforms using the transfer function based approaches. Expected discrepancies in the systole are observed when directly compared to the radial trace. When compared to the estimated central waveforms using the mathematical models of GTF and ATF, the pulse pressure estimation error drops significantly. Nevertheless, the estimated PP using the proposed method underestimates over all subjects.

This study demonstrates that the estimation of the ABP waveform using the designed system is consistent with the clinically well-accepted A-line measurement. Subsequent studies can improve the accuracy of the PP estimation by removing potential sources of error in the pulse wave velocity estimation.

Chapter 8

Conclusions

8.1 Summary of Contributions

Arterial blood pressure (ABP) has been a key hemodynamics parameter in evaluating systemic circulation. ABP not only contains predictive values for adverse outcomes of cardiovascular diseases [10] but it also directly indicates the pathophysiologic states, potentially leading to heart failure and vascular diseases. Due to its convenience, a sphygmomanometer measurement at the upper arm, either using an auscultatory or an oscillometric method, has been used to measure systolic and diastolic blood pressures while an arterial-line (A-line) at the radial or femoral artery is only justified for continuous monitoring of a full waveform in intensive care settings due to its invasiveness and associated complications.

In addition, central ABP has been shown to have more clinical significance than the peripheral one [10] from the sphygmomanometer and A-line. Not only does central ABP directly exerts mechanical stress on essential organs, such as the brain, kidney, and heart, but it is also the target variable that the cardiovascular control loop actively regulates to maintain adequate perfusion to all downstream organs and tissues through smooth muscle contractions in individual branches.

Finally, recent studies concentrated on extracting clinically significant but yet to be discovered prognostic predictors or diagnostic indicators by closely investigating a pulse wave through pulse wave analysis, which has been hampered due to the

invasive nature of the A-line in a large scale population study [17, 18]. In addition, novel diagnostic opportunities may be available by understanding the variabilities in ABP waveform, similar to the study in heart rate variability, potentially enabled by continuous monitoring [23].

In this context, this thesis work aimed to develop a low-cost ultrasound scanning system that embodies a non-invasive method of measuring a central arterial pressure waveform in real-time. By using ultrasound, local arterial compliance, represented by a pulse wave velocity, and arterial pulsation are continuously monitored in real-time with a fine temporal resolution to estimate the full ABP waveform non-invasively. Along this line, the contributions of this thesis work are summarized as follows:

- The design of a programmable low-cost ultrasound scanning system is presented and validated with electrical and acoustic characterization in Chapter 3.
- Continuous monitoring of local arterial compliance, pulsation, and the ABP waveform at the common carotid artery, one of the surrogate central sites based on the similar pulse contour between the aorta and the carotid, was shown feasible by using the designed system through the proof-of-concept study in Chapter 4.
- A motion and misalignment tolerant ultrasonography strategy on measuring blood flow velocity and diameter waveform is proposed and validated in Chapters 5 and 6 to potentially extend monitoring duration significantly, thus reaching the aim of real-time and continuous monitoring.
- The proposed non-invasive evaluation of the arterial pressure waveform using ultrasound is validated in more clinically relevant settings, such as a simulated stress test under the Valsalva maneuver, presented in Chapter 6, and intensive care settings, which is briefly discussed in Chapter 7.

8.2 Future Works

Several future directions following this thesis work are suggested below:

- Refinement of the ultrasonography strategy for enhancing motion and misalignment tolerance

  The motion tolerant ultrasonography introduced in Chapter 5 achieves lateral and vertical motion tolerance. The clutter filtering imaging process improves visualization of the echoes from the arterial walls in low-contrast M-mode images. The introduced IRM estimator mitigates the effect of stationary clutter on the distension waveform estimation.

  Further imaging processing to completely separate the echoes of interest from added clutter from adjacent tissues can ensure the reliability of the distension waveform measurement, regardless of the contrast in raw ultrasound images. Due to similar spectral characteristics of the echo of interest and the clutter, the separation is not straightforward, unlike the clutter filtering in the Doppler spectrogram. Because the origins of the echoes and the clutter are different, they can potentially be separated completely in other base signal spaces.

  In addition, the intensities of the echoes from the vessel walls are found highly sensitive on the angle of insonation due to the nature of specular scattering, and they are maximized at perpendicular insonation. By using a 1-D array with a minimal channel count, perpendicular insonation on the vessel walls for the M-mode can be ensured even with a limited beam steering capability within a few degrees.

- Improvement on the system design for more wearability and user compliance

  Currently, the designed system is suited for an extended period of real-time monitoring but not for truly continuous monitoring. Several obstacles complicate such a goal, including secure placement of the probe, secure acoustic coupling for an extended period of time, and a reduced form factor and power consumption. A patch-type ultrasound probe enabled by capacitive or piezoelectric micro-machined ultrasonic transducer (cMUT or pMUT) technologies may enable more secure placement, thereby enhancing user compliance. In addition, non-drying hydrogel or other acoustic coupling materials can be used

to maintain good coupling for an extended period of time. Finally, miniaturization of the electronics system design through higher level of integration would be certainly necessary to reduce power consumption and the form factor for continuous operation of the device with a limited battery capacity.

- Further validation of biomechanics model for ABP waveform estimation

  The ABP waveform estimation model in this work only incorporates the first order effect in a linear biomechanics model. However, several second order effects are well-known, such as viscoelasticity, pressure-dependent elasticity change, and the effects of surrounding tissues. These considerations can be incorporated to further refine the estimation model.

  In addition, although frequent calibration of the baseline pressure is assumed unnecessary because a central elastic artery is believed to be negligibly modulated by smooth muscle tones, this assumption has not been completely verified. While the estimation model provides independent estimation of pulse pressure, the ABP waveform with a correct mean arterial pressure is certainly more clinically meaningful. Further works to investigate the required frequency of calibration to maintain accuracy of the estimated mean arterial pressure could certainly follow.

As suggested, numerous improvements and extensive validations are still required. With the suggested future works, the electrically power efficient and mechanically sophisticated system can be designed. In addition, refined vascular mechanics model can improve the accuracy of the ABP waveform estimation. In conclusion, this thesis work clearly demonstrates a great potential for a portable low-cost ultrasound system for the non-invasive evaluation of a central arterial pressure waveform possibly in more clinically relevant settings.

Bibliography

[1] S. Mendis, P. Puska, B. Norrving, *et al.*, *Global atlas on cardiovascular disease prevention and control.* World Health Organization, 2011.

[2] National Center for Health Statistics, *Health, United States, 2016: With Chartbook on Long-term Trends in Health.* Centers for Disease Control and Prevention, 2017.

[3] N. Westerhof, J.-W. Lankhaar, and B. E. Westerhof, "The arterial Windkessel," *Medical & Biological Engineering & Computing*, vol. 47, pp. 131–141, June 2008.

[4] R. Ross and J. A. Glomset, "The pathogenesis of atherosclerosis," *New England Journal of Medicine*, vol. 295, pp. 420–425, Aug. 1976.

[5] M. F. O'Rourke and M. E. Safar, "Relationship between aortic stiffening and microvascular disease in brain and kidney cause and logic of therapy," *Hypertension*, vol. 46, pp. 200–204, July 2005.

[6] M. E. Safar, B. I. Levy, and H. Struijker-Boudier, "Current perspectives on arterial stiffness and pulse pressure in hypertension and cardiovascular diseases," *Circulation*, vol. 107, pp. 2864–2869, June 2003.

[7] D. Y. Leung, S. Glagov, and M. B. Mathews, "Cyclic stretching stimulates synthesis of matrix components by arterial smooth muscle cells in vitro," *Science*, vol. 191, pp. 475–477, Feb. 1976.

[8] S. S. Franklin, S. A. Khan, N. D. Wong, M. G. Larson, and D. Levy, "Is pulse pressure useful in predicting risk for coronary heart disease? The framingham heart study," *Circulation*, vol. 100, pp. 354–360, July 1999.

[9] G. F. Mitchell, L. A. Moy, E. Braunwald, J.-L. Rouleau, V. Bernstein, E. M. Geltman, G. C. Flaker, and M. A. Pfeffer, "Sphygmomanometrically determined pulse pressure is a powerful independent predictor of recurrent events after myocardial infarction in patients with impaired left ventricular function," *Circulation*, vol. 96, pp. 4254–4260, Dec. 1997.

[10] M. J. Roman, R. B. Devereux, J. R. Kizer, P. M. Okin, E. T. Lee, W. Wang, J. G. Umans, D. Calhoun, and B. V. Howard, "High central pulse pressure is independently associated with adverse cardiovascular outcome: The strong heart

study," *Journal of the American College of Cardiology*, vol. 54, pp. 1730–1734, Oct. 2009.

[11] T. K. Waddell, A. M. Dart, T. L. Medley, J. D. Cameron, and B. A. Kingwell, "Carotid pressure is a better predictor of coronary artery disease severity than brachial pressure," *Hypertension*, vol. 38, pp. 927–931, Oct. 2001.

[12] M. Karamanoglu, M. F. O'Rourke, A. P. Avolio, and R. P. Kelly, "An analysis of the relationship between central aortic and peripheral upper limb pressure waves in man," *European Heart Journal*, vol. 14, pp. 160–167, Feb. 1993.

[13] G. Swamy, D. Xu, N. B. Olivier, and R. Mukkamala, "An adaptive transfer function for deriving the aortic pressure waveform from a peripheral artery pressure waveform," *American Journal of Physiology - Heart and Circulatory Physiology*, vol. 297, pp. H1956–H1963, Nov. 2009.

[14] M. Gao, W. C. Rose, B. Fetics, D. A. Kass, C.-H. Chen, and R. Mukkamala, "A simple adaptive transfer function for deriving the central blood pressure waveform from a radial blood pressure waveform," *Scientific Reports*, vol. 6, pp. 1–9, Sept. 2016.

[15] The SPRINT Research Group, "A randomized trial of intensive versus standard blood-pressure control," *New England Journal of Medicine*, vol. 373, pp. 2103–2116, Nov. 2015.

[16] G. Moody and L. Lehman, "Predicting acute hypotensive episodes: The 10th annual PhysioNet/Computers in cardiology challenge," in *2009 36th Annual Computers in Cardiology Conference (CinC)*, pp. 541–544, Sept. 2009.

[17] T. Weber, J. Auer, M. F. O'Rourke, E. Kvas, E. Lassnig, R. Berent, and B. Eber, "Arterial stiffness, wave reflections, and the risk of coronary artery disease," *Circulation*, vol. 109, pp. 184–189, Jan. 2004.

[18] D. Chemla, A. Nitenberg, J.-L. Teboul, C. Richard, X. Monnet, H. Le Clesiau, P. Valensi, and M. Brahimi, "Subendocardial viability ratio estimated by arterial tonometry: A critical evaluation in elderly hypertensive patients with increased aortic stiffness," *Clinical and Experimental Pharmacology and Physiology*, vol. 35, pp. 909–915, Aug. 2008.

[19] S. J. Marchais, A. P. Guerin, B. M. Pannier, B. I. Levy, M. E. Safar, and G. M. London, "Wave reflections and cardiac hypertrophy in chronic uremia. Influence of body size.," *Hypertension*, vol. 22, pp. 876–883, Dec. 1993.

[20] D. Tsiachris, C. Tsioufis, D. Syrseloudis, D. Roussos, I. Tatsis, K. Dimitriadis, K. Toutouzas, E. Tsiamis, and C. Stefanadis, "Subendocardial viability ratio as an index of impaired coronary flow reserve in hypertensives without significant coronary artery stenoses," *Journal of Human Hypertension*, vol. 26, pp. 64–70, Jan. 2012.

[21] R. Mukkamala, A. Reisner, H. Hojman, R. Mark, and R. Cohen, "Continuous cardiac output monitoring by peripheral blood pressure waveform analysis," *IEEE Transactions on Biomedical Engineering*, vol. 53, pp. 459–467, Mar. 2006.

[22] B. Haslam, T. Heldt, A. J. Gordhandas, C. Ricciardi, and G. Verghese, "Relating noninvasive cardiac output and total peripheral resistance estimates to physical activity in an ambulatory setting.," in *AAAI Spring Symposium: Computational Physiology*, pp. 1–9, 2011.

[23] M. L. Appel, R. D. Berger, J. P. Saul, J. M. Smith, and R. J. Cohen, "Beat to beat variability in cardiovascular variables: Noise or music?," *Journal of the American College of Cardiology*, vol. 14, pp. 1139–1148, Nov. 1989.

[24] S. Akselrod, D. Gordon, F. A. Ubel, D. C. Shannon, A. C. Berger, and R. J. Cohen, "Power spectrum analysis of heart rate fluctuation: a quantitative probe of beat-to-beat cardiovascular control," *Science*, vol. 213, pp. 220–222, July 1981.

[25] R. W. deBoer, J. M. Karemaker, and J. Strackee, "Hemodynamic fluctuations and baroreflex sensitivity in humans: a beat-to-beat model," *The American Journal of Physiology*, vol. 253, pp. H680–H689, Sept. 1987.

[26] L. S. Costanzo, *Physiology*. Philadelphia, PA : Saunders/Elsevier, fifth ed., 2014.

[27] N. Nasr, A. P.-L. Traon, and V. Larrue, "Baroreflex sensitivity is impaired in bilateral carotid atherosclerosis," *Stroke*, vol. 36, pp. 1891–1895, Sept. 2005.

[28] G. Parati, G. Pomidossi, F. Albini, D. Malaspina, and G. Mancia, "Relationship of 24-hour blood pressure mean and variability to severity of target-organ damage in hypertension," *Journal of Hypertension*, vol. 5, pp. 93–98, Feb. 1987.

[29] J. Penaz *et al.*, "Photoelectric measurement of blood pressure, volume and flow in the finger," in *Digest of the 10th international conference on medical and biological engineering*, vol. 104, 1973.

[30] B. P. M. Imholz, G. a. V. Montfrans, J. J. Settels, G. M. a. V. D. Hoeven, J. M. Karemaker, and W. Wieling, "Continuous non-invasive blood pressure monitoring: reliability of Finapres device during the Valsalva manoeuvre," *Cardiovascular Research*, vol. 22, pp. 390–397, June 1988.

[31] G. M. Drzewiecki, J. Melbin, and A. Noordergraaf, "Arterial tonometry: Review and analysis," *Journal of Biomechanics*, vol. 16, no. 2, pp. 141–152, 1983.

[32] M. F. O'Rourke and A. Adji, "Clinical use of applanation tonometry: Hope remains in Pandoras box:," *Journal of Hypertension*, vol. 28, pp. 229–233, Feb. 2010.

[33] L. M. Van Bortel, E. J. Balkestein, J. J. van der Heijden-Spek, F. H. Vanmolkot, J. A. Staessen, J. A. Kragten, J. W. Vredeveld, M. E. Safar, H. A. S. Boudier,

and A. P. Hoeks, "Non-invasive assessment of local arterial pulse pressure: comparison of applanation tonometry and echo-tracking," *Journal of Hypertension*, vol. 19, no. 6, pp. 1037–1044, 2001.

[34] J. M. Meinders and A. P. G. Hoeks, "Simultaneous assessment of diameter and pressure waveforms in the carotid artery," *Ultrasound in Medicine & Biology*, vol. 30, pp. 147–154, Feb. 2004.

[35] A. M. Zakrzewski, *Arterial blood pressure estimation using ultrasound*. Thesis, Massachusetts Institute of Technology, 2017.

[36] A. M. Zakrzewski and B. W. Anthony, "Arterial blood pressure estimation using ultrasound: Clinical results on healthy volunteers and a medicated hypertensive volunteer," in *2017 39th Annual International Conference of the IEEE Engineering in Medicine and Biology Society (EMBC)*, pp. 2154–2157, July 2017.

[37] B. W. A. M. M. Beulen, N. Bijnens, G. G. Koutsouridis, P. J. Brands, M. C. M. Rutten, and F. N. van de Vosse, "Toward noninvasive blood pressure assessment in arteries by using ultrasound," *Ultrasound in Medicine & Biology*, vol. 37, pp. 788–797, May 2011.

[38] J. Vappou, J. Luo, K. Okajima, M. D. Tullio, and E. E. Konofagou, "Non-invasive measurement of local pulse pressure by pulse wave-based ultrasound manometry (PWUM)," *Physiological Measurement*, vol. 32, pp. 1653–1662, Oct. 2011.

[39] J. Seo, S. Pietrangelo, H.-S. Lee, and C. Sodini, "Noninvasive arterial blood pressure waveform monitoring using two-element ultrasound system," *IEEE Transactions on Ultrasonics, Ferroelectrics, and Frequency Control*, vol. 62, pp. 776–784, Apr. 2015.

[40] J. Seo, S. J. Pietrangelo, H. S. Lee, and C. G. Sodini, "Carotid arterial blood pressure waveform monitoring using a portable ultrasound system," in *2015 37th Annual International Conference of the IEEE Engineering in Medicine and Biology Society (EMBC)*, pp. 5692–5695, Aug. 2015.

[41] T. L. Szabo, *Diagnostic ultrasound imaging : inside out*. Academic Press series in biomedical engineering, Burlington, MA : Elsevier Academic Press, first ed., 2004.

[42] J. A. Jensen, *Estimation of blood velocities using ultrasound: a signal processing approach*. Cambridge ; New York, USA : Cambridge University Press, first ed., 1996.

[43] W. N. McDicken, *Diagnostic ultrasonics: principles and use of instruments*. Wiley medical publication, New York : Wiley, second ed., 1981.

[44] F. W. Kremkau, *Diagnostic ultrasound: principles and instruments*. Philadelphia, PA: W.B. Saunders, fifth ed., 1998.

[45] US Food and Drug Administration, *Information for Manufacturers Seeking Marketing Clearance of Diagnostic Ultrasound Systems and Transducers.* U.S. Department of Health and Human Services, Food and Drug Administration, 2008.

[46] J. Seo, *Continuous and non-invasive blood pressure monitoring using ultrasonic methods.* Thesis, Massachusetts Institute of Technology, 2014.

[47] J. A. Jensen, "FIELD: A program for simulating ultrasound systems," in *10th Nordic-Baltic Conference on Biomedical Imaging*, vol. 4, supplement 1, part 1, pp. 351–353, 1996.

[48] J. Jensen and N. Svendsen, "Calculation of pressure fields from arbitrarily shaped, apodized, and excited ultrasound transducers," *IEEE Transactions on Ultrasonics, Ferroelectrics and Frequency Control*, vol. 39, pp. 262–267, Mar. 1992.

[49] D. A. McDonald, *Blood flow in arteries.* Baltimore : Williams & Wilkins, second ed., 1974.

[50] W. R. Milnor, *Hemodynamics.* Baltimore : Williams & Wilkins, 1989.

[51] J. R. Womersley, "Method for the calculation of velocity, rate of flow and viscous drag in arteries when the pressure gradient is known," *The Journal of Physiology*, vol. 127, pp. 553–563, Mar. 1955.

[52] J. Womersley, "XXIV. Oscillatory motion of a viscous liquid in a thin-walled elastic tubeI: The linear approximation for long waves," *Philosophical Magazine Series 7*, vol. 46, no. 373, pp. 199–221, 1955.

[53] J. C. Bramwell and A. V. Hill, "The velocity of the pulse wave in man," *Proceedings of the Royal Society of London. Series B, Containing Papers of a Biological Character*, vol. 93, pp. 298–306, Apr. 1922.

[54] J. K.-J. Li, *Arterial system dynamics.* New York University biomedical engineering series, New York : New York University Press, first ed., 1987.

[55] C. D. Clemente, *Anatomy : a regional atlas of the human body.* Baltimore : Williams & Wilkins, fourth ed., 1997.

[56] N. Stergiopulos, D. F. Young, and T. R. Rogge, "Computer simulation of arterial flow with applications to arterial and aortic stenoses," *Journal of Biomechanics*, vol. 25, pp. 1477–1488, Dec. 1992.

[57] R. Kelly and D. Fitchett, "Noninvasive determination of aortic input impedance and external left ventricular power output: A validation and repeatability study of a new technique," *Journal of the American College of Cardiology*, vol. 20, pp. 952–963, Oct. 1992.

[58] R. Mukkamala, J.-O. Hahn, O. Inan, L. Mestha, C.-S. Kim, H. Toreyin, and S. Kyal, "Toward ubiquitous blood pressure monitoring via pulse transit time: Theory and practice," *IEEE Transactions on Biomedical Engineering*, vol. 62, pp. 1879–1901, Aug. 2015.

[59] E. Hermeling, A. P. G. Hoeks, M. H. M. Winkens, J. L. Waltenberger, R. S. Reneman, A. A. Kroon, and K. D. Reesink, "Noninvasive assessment of arterial stiffness should discriminate between systolic and diastolic pressure ranges," *Hypertension*, vol. 55, pp. 124–130, Jan. 2010.

[60] J. Luo, R. Li, and E. Konofagou, "Pulse wave imaging of the human carotid artery: an in vivo feasibility study," *IEEE Transactions on Ultrasonics, Ferroelectrics and Frequency Control*, vol. 59, pp. 174–181, Jan. 2012.

[61] P. J. Brands, J. M. Willigers, L. A. F. Ledoux, R. S. Reneman, and A. P. G. Hoeks, "A noninvasive method to estimate pulse wave velocity in arteries locally by means of ultrasound," *Ultrasound in Medicine & Biology*, vol. 24, pp. 1325–1335, Dec. 1998.

[62] S. I. Rabben, N. Stergiopulos, L. R. Hellevik, O. A. Smiseth, S. Slrdahl, S. Urheim, and B. Angelsen, "An ultrasound-based method for determining pulse wave velocity in superficial arteries," *Journal of Biomechanics*, vol. 37, pp. 1615–1622, Oct. 2004.

[63] C. A. C. Bastos, P. J. Fish, and F. Vaz, "Spectrum of Doppler ultrasound signals from nonstationary blood flow," *IEEE Transactions on Ultrasonics, Ferroelectrics, and Frequency Control*, vol. 46, pp. 1201–1217, Sept. 1999.

[64] R. W. Gill, "Measurement of blood flow by ultrasound: Accuracy and sources of error," *Ultrasound in Medicine & Biology*, vol. 11, pp. 625–641, July 1985.

[65] A. Hoeks, Xu Di, P. Brands, and R. Reneman, "An effective algorithm for measuring diastolic artery diameters," *Archives of Acoustics*, vol. 20, pp. 65–76, Jan. 1995.

[66] R. W. Stadler, J. Andrew Taylor, and R. S. Lees, "Comparison of B-mode, M-mode and echo-tracking methods for measurement of the arterial distension waveform," *Ultrasound in Medicine & Biology*, vol. 23, no. 6, pp. 879–887, 1997.

[67] A. P. G. Hoeks, T. G. J. Arts, P. J. Brands, and R. S. Reneman, "Comparison of the performance of the RF cross correlation and doppler autocorrelation technique to estimate the mean velocity of simulated ultrasound signals," *Ultrasound in Medicine & Biology*, vol. 19, no. 9, pp. 727–740, 1993.

[68] P. J. Brands, A. P. G. Hoeks, L. A. F. Ledoux, and R. S. Reneman, "A radio frequency domain complex cross-correlation model to estimate blood flow velocity and tissue motion by means of ultrasound," *Ultrasound in Medicine & Biology*, vol. 23, no. 6, pp. 911–920, 1997.

[69] P. G. M. de Jong, T. Arts, A. P. G. Hoeks, and R. S. Reneman, "Determination of tissue motion velocity by correlation interpolation of pulsed ultrasonic echo signals," *Ultrasonic Imaging*, vol. 12, pp. 84–98, Apr. 1990.

[70] J. Seo, C. G. Sodini, and H. S. Lee, "Monitoring of pulse pressure and arterial pressure waveform changes during the valsalva maneuver by a portable ultrasound system," in *2018 40th Annual International Conference of the IEEE Engineering in Medicine and Biology Society (EMBC) (accepted for publication)*, July 2018.

[71] D. W. Rickey, P. A. Picot, D. A. Christopher, and A. Fenster, "A wall-less vessel phantom for Doppler ultrasound studies," *Ultrasound in Medicine & Biology*, vol. 21, no. 9, pp. 1163–1176, 1995.

[72] K. Zell, J. I. Sperl, M. W. Vogel, R. Niessner, and C. Haisch, "Acoustical properties of selected tissue phantom materials for ultrasound imaging," *Physics in Medicine & Biology*, vol. 52, no. 20, pp. N475–N484, 2007.

[73] S. J. Pietrangelo, *A wearable Transcranial Doppler ultrasound phased array system*. Thesis, Massachusetts Institute of Technology, 2017.

[74] J. Krejza, M. Arkuszewski, S. E. Kasner, J. Weigele, A. Ustymowicz, R. W. Hurst, B. L. Cucchiara, and S. R. Messe, "Carotid artery diameter in men and women and the relation to body and neck size," *Stroke*, vol. 37, pp. 1103–1105, Apr. 2006.

[75] F. Hansen, P. Mangell, B. Sonesson, and T. Lnne, "Diameter and compliance in the human common carotid artery variations with age and sex," *Ultrasound in Medicine & Biology*, vol. 21, pp. 1–9, Jan. 1995.

[76] A. L. Pauca, S. L. Wallenhaupt, N. D. Kon, and W. Y. Tucker, "Does radial artery pressure accurately reflect aortic pressure?," *Chest*, vol. 102, pp. 1193–1198, Oct. 1992.

[77] B. Dunmire, K. W. Beach, K.-H. Labs, M. Plett, and D. E. Strandness Jr., "Cross-beam vector Doppler ultrasound for angle-independent velocity measurements," *Ultrasound in Medicine & Biology*, vol. 26, pp. 1213–1235, Oct. 2000.

[78] P. Tortoli, G. Bambi, and S. Ricci, "Accurate Doppler angle estimation for vector flow measurements," *IEEE Transactions on Ultrasonics, Ferroelectrics, and Frequency Control*, vol. 53, pp. 1425–1431, Aug. 2006.

[79] D. W. Holdsworth, C. J. D. Norley, R. Frayne, D. A. Steinman, and B. K. Rutt, "Characterization of common carotid artery blood-flow waveforms in normal human subjects," *Physiological Measurement*, vol. 20, pp. 219–240, Aug. 1999.

[80] W. Zong, T. Heldt, G. Moody, and R. Mark, "An open-source algorithm to detect onset of arterial blood pressure pulses," in *Computers in Cardiology, 2003*, pp. 259–262, Sept. 2003.

[81] J. Seo, S. J. Pietrangelo, C. G. Sodini, and H. S. Lee, "Motion tolerant unfocused imaging of physiological waveforms for blood pressure waveform estimation using ultrasound," *IEEE Transactions on Ultrasonics, Ferroelectrics, and Frequency Control*, vol. 65, pp. 766–779, May 2018.

[82] M. Tanter and M. Fink, "Ultrafast imaging in biomedical ultrasound," *IEEE Transactions on Ultrasonics, Ferroelectrics, and Frequency Control*, vol. 61, pp. 102–119, Jan. 2014.

[83] C. M. Gallippi and G. E. Trahey, "Adaptive clutter filtering via blind source separation for two-dimensional ultrasonic blood velocity measurement," *Ultrasonic Imaging*, vol. 24, pp. 193–214, Oct. 2002.

[84] K. V. Ramnarine, D. K. Nassiri, P. R. Hoskins, and J. Lubbers, "Validation of a new blood-mimicking fluid for use in doppler flow test objects," *Ultrasound in Medicine & Biology*, vol. 24, pp. 451–459, Mar. 1998.

[85] L. Pstras, K. Thomaseth, J. Waniewski, I. Balzani, and F. Bellavere, "The Valsalva manoeuvre: physiology and clinical examples," *Acta Physiologica*, vol. 217, pp. 103–119, June 2016.

[86] J. P. Murgo, N. Westerhof, J. P. Giolma, and S. A. Altobelli, "Manipulation of ascending aortic pressure and flow wave reflections with the Valsalva maneuver: relationship to input impedance," *Circulation*, vol. 63, pp. 122–132, Jan. 1981.

[87] R. D. Latham, N. Westerhof, P. Sipkema, B. J. Rubal, P. Reuderink, and J. P. Murgo, "Regional wave travel and reflections along the human aorta: a study with six simultaneous micromanometric pressures," *Circulation*, vol. 72, pp. 1257–1269, Dec. 1985.

[88] J.-L. Hbert, C. Coirault, K. Zamani, G. Fontaine, Y. Lecarpentier, and D. Chemla, "Pulse pressure response to the strain of the Valsalva maneuver in humans with preserved systolic function," *Journal of Applied Physiology*, vol. 85, pp. 817–823, Sept. 1998.

[89] C.-H. Chen, E. Nevo, B. Fetics, P. H. Pak, F. C. P. Yin, W. L. Maughan, and D. A. Kass, "Estimation of central aortic pressure waveform by mathematical transformation of radial tonometry pressure: Validation of generalized transfer function," *Circulation*, vol. 95, pp. 1827–1836, Apr. 1997.

[90] S. A. Hope, D. B. Tay, I. T. Meredith, and J. D. Cameron, "Use of arterial transfer functions for the derivation of aortic waveform characteristics," *Journal of Hypertension*, vol. 21, pp. 1299–1305, July 2003.

[91] M. O'Rourke and V. Clinic, "Use of generalised transfer function in clinical studies," 2005.